DEVELOPMENT OF MINIATURIZED ELECTROCHEMICAL DEVICES FOR DETECTION OF DOPAMINE, L-CYSTEINE AND ANTI-SARS-COV-2 ANTIBODIES

WISARUT KHAMCHAROEN

Graduate School Srinakharinwirot University

2021

การพัฒนาอุปกรณ์ย่อส่วนทางเคมีไฟฟ้าสำหรับการตรวจวัดโดพามีน แอล-ซิสเทอีน และแอนติบอดีต้านเชื้อไวรัสซาร์ส-โควี-ทู

วิศรุต ขำเจริญ

ปริญญานิพนธ์นี้เป็นส่วนหนึ่งของการศึกษาตามหลักสูตร
ปรัชญาดุษฎีบัณฑิต สาขาวิชาเคมีประยุกต์
คณะวิทยาศาสตร์ มหาวิทยาลัยศรีนครินทรวิโรฒ
ปีการศึกษา 2564

DEVELOPMENT OF MINIATURIZED ELECTROCHEMICAL DEVICES FOR DETECTION OF DOPAMINE, L-CYSTEINE AND ANTI-SARS-COV-2 ANTIBODIES

WISARUT KHAMCHAROEN

A Dissertation Submitted in Partial Fulfillment of the Requirements

for the Degree of DOCTOR OF PHILOSOPHY

(Applied Chemistry)

Faculty of Science, Srinakharinwirot University

2021

THE DISSERTATION TITLED

DEVELOPMENT OF MINIATURIZED ELECTROCHEMICAL DEVICES FOR DETECTION OF DOPAMINE, L-CYSTEINE AND ANTI-SARS-COV-2 ANTIBODIES

BY

WISARUT KHAMCHAROEN

HAS BEEN APPROVED BY THE GRADUATE SCHOOL IN PARTIAL FULFILLMENT OF THE REQUIREMENTS FOR THE DOCTOR OF PHILOSOPHY IN APPLIED CHEMISTRY AT SRINAKHARINWIROT UNIVERSITY

(Assoc. Prof. Dr. Chatchai Ekpanyaskul, MD.)

Dean of Graduate School

ORAL DEFENSE COMMITTEE

..... Major-advisor

(Assoc. Prof. Dr.Weena Siangproh)

..... Chair

(Prof. Dr.Orawon Chailapakul)

..... Committee

(Assoc. Prof. Dr.Apinya Chaivisuthangkura)

Title	DEVELOPMENT OF MINIATURIZED ELECTROCHEMICAL DEVICES FOR DETECTION OF DOPAMINE, L-CYSTEINE AND ANTI-SARS-COV-2 ANTIBODIES
Author	WISARUT KHAMCHAROEN
Degree	DOCTOR OF PHILOSOPHY
Academic Year	2021
Thesis Advisor	Associate Professor Dr. Weena Siangproh

This dissertation aims to develop novel electrochemical devices for the detection of important target analytes, which can be divided into two parts. The first part concerned the development of electrochemical paper-based analytical devices for clinical and food applications, and there were two subprojects in this section. The first subproject is the fabrication of electrochemical microfluidic paper-based analytical device (eμPAD) and developed for the highly selective and sensitive detection of dopamine (DA). Nafion was deposited into paper-based microchannel to increase selectivity and multilayered eμPAD was subsequently designed for the flow of the solution. The next subproject is a novelty of poly(cysteine) modified screen-printed graphene electrode, developed for the electroanalysis of L-cysteine (Cys). Furthermore, an all-in-one origami paper-based analytical device was proposed to combine all of the procedures into one device and providing a more convenient method for end-users. The second part was the development of an electrochemical device for COVID-19 diagnosis. In this part, the sequential delivery pump-free microfluidic coupled with screen-printed electrodes (SPE), which were developed for simple and rapid detection of IgG antibodies against SARS-CoV-2 nucleocapsid protein (anti-N antibody). The immunological assay was performed on the nitrocellulose membrane where the SPE was aligned above to perform the sensitive electrochemical detection of anti-N antibodies. As previously mentioned, all electrochemical devices produced from this work had a great analytical performance and a low limit of detection that can be applied to detect specific target analytes in various real samples, e.g., urine, whole blood, and food samples.

Keyword : Electrochemical detection, Dopamine, L-cysteine, COVID-19

ACKNOWLEDGEMENTS

First and foremost, I would like to express my deepest gratitude to my advisor, Associate Professor Dr. Weena Siangproh, for her guidance, motivation and encouragement through my incredible Ph.D. life adventure. She not only provided critical advice in experiments and writing, but also taught me to overcome the difficulties and fears. Thanks for always telling me that I am awesome even the time I did not feel that way. Any future of my career as a scientist will be tied to experiences, I received under her supervision.

I would like to thank Professor Dr. Charles S. Henry from Colorado State University for mentoring and giving opportunity to work on exciting project throughout 1 year in USA. I am grateful to all of those with whom I have had to work during coronavirus project. I wish to thank members in Henry group for their help and inviting me to join many outdoor activities, it was amazing year in USA.

I am fortunate to have been a part of Electroanalytical and Imaging Sensor Research Group (EISRG). I wish to thank all member for their help and encouragement. The moments of hard works and happiness in laboratory will be forever remembered. I would also like to thank members of Electrochemistry and Optical Spectroscopy Center of Excellence (EOSCE) for chemical and equipment resources, and valuable suggestions.

I grateful acknowledge the financial supports during my Ph.D. and short-term research program in USA from Science Achievement Scholarship of Thailand (SAST). I am thankful to my Ph.D. dissertation committees Professor Dr. Orawon Chailapakul and Associate Professor Dr. Apinya Chaivisuthangkura for their contributions and feedbacks.

Special words of appreciation are dedicated to my friends for providing happy distractions to rest my mind outside of research. Lastly, my family deserves endless gratitude, my mother, Piyanuch Khamcharoen, my grandmother, Mayuree Khamcharoen and other family members for economical support and unconditional love. My accomplishments and success are because they believed in me.

WISARUT KHAMCHAROEN

TABLE OF CONTENTS

Page

List of tables

Page

List of figures

Page

CHAPTER 1
INTRODUCTION

1.1 Background

The tremendous growth of technology makes a great revolution in analytical chemistry. Various analytical approaches, such as high-performance liquid chromatography (HPLC), gas chromatography (GC), mass spectrometry (MS), UV-visible spectrophotometry, fluorescence spectrophotometry, electrophoresis, and surface enhanced Raman scattering have been developed for a wide range of applications, including clinical diagnosis, drug analysis, environmental monitoring, and food control and safety. Even though these techniques provided great performance in terms of high sensitivity and selectivity, some limitations still remained, such as the need for multiple sample preparation steps, large amounts of sample volume, specialized analyzing skills and expensive instruments. Nowadays, the new trends of analytical methods are based on the ideal of low-cost, miniaturized system, hand-held equipment, and user-friendly. These requirements allow us to develop new alternative sensing devices that can alleviate issues from previous methods.

A small biological compound released by the metabolite function in the human body system, such as dopamine (DA) can be beneficial as a trust parameter in the diagnosis of many diseases. The abnormal DA concentration in biological fluid relates to a variety of neurological disorders, immune suppression, and drug addiction issues (de Fatima Ulbrich, Winiarski, Jost, & Maduro de Campos, 2020). However, DA in biological samples present at very low level and mixed in several complex interferences that make it difficult to measure the exact concentration and long-time consuming to operate the method. Hence, the requirement of a fast and low-cost analytical tool for real-time monitoring of DA is important for early diagnosis.

The demand of analytical methods for food analysis has exponential growth for several years. Especially, the determination of additive compounds in food supplies remains a top priority for the food industry scale, in order to ensure the quality of food

products before launching it to the market. Likewise in the Islamic world, the certification for permissible food and avoidance from prohibited food in accordance with Islamic law (Shariah) known as Halal, is the most significant concern (Karahalil, 2020). Especially in this decade, Halal food consumption has become new trend in non-Muslim countries to export Halal products all over the world. As a result, the awareness of non-approval ingredients in Halal food supplies need to be in the spotlight. In the bakery industry, L-cysteine (Cys) or E920 is used as a food additive. Because the advantages are to reduce the mixing time in dough preparation and to enhance soft texture in bakeries. However, some parts of the global Cys production are extracted from human hair and forbidden animals, both of which are prohibited to eat under Islamic law. Thus, the use of Cys as a food additive is disallowed in many Muslim countries. The development of a new alternative analytical platform for detecting Cys in food products is extremely required.

The infectious diseases caused by viruses are the most urgent global crisis in 2020, since the World Health Organization (WHO) announced in mid-March that a pandemic of severe acute respiratory syndrome coronavirus 2 (SARS-CoV-2) is ongoing (Lee et al., 2021; Tuaillon et al., 2020). Coronavirus are easily transmitted via respiratory droplets and have an incubation period within 2-14 days. Therefore, in a matter of months, the outbreaks of this virus spread from its origins in Wuhan, China, to most of countries around the world. Even a year after the outbreak began, the numbers of infected patients remained significantly high. Early diagnosis to isolate infected patients from coronavirus is a vital solution to reducing numbers of patients. The quantitative reverse transcription polymerase chain reaction (RT–qPCR) is the gold-standard method for determining viral RNAs of the SARS-CoV-2 virus in patient mucus samples (Vogels et al., 2020). However, the difficulty and cost of this technique are still significant issues. In the global community, a rapid and low-cost SARS-CoV-2 detection tool is in high demand for large-scale testing (Li et al., 2020).

Electrochemical techniques have received attention for analytical applications, due to advantages such as portable equipment, rapid analysis time from sample-to-

answer, small sample volume, and high accuracy and precision. The ability to miniaturize electrochemical instruments brought the analytical chemists to generate novel designs and applications. To fabricate electrochemical devices, low-cost materials based on the substrate, such as paper and flexible plastic thin film have gained massive consideration for the modern electroanalytical method. These alternative materials have several outstanding characteristics, such as simple assembly, wide availability, reduction to microanalytical systems and easy disposal (Noviana, Carrão, Pratiwi, & Henry, 2020).

Microfluidic paper-based analytical device (μPAD) concept was first introduced by Whitesides's group in 2007 (Andres W. Martinez, Phillips, Butte, & Whitesides, 2007), they constructed a microchannel on paper substrate using hydrophilic/hydrophobic materials, which generated self-pumping property via capillary force of μPAD without the use of an external pump. The enjoyable developments of μPAD after their work have provided greater analytical performance such as reducing operational steps, separation of analytes, preconcentration and combining multiple detections. Following that, the new format of paper-based platform has been proposed for analytical application. An origami paper-based analytical device (oPAD) has demonstrated high potentials to facilitate simpler analytical methods for end-users. The oPAD is created by folding paper and stacking different paper layers in vertical style, while the set-up layers enable several functions (C. A. Chen, Yeh, Tsai, Li, & Chen, 2019). Furthermore, the attempt to use low-cost and flexible material substrates is not conducted only in paper-based analytical device, a capillary-driven microfluidic device was proposed using lamination-based methods which stack from multiple layers of polyester film and Double-sided adhesive film (DSA) for simple fabrication and a powerful flow-based system. This microfluidic platform outperforms the μPAD in terms of functional efficiency, including fast flow rate, uniform flow, and low risk of sample loss (Jang, Carraõ, Menger, Moraes De Oliveira, & Henry, 2020; Jang et al., 2021). Because of the capabilities of alternative platforms mentioned above, many works have been developed by taking the

advantages of μPAD, oPAD, and lamination-based capillary-driven microfluidic device for various analytical applications.

From the motivation as mentioned above, In the first part of this dissertation, simple, sensitive, selective, and low-cost paper-based electrochemical devices for point-of-care (POC) testing and food analysis were proposed. For POC testing, an electrochemical microfluidic paper-based analytical device (eμPAD) was developed. To provide high selectivity, Nafion deposited on microfluidic paper-based channel is used to block ascorbic (AA) before solution is flowed to the electrode area, whereas AA is a major interference in biological sample. Poly(glutamic acid) (PGA) film was employed as modifier to alter the screen-printed graphene electrode (SPGE) surface to enhance the electrochemical response of DA. In addition, a multilayered eμPAD was constructed to improve the electrochemical performance of DA. For food analysis, a new sensing device using self-modification of poly(cysteine) (poly(Cys)) modified screen-printed graphene electrode (SPGE) for detection of Cys in food samples was developed. This sensor used Cys itself as a monomer to electropolymerize at electrode surface. The new all-in-one oPAD was proposed to improve precision from device-to-device, to avoid Cys contamination from modification to detection steps and offers more convenient method for the end-users. This platform was successfully applied to detect Cys in food products that had several complex interferences.

With the severe pandemic situation of the COVID-19, all sectors are working together to develop a method to measure the related targets concerning this disease. Simple, portable, and rapid detection is highly required for large scale population screening to tackle the cluster of infection. As well as to overcome the lack of accuracy that revealed from test kits in the market. Therefore, in the second part of dissertation, electrochemical capillary-driven immunoassay for detecting IgG antibodies against SARS-CoV-2 nucleocapsid protein (anti-N antibody) was developed for COVID-19 diagnosis. The lamination-based capillary-driven microfluidic device was designed for lateral flow immunoassay (LFIA), which combines with highly sensitive electrochemical technique using screen-printed carbon electrode (SPCE) for direct detection of anti-N

antibody in human blood sample. The device included automating sequential delivery system for transporting reagents to detection area, which reduced multi-pipetting steps and analysis time.

1.2 Objectives of the research

The aim of research consists of three goals as listed below:

1. To develop a novel electrochemical microfluidic paper-based analytical device for monitoring of dopamine levels in biological samples.

2. To propose a new electrochemical Cys sensor coupled with all-in-one oPAD for food quality control and Halal food investigation applications

3. To develop a lamination-based sequential capillary-driven microfluidic device combined with screen-printed electrode for the electrochemical detection of anti-N antibody in human blood samples.

1.3 Significance of the research

1. This research can be used to detect important analytes for a variety of applications, such as clinical diagnosis and food analysis.

2. The proposed platforms open the vision to the possibility of using them as models for alternative electroanalytical devices in other applications.

3. The materials selected for this research have the potential to reduce the cost of analytical sensing devices.

1.4 Scope of the research

This research focuses on the fabrication methods for developing electrochemical devices, including μPAD, oPAD, and lamination-based capillary-driven microfluidic device to obtain high potential platforms for detection of DA, Cys and anti-N antibody, respectively. The designed concepts not only offer low-cost materials, simple fabrication and operation, and rapid detection, but they also maintain high sensitivity and selectivity. Analytical performances such as linear concentration range, limit of detection (LOD) , precision, accuracy and selectivity were studied. These novel analytical platforms were eventually applied to detect analytes in real samples.

CHAPTER 2
THEORY AND LITERATURE REVIEWS

2.1 Electrochemical technique

Electroanalytical chemistry is a branch of analytical chemistry that studies the interrelations between electricity and chemical reactions in order to measure the electrical properties such as current, potential and charge. The electrical quantity produced by the chemical reaction can be used for quantitative analysis. As a result, this technique has a wide range of applications (Bard & Faulkner, 2001). Electroanalytical chemistry generally divided into two main types including potentiometric and voltammetric measurements. In this research, several types of voltammetry are used as an electrochemical technique for analytical applications.

2.1.1 Voltammetry

Voltammetry is an electroanalytical technique that measures current as a function of potential or voltage applied to a working electrode. The result of this technique is known as a voltammogram. This technique can be used to investigate the properties of electroactive species that can be reduced or oxidized at the working electrode. When negative potentials are applied to the electrode, it becomes more strongly oxidizing agent, and reduction reaction occurs. On the other hand, when potentials at the electrode are applied to positive potentials, it becomes more strongly reducing agent, and oxidation reaction occurs. Voltammetry is divided into various types based on the potential waveform that is applied to the working electrode, such as linear sweep voltammetry (LSW), cyclic voltammetry (CV), normal pulse voltammetry (NPV), differential pulse voltammetry (DPV) , square wave voltammetry (SWV) , Chronoamperometry, anodic stripping voltammetry, cathodic stripping voltammetry, and adsorptive stripping voltammetry. In this research, CV, DPV, and chronoamperometry were used for electrochemical detection and characterization.

2.1.1.1 Cyclic voltammetry (CV)

CV is a common and widely used technique for characterizing the electrochemical properties of analytes during the initial study of the redox reaction.

Furthermore, CV is used to gain insight into the kinetics of electrode reactions, which are related to the electron transfer process and chemical reaction (Heinze, 1984). In an experiment, working electrode is placed in a stagnant solution and the potential versus time is plotted as a triangular potential waveform, as shown in Figure 1. During operation, the potentiostat measures the current generated by the reaction at the working electrode surface, which corresponds to the analyte concentration. The resulting plot of current versus applied potential is known as a cyclic voltammogram.

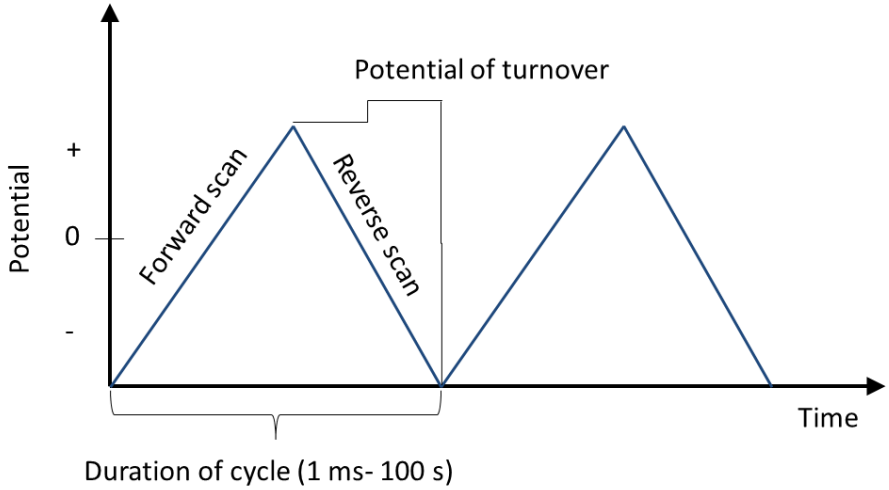

Figure 1 Illustration of CV waveform

Source: Fiala, R. (2017) "Cycling Voltammetry: principle." Retrieved 28 January 2019). from https://physics.mff.cuni.cz/kfpp/povrchy/method/cv-principles.

The expected cyclic voltammogram of reversible redox reaction in a single potential cycle is shown in Figure 2. At the beginning, it is assumed that there is only oxidized form (O). As a result, for the first half-cycle, the potential is scanned to more negative potential, starting from a value where no reduction occurs. When the applied potential approaches the formal potential (E^0) of the redox reaction, a cathodic current begins to increase, eventually resulting in the appearance of a peak. During the potential is scanned to negative potential in which the reduction process takes place, reduced (R) molecules are produced and accumulated near the electrode surface. The direction of potential sweep is reversed to positive potential after the applied potential

traverses more than 90/ *n* mV beyond the observed peak. The R molecules are re-oxidized back to O, and an anodic peak appears (J. Wang, 2000).

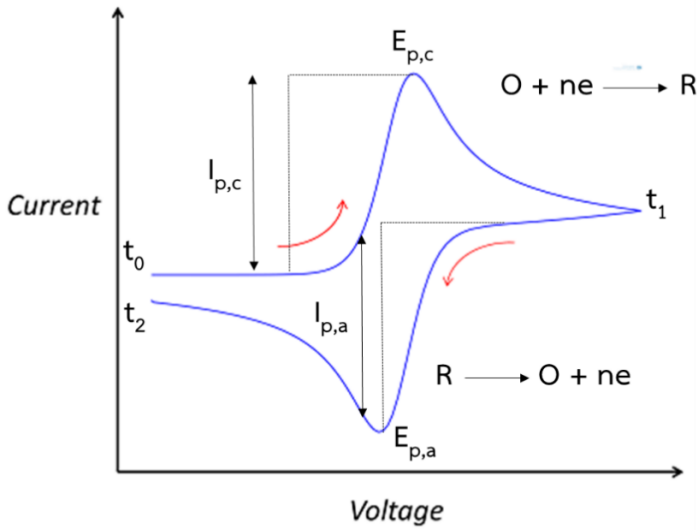

Figure 2 Typical cyclic voltammogram for reversible reaction.

Source: Dickinson, E. (2013) "Modeling Electroanalysis: Cyclic Voltammetry." Retrieved 14 January 2019, from https://www.comsol.com/blogs/modeling-electroanalysis-cyclic-voltammetry/

According to reversible reaction, it can be characterized by Randles-Sevcik equation:

$$I_p = (2.69 \times 10^5) n^{3/2} A C D^{1/2} \nu^{1/2} \quad \text{.....equation 1}$$

Where:

I_p = peak current (A)

n = number of electrons

A = electrode area (cm^2)

C = concentration of analyte (mol/cm^3)

D = the diffusion coefficient of analyte (cm^2/s)

ν = scan rate (V/s)

When the scan rate is increased, the peak current increases as well, while the reaction remains reversible. To determine the electrode process controlled at

surface, peak currents are plotted versus square root of scan rate. If analyte is adsorbed on the electrode surface, peak current is associated with scan rate rather than square root of scan rate. However, this technique is normally used for analyte characterization and qualitative detection. This technique is not suitable for quantitative detection due to its low sensitivity and difficulty in distinguishing a peak between two or more analytes.

2.1.1.2 Differential pulse voltammetry (DPV)

DPV is an excellent technique for quantitative detection of organic and inorganic compounds. This technique offers more advantages when compared to other electrochemical techniques including high sensitivity and ability to discriminate peak between two and/or more analytes. Figure 3 shows DPV waveform, the fixed-magnitude pulses which superimposed on linear potential ramp are applied to working electrode. In this technique, the current is sampled at two points. The first point is before the pulse application (at t_1), and the second point is at the end of the pulse application when charging current has decayed (at t_2). The first current (i_1) is instrumentally subtracted from the second current (i_2), and the current difference ($\Delta i = i_1 - i_2$) is plotted versus the applied potential. Peak height obtained from DPV is directly proportional to the concentration of the corresponding analytes.

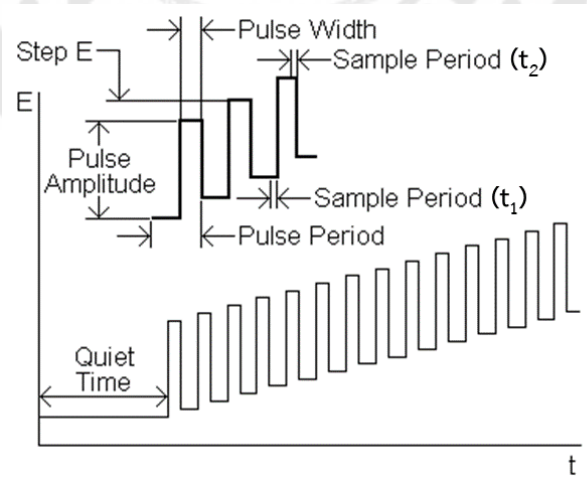

Figure 3 Illustration of DPV waveform

Source: Basinc. “Pulse Voltammetric Techniques.” Retrieved 14 January 2019, from https://www.basinc.com/manuals/EC_epsilon/Techniques/Pulse/pulse

2.1.1.3 Chronoamperometry

Chronoamperometric technique has been widely used for quantitative analysis, especially in flow-based measurement and chromatography. This technique works by applying a constant potential at working electrode, and resulting current is measured as function with time (Harvey, 2021). The potential waveform is shown in Figure 4a, where the potential is held, the electroactive specie is oxidized or reduced at working electrode surface and current dependent with time occurs. At the beginning of applied potential, this technique generates high charging currents, then resulting currents decay exponentially with time as shown in Figure 4b. Normally, average constant currents after charging current period associate with concentrations of analyte, these results are used for quantitative analysis. In addition, because the applied potential is fixed at a specific potential, chronoamperometry accomplished greater selectivity than others pulse techniques.

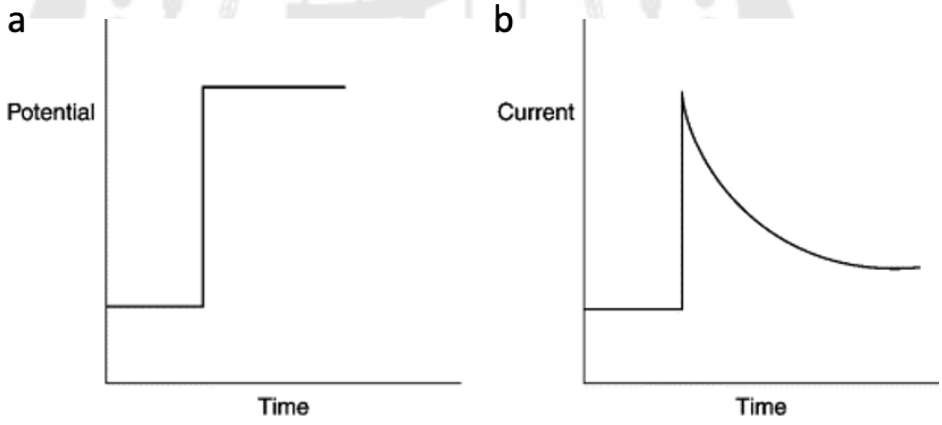

Figure 4 (a) Chronoamperometric waveform and (b) Typical chronoamperometry data

Source: Honeychurch, K. C. (2012). 13 - Printed thick-film biosensors M. Prudenziati & J. Hormadaly *Printed Films* (pp. 366-409): Woodhead Publishing.

2.1.2 Screen-printed electrode (SPE)

SPE is promising technology for analytical applications, which provides more advantages than traditional electrodes, including low cost of material, diverse geometries can be easily designed due to easy fabrication method, simple operation,

and requiring small amount of sample volume. Moreover, SPE is minimized to be a small device, it is capable for on-site analysis application. Many commercial sources of SPE are available in numerous configurations and it is convenient to fabricate using in-house screen-printing techniques and screen-printing machines. The pattern of SPE can be changed depending on applications. Figure 5(a) shows a commercial SPE, and Figure 5(b) shows an in-house SPE screened on poly(vinyl chloride) substrate. In addition, the electrode surface of SPE is easily modified to adapt for improvement of sensitivity and selectivity, making it useful in various applications.

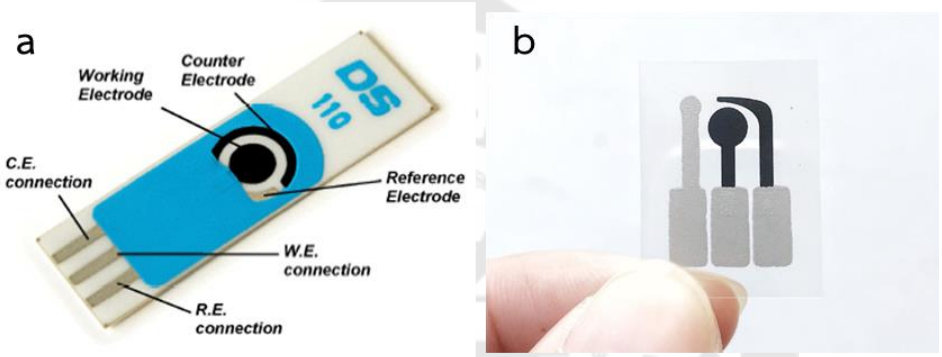

Figure 5 (a) Commercial SPE and (b) in-house SPE

Source: Dropsens. "Screen-printed electrodes." Retrieved 22 January 2019, from http://www.dropsens.com/en/screen_printed_electrodes_pag.html.

2.2 Microfluidic paper-based analytical device (μPAD)

The capillary-driven microfluidic devices have been attracted interest in the last several years because of their potential advantages involving inducing the flow in microchannel without the use of external pumps. Paper is one of the most common and popular material used to assemble microfluidic devices, this material itself exhibits several advantages, such as low-cost, flexibility, ease of fabrication and disposability(C. A. Chen et al., 2019; Elizalde, Urteaga, & Berli, 2015). μPAD is a powerful analytical platform fabricated from paper material. Typically, the solution flows inside a microfluidic channel through the cellulose structure of paper via capillary action without using an external pump. Because of this property, μPAD provides an outstanding analytical

platform for fluid handling and analysis for many kinds of applications. μPAD offers several advantages, such as cost-effectiveness, ease of use, portability and using small amounts of sample and reagent. Figure 6 shows the first introduction of simple μPAD was made for colorimetric detection by Whitesides 's group.

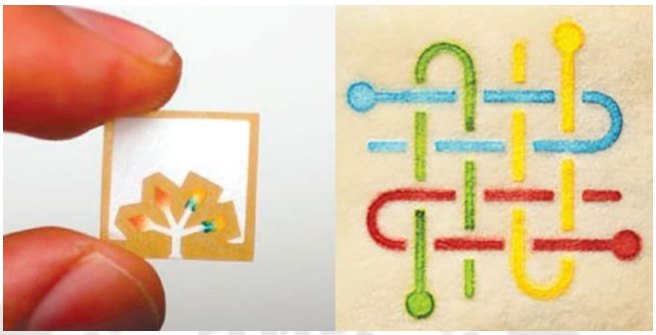

Figure 6 The design of μPAD for analytical application

Source: Martinez, A. W., Phillips, S. T., Whitesides, G. M., & Carrilho, E. (2010). Diagnostics for the developing world: microfluidic paper-based analytical devices. *Anal Chem, 82*(1), 3-10.

2.3 Origami paper-based analytical device (oPAD)

As 400 years of Origami, the Japanese art form created from paper-folding transforms a simple flat paper to various three-dimensional designs of the arts. Nowadays, modern origami paper technique has been adapted for analytical applications. Since, Liu and Crooks (H. Liu & Crooks, 2011) have proposed a new design of paper-based analytical tool known as oPAD. This method has been developed to improve analytical performance for several reasons. Instead of assembling multiple paper layers to generate an analytical device, oPAD creates from a single piece of paper by folding paper and stacking them together, simplifying and speeding up the fabrication processes. Furthermore, the oPAD creations enable analytical chemists to facilitate convenient analytical procedures by combining multiple steps and/or techniques into a single device. For example, Chen, et al. (C.-A. Chen et al., 2021) conducted multiple steps of enzyme-linked immunosorbent assay (ELISA) into a single three-dimensional oPAD, allowing for an all-in-one sample-to-answer solution (Figure 7).

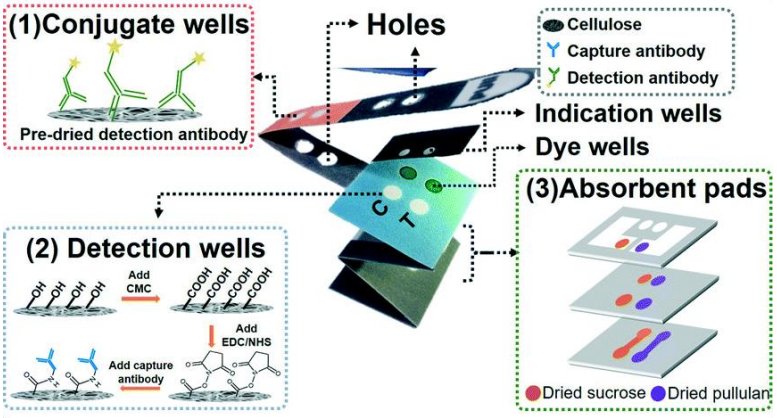

Figure 7 Components of 3D oPAD combined multiple reagents and preparation steps into a single device for ELISA system

Source: Chen, C.-A., Yuan, H., Chen, C.-W., Chien, Y.-S., Sheng, W.-H., & Chen, C.-F. (2021). An electricity- and instrument-free infectious disease sensor based on a 3D origami paper-based analytical device. *Lab on a Chip, 21*(10), 1908-1915.

2.4 Electrochemical paper-based analytical device

The challenge in improving μPAD and oPAD efficiency is to achieve a low LOD while maintaining good selectivity. The majority of studies proposed paper-based platform in conjunction with colorimetric detection. However, sensitivity and selectivity are poor. To overcome these problems, paper-based platform coupled with electrochemical detection has been developed to provide a good match in terms of sensitivity and selectivity (J. Adkins, Boehle, & Henry, 2015).

Dungchai et al. (Dungchai, Chailapakul, & Henry, 2009) published the first report on eμPAD for biological compounds detection. Since the first report, eμPAD has continuously increased at an exponential rate, becoming one of the most promising techniques for combining with μPAD. The eμPAD achieved various advantages including, inexpensive, portable and can be integrated with a smartphone. Moreover, when compared to a μPAD coupled with colorimetric detection, this device provided higher sensitivity and selectivity. In terms of improving the analytical performance, eμPAD has been used for many applications, including separation (Shiroma, Santhiago,

Gobbi, & Kubota, 2012), preconcentration (Nantaphol et al., 2017), and coupling with colorimetric detection or other techniques for dual detection (Rattanarat et al., 2014) as shown in Figure 8.

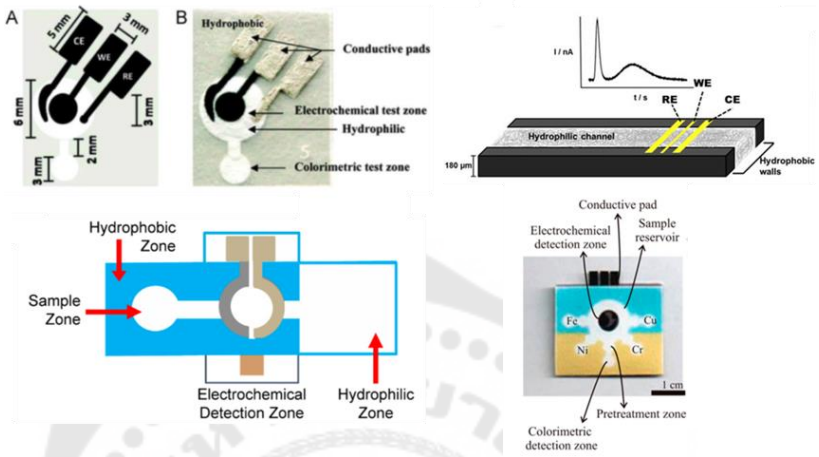

Figure 8 The image of eμPAD platforms for various applications

Source: Dungchai, W., Chailapakul, O., & Henry, C. S. (2009). Electrochemical detection for paper-based microfluidics. *Anal Chem, 81*(14), 5821-5826. Shiroma, L. Y., Santhiago, M., Gobbi, A. L., & Kubota, L. T. (2012). Separation and electrochemical detection of paracetamol and 4-aminophenol in a paper-based microfluidic device. *Anal Chim Acta, 725*, 44-50. Nantaphol, S., Channon, R. B., Kondo, T., Siangproh, W., Chailapakul, O., & Henry, C. S. (2017). Boron Doped Diamond Paste Electrodes for Microfluidic Paper-Based Analytical Devices. *Anal Chem, 89*(7), 4100-4107. And Rattanarat, P., Dungchai, W., Cate, D., Volckens, J., Chailapakul, O., & Henry, C. S. (2014). Multilayer paper-based device for colorimetric and electrochemical quantification of metals. *Anal Chem, 86*(7), 3555-3562.

However, the significant problems of μPAD when coupled with electrochemical detection is the decay of flow rate related with time, which results in low electrochemical current response and slow flow rate in microfluidic paper-based channels. In 2016, Adkins et al. (J. A. Adkins, Noviana, & Henry, 2016) developed eμPAD for quasi-steady flow detection at microwire electrodes to overcome the decay of flow rate related with time. They designed the eμPAD with a 270° fan shape connected to an inlet channel (as

shown in Figure 9a). Moreover, Channon et al. (Channon et al., 2018) developed multilayered μPAD coupled with electrochemical detection by fabrication of eμPAD with two layers of μPAD and used packing tape for sealing method (as shown in Figure 9b). The results offered a higher flow rate than compared to typical eμPAD platforms.

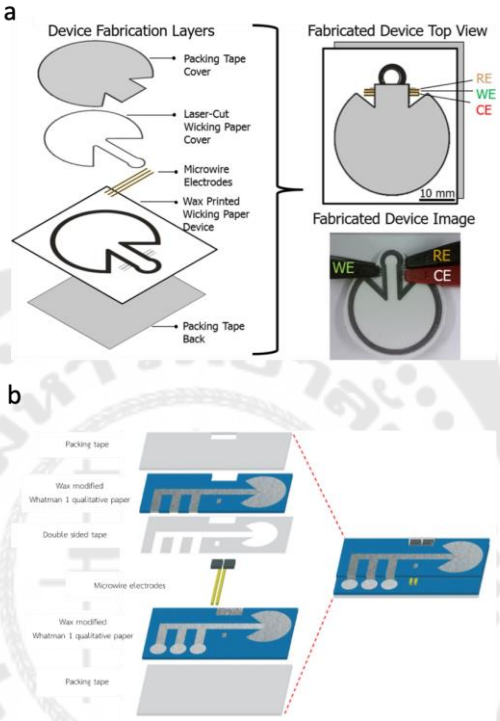

Figure 9 The components of (a) quasi-stationary flow eμPAD and (b) multilayered eμPAD

Source: Adkins, J. A., Noviana, E., & Henry, C. S. (2016). Development of a Quasi-Steady Flow Electrochemical Paper-Based Analytical Device. *Anal Chem, 88*(21), 10639-10647. And Channon, R. B., Nguyen, M. P., Scorzelli, A. G., Henry, E. M., Volckens, J., Dandy, D. S., & Henry, C. S. (2018). Rapid flow in multilayer microfluidic paper-based analytical devices. *Lab on a Chip, 18*(5), 793-802.

The numerous styles of electrochemical oPAD have been used for analytical application, not only provided high sensitivity but also offer more convenient for operation. Wang et al. (C. C. Wang et al., 2016) proposed oPAD inspired from pop-up greeting card. This oPAD was designed by separating sample preparation and

electrochemical detection zones, then it can be connected after folding paper from two zones together. This concept achieved high sensitivity for detection of biomarker as well as time-controlled of sample incubation prior to electrochemical measurements (Figure 10a). In addition, oPAD was applied with boron-doped diamond electrode (BDDE) for multistep modification and detection of metal compounds (Pungjunun et al., 2018). Instead of using inconvenient conventional BDDE configuration, this completed oPAD coupled BDDE was designed to offer a small single drop of sample and reagents (Figure 10b). In addition, the working area at BDDE surface can be controlled using this operational system, which allowed precise surface area during modification and detection.

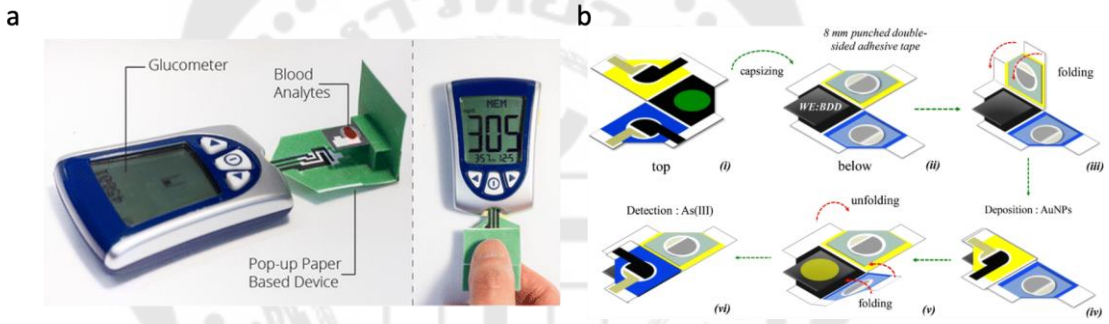

Figure 10 (a) oPAD inspired by pop-up paper coupled with screen-printed electrode and (b) an oPAD coupled BDDE for multistep electrochemical modification and total arsenic detection

Source: Wang, C. C., Hennek, J. W., Ainla, A., Kumar, A. A., Lan, W. J., Im, J., . . . Whitesides, G. M. (2016). A Paper-Based Pop-up Electrochemical Device for Analysis of Beta-Hydroxybutyrate. *Analytical Chemistry, 88*(12), 6326-6333. Pungjunun, K., Chaiyo, S., Jantrahong, I., Nantaphol, S., Siangproh, W., & Chailapakul, O. (2018). Anodic stripping voltammetric determination of total arsenic using a gold nanoparticle-modified boron-doped diamond electrode on a paper-based device. *Microchim Acta, 185*(7), 324.

2.5 Paper-based analytical device fabrication method

Fabrication method is based on patterning hydrophilic/hydrophobic on paper. Various techniques were proposed to fabricate paper-based devices, the criteria for selecting the method depended on cost and complication of process which involved chemical modification and/or physical deposition (Xia, Si, & Li, 2016). Currently, many fabrication methods have been proposed including photolithography, ink-jet etching, wax dipping, screen printing, wax printing, stamping and ink-jet printing. The advantages and disadvantages of each fabrication method are listed in Table 1 (Akyazi, Basabe-Desmonts, & Benito-Lopez, 2018).

Table 1 Comparison of paper-based device fabrication methods

Method fabrication	Advantages	Disadvantages
Photolithography	- High resolution of μPADs pattern	- Requirement of expensive tool - Requires washing steps to remove uncross-linked polymer
Ink-jet etching	- Low cost of equipment	- Requires multiple printing steps to create the μPADs pattern - Requires several steps for fabrication
Wax dipping	- Cheap and easy to fabricate	- Low reproducibility
Screen printing	- Simple fabrication method	- Low resolution of μPAD pattern - Requires difference screen for making difference patterns
Wax printing	- Simple and fast to fabricate	- Low resolution of μPADs pattern - Requires high temperature for heating step
Stamping	- Low cost and simple of tool	- Low resolution of device pattern

Table 1 (Continued)

Method fabrication	Advantages	Disadvantages
Ink-jet printing	- High resolution of μPADs pattern - Requires a simple desktop printer	- Requires modified ink - Requires high temperature for heating step

Wax printing was chosen in this study due to low cost, simplicity, rapidity and lack of mask requirement. Furthermore, this method requires only graphic software to generate the pattern. Figure 11 depicts a wax printing procedure to fabricate paper-based device. The solid wax can be directly printed onto the paper. Then, solid wax is melted into a cellulose structure of paper using an oven, hot plate, or heat gun to separate between hydrophobic and hydrophilic areas. This fabrication method also shows less steps for fabrication compared to the other methods.

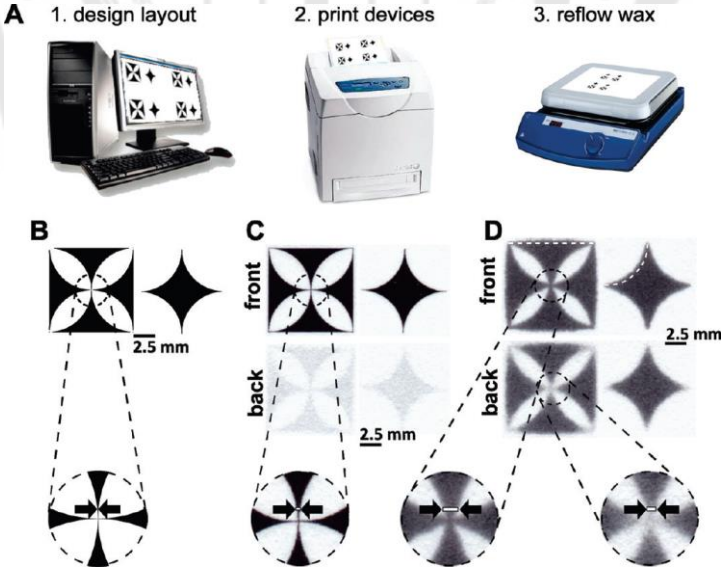

Figure 11 Wax printing method for fabrication of μPAD.

Source: Carrilho, E., Martinez, A. W., & Whitesides, G. M. (2009). Understanding wax printing: a simple micropatterning process for paper-based microfluidics. *Anal Chem, 81*(16), 7091-7095.

2.6 Lamination-based microfluidic device

Although μPAD has demonstrated a promising flow-based platform for broadly analytical applications in several years, the inefficiency persists due to some limitations such as, difficulty in controlling flow rate, non-uniform flow, and sample and/or reagents lost during solution delivery. As a result of these issues, some applications are restricted (Jang et al., 2021; Nguyen, Meredith, Kelly, & Henry, 2018). To overcome the limitations, alternative materials and fabrication methods are required to develop a capillary-driven microfluidic devices. Instead of using μPAD, a lamination-based fabrication method was proposed to generate self-pumping microchannel. Several lamination methods were used to stack multilayer of material substrate to create microchannel such as plasma bonding (da Costa et al., 2014), toner (De Souza, Alves, & Coltro, 2012), and adhesive film (Channon et al., 2018; Andres W. Martinez, Phillips, & Whitesides, 2008). Also, for substrate, various materials such as glass slide (Channon et al., 2021), acrylic (Islam, Natu, & Martinez-Duarte, 2015), and polyester film (Jang et al., 2020) were selected to fabricate microfluidic device. Among these materials, the use of double-sided adhesive film (DSA) as a lamination method and polyester film as a substrate material are great combinations for development of capillary-driven microfluidic devices. Because they are common and inexpensive materials. Moreover, they exhibit a simple fabrication to generate device.

Figure 12a shows a simple design of capillary-driven microfluidic device fabricated by lamination-based method using multilayer stacking of polyester film and DSA. The channel height (Figure 12b) can be adjusted by varying the numbers of polyester films and DSA layers. Capillary-driven microfluidic device that was developed by Henry group was designed in drawing software (CorelDRAW X4, Corel) and generated channel templates of polyester film and DSA using CO_2 laser cutter. Unlike μPAD, that solution flows through cellulose of paper, this fabrication method shows a great uniform flow to transport solution in microchannel through the gap between each polyester film that binds by DSA layer without using external pump.

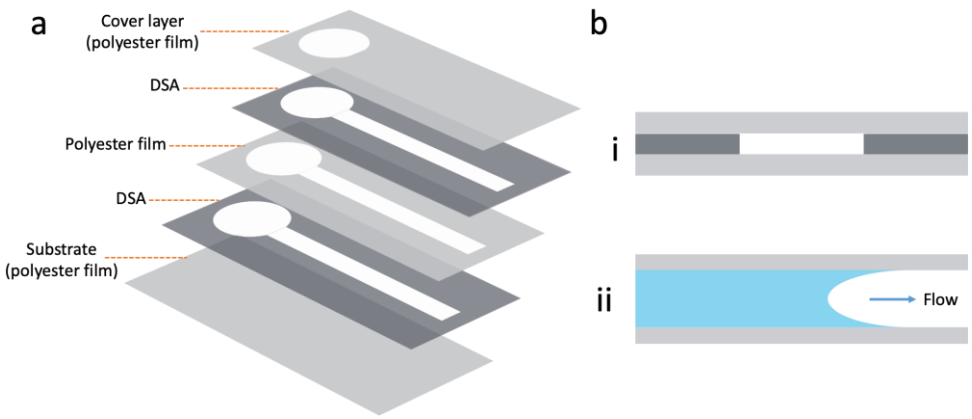

Figure 12 (a) Components of capillary-driven microfluidic device generates from multiple stacking of polyester film and DSA (b) The device with (i) cross-sectional view and (ii) side-sectional view

2.7 Dopamine (DA)

DA is one of the most important neurotransmitters that is produced by nerve cells known as neurons. Its function is used to communicate messages from the central nervous system to the brain and transmit signals from the brain to the external environment (Konkel, 2018). The DA function is primarily responsible for movement control, attention, learning, emotional responses and blood pressure regulation. DA, also called hydroxytyramine (Figure 13), is a nitrogen-containing compound that can form as an intermediate compound from dihydroxyphenylalanine (dopa) during the metabolism of amino acid tyrosine (Augustyn et al.). In the mechanism pathway, DA is a precursor for synthesis of norepinephrine and epinephrine. The deficiency of DA level due to the progressive degeneration of neuron cells in the substantia nigra is associated with several diseases such as Parkinson's disease, Huntington's disease, Alzheimer's disease, Attention-Deficit Hyperactivity Disorder and Schizophrenia (Triarhou, 2013). Generally, DA level is determined via blood testing and 24 hours urinary measurements (Sawka, Jaeschke, Singh, & Young, 2003). Thus, a simple, sensitive, selective, and fast analytical method for detection and monitoring of DA concentration in biological samples is a key element for the development of an analytical system for assisting

doctors in diagnosing and monitoring these diseases using DA level results from clinical tests.

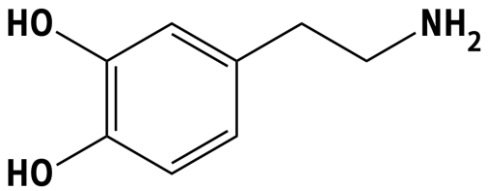

Figure 13 Chemical structure of DA

2.8 L-Cysteine (Cys) in Halal foods

Detection of food additive ingredients has gained remarkable attention in several years. Especially, the monitoring of food additive ingredients directly relates to quality of food products in the industrial scale, where high precision is required to ensure consistent product quality in every batch before launching it to the market. In consumer perspective, concerning of contamination of unacceptable ingredients in some communities such as, Muslim population is major concern in this decade. Where in some regions of the world attempt to reduce the cost of food production by using low-cost ingredients derived from prohibited things according to religious regulation. The development of promising analytical tools for determination of food additive ingredients for food quality control as well as for monitoring and raising awareness of forbidden ingredient contamination in religious food is strongly demanded.

2.8.1 Halal foods

Over 3 billion people worldwide are Muslims who reach out to the Halal industries, one of the biggest and fastest growing industries globally. Halal refers to the things approved by Islamic law, including, food, beverage, and activities associate with the Muslim lifestyle, and the Halal industry covers finance, logistics, and tourism. Particularly in food, the Halal food industry accounts for 16.6% of the global food market, generating billions of dollars each year. At the beginning, Halal foods were thought about Muslim foods that were free from alcohol and pork. Nowadays, Halal foods include food safety requirements and ingredients which are free from forbidden things according to Islamic law such as any part of the human body, toxic ingredients, blood,

dead animals, carnivorous animals, and animals that have not been slaughtered in the name of Allah. From the numerous requirements, many countries certified Halal status on Halal food packages (Figure 14) to ensure and offer more convenience for customers in selecting foods that are free from any prohibited ingredients under Islamic law.

Figure 14 Examples of Halal status labeled on food product package that are certified by Halal organizations from several countries around the world.

Source: “Halal Certification for Food, Cosmetics and Pharmaceutilcal products.” Retrieved 8 July 2021, from https://www.halalcs.org/en/#section-1259

Nowadays, the export of Halal food products is not limited to Muslim countries; Halal is exported to the global Muslim community in non-Muslim countries, such as, Canada, France, New Zealand, and Australia. Awareness and investigation of the ingredients in Halal food products at the primary production before launching to consumers have to be a priority to control and protect the Muslim community from ingredients that are forbidden under Islamic law.

The modern analytical approaches used for Halal food analysis have been booming for many years. Researchers used hi-end technologies to provide high accuracy and precision, as well as robustness methods for routine analysis. For example, the use of protein-based methods and DNA analysis for detection of pork derivative adulteration in meat products (Ballin, Vogensen, & Karlsson, 2009). Other

methods such as HPLC coupled with MS (Von Bargen, Dojahn, Waidelich, Humpf, & Brockmeyer, 2013), fourier transform infrared spectroscopy (FTIR) (Xu, Cai, Cui, Ye, & Yu, 2012), and fluorescence microscopy (Kelly, Tarbin, Ashwin, & Sharman, 2006) have been developed for Halal food investigation. However, the requirements of the new trends in modern food analytical methods are based on low-cost, simple and miniaturization that can provide for on-site analysis application.

2.8.2 L-Cysteine (Cys)

Cys is a sulfhydryl amino acid (Figure 15) that mainly found in many food sources mostly in high protein, such as dietary products, egg, beef, chicken, and whole grain. In the food industry, Cys or E920 has been used as a food additive in the bakery industry for several decades. Because of the benefits of Cys that is used to break-up disulfide bonds of gluten network in flour during bakery production. Cys function reduces required-time for dough relaxation, instead of left-over it for several hours. In addition, it provides a softened texture after baking as well (Reuben, 2009). However, raw material of Cys sources might be an essential issue for religious consumers like Muslim. Most of Cys is extracted from cheap abundant protein sources, including human hair, features, bristles or hooves from animals. When these sources dissolve in acid solution to isolate Cys via simple chemical processes known as keratin hydrolysis. As mentioned in the Halal food section, Muslim does not allow to consume Cys derived from these sources. Even recently, Cys is extracted through an enzymatic reaction from bacteria fermentation, but the cost is still more expensive than other sources. Hence, concerning of Cys sources led to many Muslim country banned this substance as food additive, in order to protect Muslim from the thing that was suspected follows by Islamic law.

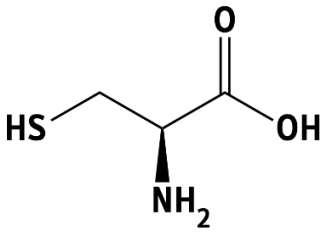

Figure 15 Chemical structure of Cys

2.9 SARS-CoV-2

The outbreak of COVID-19 all over the world has caused 240 million infections, resulting in more than 4 million deaths by November 2021. All social activities as well as national economies and businesses have been disrupted due to the lockdown regulation to tackle the spread of virus. Generally, SARS-CoV-2 is easily transmitted from person to person via mucus from infected patients. In patients suffering from mild illness, the most common symptoms are cold, fever, cough and loss of taste. Moreover, severe syndromes such as pneumonia and acute respiratory distress can be found in some patients, posing a risk of death (Rasmi, Li, Khan, Ozer, & Choi, 2021). Meanwhile, some patients are asymptomatic. Even currently, vaccines have been developed to fight the virus. However, the numbers of the vaccinated population are confined in high income countries. On the other hand, vaccines are still highly demanded in middle- and low-income countries. To reduce the numbers of COVID-19 patients by isolating infected individuals from the community, rapid, low-cost, and high accuracy of COVID-19 diagnostic testing remains the major key solution.

Numerous laboratory tests have been used for diagnostic and screening COVID-19 patients. RT-qPCR is a routine gold standard method that used for confirming infected cases. Even though this method provides high sensitivity and selectivity, it is expensive, requires specialists to operate and analyze results, and takes a long-time consuming. Currently, the idea of low-cost and rapid COVID-19 diagnostic tests has gained attention, despite it offers lower sensitivity. As shown in Figure 16 RT-qPCR test has low-frequency rate for testing due to the inconvenient method, owing to the probability that infected people are unaware that they are infected from a virus during an infectious period. In comparison, low-cost diagnostic tools provide high-frequency rate testing that offer patients to learn faster that they are infected by a virus to isolate themselves from the community (Mina, Parker, & Larremore, 2020).

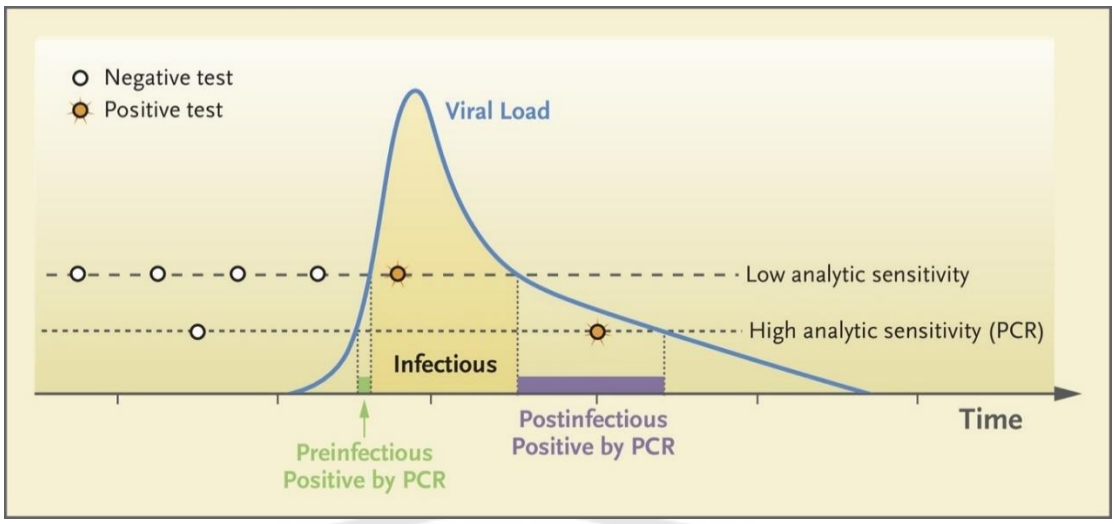

Figure 16 Diagram shows frequency testing of high sensitive method (RT-qPCR) versus low sensitive method in order to verify positive cases.

Source: Mina, M. J., Parker, R., & Larremore, D. B. (2020). Rethinking Covid-19 Test Sensitivity — A Strategy for Containment. *New England Journal of Medicine, 383*(22), e120-e120.

2.9.1 Serology testing

Immunological testing, also known as serology testing, is one of promising analytical approaches for determination of antibody immune response produced against the virus in infected patients. This type of method can detect immunoglobulin M (IgM), and immunoglobulin G (IgG) directed against SARS-CoV-2 in human blood samples. After infection from SARS-CoV-2 virus, usually around 7-10 days, the immune system in the human body produces IgM and IgG antibodies to fight the virus, respectively. IgM and IgG can be found in detectable concentration within a period from 5 days to 2 weeks. The antibody level results advantage to support others testing such as antigen and nucleic acid detection to reduce false-negative results (Seunghyeon Kim et al., 2021). In addition, because IgM and IgG antibodies remain longer in bloodstream than antigen or viral RNA, the serology assay has potential to monitor the SARS-CoV-2

antibody in humans on late-stage, post-infection and/or after vaccination (Kasetsirikul et al., 2020).

2.9.2 Enzyme-Linked Immunosorbent Assay (ELISA)

ELISA is commonly an immunological assay for detecting antigens, antibodies, protein hormones and glycoproteins. Many variants of ELISA strategy have been developed for different situations depending on application, such as direct ELISA, indirect ELISA, sandwich ELISA and competitive ELISA ("Overview of ELISA,"). Based on our work, the principle of ELISA technique includes four steps in order as shown in Figure 17. This assay relies on a specific capture protein that binds with target analyte. Then, the detection system produced through enzymatic or chemical reaction is labeled with secondary antibodies that bind to target analytes that already bind to substrate. The labeled secondary antibody is used to quantify concentration of target analyte by generating several kinds of signal such as colorimetric readout, fluorescence, chemiluminescence and electrochemical responses. Generally, ELISA system is conducted on a special absorbent plate to ensure the capture stick on plate surface. All experimental steps are completed in a single plate, leading to ELISA being one of the most popular techniques for immunological analysis (Horlock).

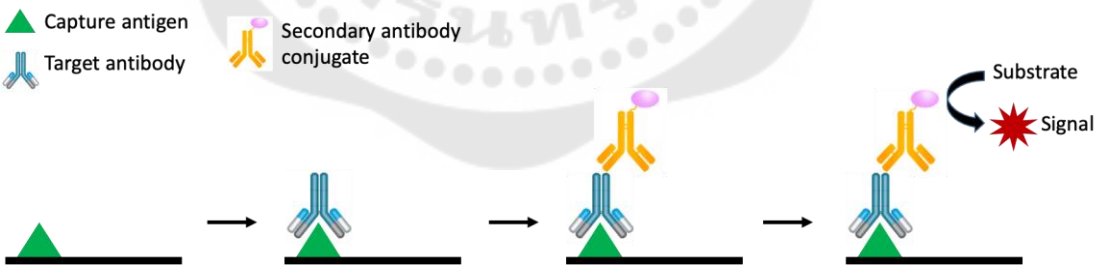

Figure 17 ELISA format includes simple four experimental steps for detection of antibody

The labeled secondary antibody or detection antibody is a significant factor for generating signals that can be used to quantify the amount of target analytes. Secondary antibody is usually labelled with Alkaline phosphatase (ALP), β-galactosidase, or horseradish peroxidase (HRP) and used a chemical substrate to

produce measurable response via enzymatic reaction. The selection of chemical substrates depends upon detection methods, such as spectrometry, fluorescence, chemiluminescence or electrochemical technique ("ELISA Fundamental Principle, How It Works,") The example of substrates, such as 3,3',5,5'-tetramethylbenzidine (TMB), *O*-phenylenediamine (OPD), 3, 3' diaminobenzidine tetrahydrochloride (DAB) and 2,2-azino-bis(3-ethylbenzthiazoline-6-sulfonic acid) (ABTS). The choices of enzyme labelled secondary antibodies enable the ELISA for widely analytical applications. As well as a simple operational system offer it to perform on-site analysis and rapid diagnosis (Zhan, Wu, Yang, & Huang, 2014).

2.9.3 Lateral flow immunoassay (LFIA)

The achievement of fast and accurate immunoassay for diagnostic testing at an early stage of infectious diseases is very important. It can evaluate the large numbers of results in a short period of time, which provides a great advantage in a pandemic crisis. LFIA has become one of the most abundant strategies for qualitative and quantitative analysis for clinical diagnosis. Typical LFIA components include sample pad, conjugate pad, nitrocellulose membrane (NCM) and waste pad, where captured protein and labelled secondary antibody are immobilized on NCM and conjugate pad, respectively (Sajid, Kawde, & Daud, 2015). All reagents immobilized on LFIA become active when sample solution flows along the device. However, the lack of sensitivity from common LFIA using naked eye readout and colorimetric detection is the major issue. Thus, several formats and detection methods have been proposed to improve LFIA performance. As shown in Figure 18a, Preechakasedkit et al. (Preechakasedkit, Siangproh, Khongchareonporn, Ngamrojanavanich, & Chailapakul, 2018) established an automating sequential delivery device using wax-printing technology to combine multiple procedures into a single device. This platform overcame some limitations that exhibited from conventional LFIA. Moreover, a few reports integrated LFIA with SPE for highly sensitive and selective electrochemical detection (Dempsey & Rathod, 2018) instead of using colorimetric readout as shown in Figure 18b.

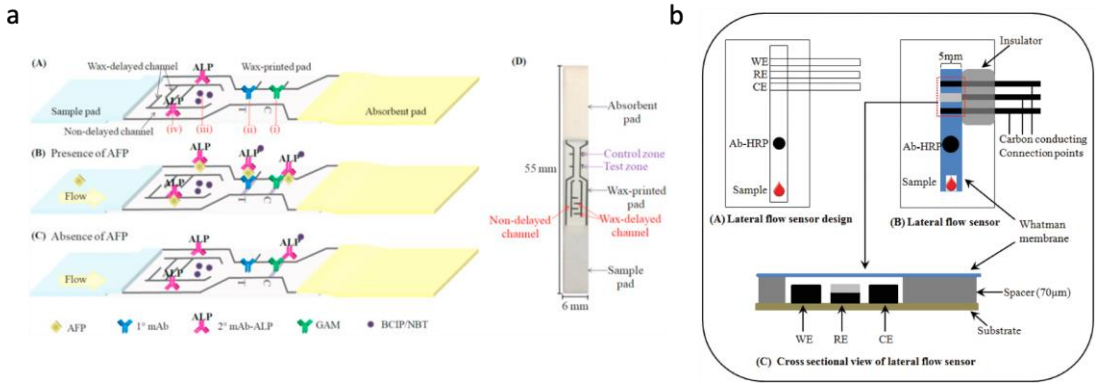

Figure 18 (a) Automating sequential delivery LFIA devices (b) SPE integrated LFIA format for electrochemical detection

Source: Preechakasedkit, P., Siangproh, W., Khongchareonporn, N., Ngamrojanavanich, N., & Chailapakul, O. (2018). Development of an automated wax-printed paper-based lateral flow device for alpha-fetoprotein enzyme-linked immunosorbent assay. *Biosensors and Bioelectronics, 102*, 27-32. And Dempsey, E., & Rathod, D. (2018). Disposable Printed Lateral Flow Electrochemical Immunosensors for Human Cardiac Troponin T. *IEEE Sensors Journal, 18*(5), 1828-1834.

CHAPTER 3
METHODOLOGY

In this chapter, the experimental of development of miniaturized electrochemical devices can be divided into two parts. The first part is development of electrochemical paper-based analytical devices for clinical and food applications, and there was generated into two subprojects. The first subproject is a multilayer microfluidic paper coupled with an electrochemical platform developed for sample separation and detection of dopamine. The second subproject is a novel L-cysteine sensor using in-situ electropolymerization of L-cysteine: potential to simple and selective detection. The second part is development of electrochemical device for COVID-19 diagnosis. In this part presents an electrochemical capillary-flow immunoassay for detecting anti-SARS-CoV-2 nucleocapsid protein antibodies at the point of care. Each project contained chemicals, materials, apparatus, fabrication methods, and system operations.

3.1 A multilayer microfluidic paper coupled with an electrochemical platform developed for sample separation and detection of dopamine

The contents of this section are based on the original research article (Khamcharoen & Siangproh, 2021), see in appendix 1 for the full article.

3.1.1 Chemicals, materials, and apparatus

All chemicals used in this work were of analytical grade and used without any purification. DA, AA, uric acid, Nafion, l-glutamic acid, bovine serum albumin (BSA), potassium ferricyanide [$K_3Fe(CN)_6$], sodium chloride (NaCl), calcium chloride ($CaCl_2$), and vitamins B_2 and B_6 were purchased from Sigma-Aldrich (St. Louis, MO, USA). Glucose was obtained from Merck (Darmstadt, Germany). Artificial urine sample was purchased from Carolina Biological Supply Company (Burlington, USA). Phosphate buffer solution (PBS) (0.1 M), used as the supporting electrolyte, was prepared using sodium dihydrogen orthophosphate ($NaH_2PO_4.2H_2O$) and disodium hydrogen orthophosphate ($Na_2HPO_4.2H_2O$), which were obtained from Ajax (Australia). N-propanol was purchased from Unilab (Mumbai, India). All aqueous solutions were prepared in deionized (DI) water.

Electrochemical techniques, such as cyclic voltammetry (CV) and differential pulse voltammetry (DPV) were performed using potentiostat CHI 1200C (Austin, TX, USA). Electrochemical impedance spectroscopy (EIS) was employed to confirm the successful modification of the electrodes using PalmSens4 (Houten, The Netherlands). Graphene and silver/silver chloride (Ag/AgCl) inks were purchased from Sun Chemical (Slough, United Kingdom). The screen-printed blocks were generated by Chaiyaboon Co. Ltd. (Bangkok, Thailand). The eμPAD pattern was fabricated using Xerox Color Qube 8570 series wax printing machine (Xerox, Japan). The Silcot cotton pad was purchased from Unicharm Products Co., Ltd. (Tokyo, Japan), and the packing tape was purchased from 3M Thailand Company (Bangkok, Thailand).

3.1.2 Design and preparation of eμPAD

The eμPAD pattern was designed using Adobe illustrator CC. Thereafter, the wax pattern was printed on the Whatman Grade 1 filter paper using a wax printing machine. Subsequently, the wax-printed paper was placed on a hot plate at a temperature of 175°C for 30 s, for melting the wax into the cellulosic structure of the paper to differentiate between the hydrophobic and hydrophilic areas. For the electrochemical detection zone, three electrodes, namely, working, reference, and counter electrodes were screened by in-house screen printing. First, the graphene ink was screened on the detection zone, as shown in Figure 19a, to obtain the working and counter electrodes and placed in the oven at a temperature of 55°C for 30 min. Subsequently, the Ag/AgCl ink was screened on the detection zone to complete the electrochemical cell, as shown in Figure 19a, and placed in the oven at a temperature of 55°C for 30 min. Figure 19b illustrates the μPAD coupled with electrochemical detection consisting of the sample zone (cycle, diameter = 10 mm), electrochemical detection zone (cycle, diameter = 12 mm), and microfluidic channel that is connected between the previously mentioned zones (channel, 3 mm × 5 mm).

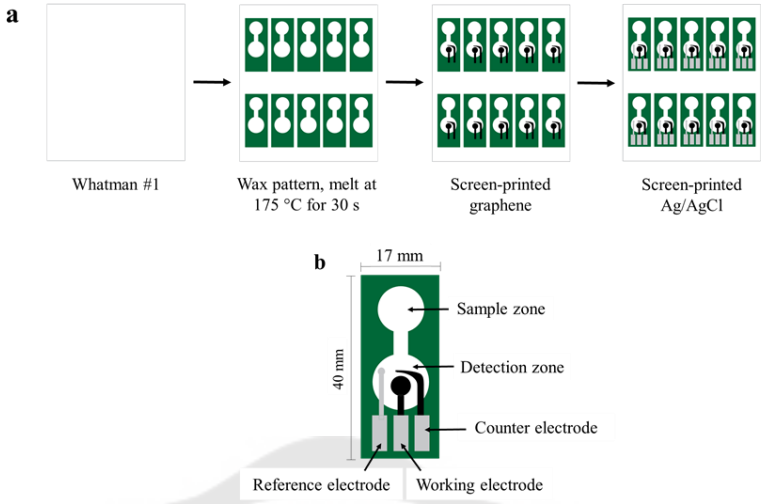

Figure 19 (a) The preparation of wax-patterned paper (b) drawing of μPAD coupled with electrochemical detection

3.1.3 Components of the eμPAD

The eμPAD has four layers (Figure 20); the two layers of packing tape, which were used to seal the top and bottom parts of the device to increase the flow rate and to prevent leakage and volatilization of the sample solution; (ii) a round cotton pad (circle, diameter = 10 mm), which was placed on the electrochemical detection zone to generate a quasi-steady flow rate on the device for the whole experiment; and (iii) the eμPAD layer, in which PGA was modified on the SPGE and 0.5% Nafion was drop-cast on the sample zone and microfluidic channel.

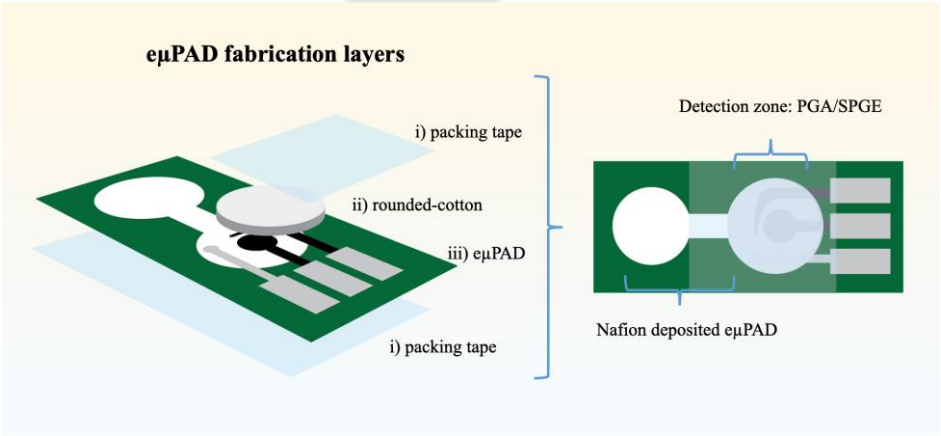

Figure 20 Illustration of eμPAD layers, fabricated from i) packing tape, (ii) rounded-cotton pad and iii) eμPAD layer.

3.1.4 Operation of eμPAD and procedure for electrochemical detection of DA

For operation, the bottom part of the eμPAD was sealed using a packing tape (Figure 21a). The surface of SPGE was modified with PGA was on by electropolymerization of 20 mM of glutamic acid in 0.1 M PBS (pH 7.4); thereafter, 100 μL of the modifier was dropped on the detection zone and potential was applied from -0.5 to +1.6 V using CV with a scan rate of 0.1 V/s for 7 cycles (Figure 21b). The eμPAD was rinsed with DI water and dried at room temperature. Thereafter, 0.5% Nafion was prepared in n-propanol, and 10 μL of the solution was drop-casted on the sample zone and microfluidic channel (Figure 21c) and dried at room temperature. Finally, the round cotton pad was placed onto the electrochemical detection zone, and the top part of the device was sealed with a packing tape (Figure 21d).

For the detection of DA, 60 μL of the DA solution in 0.1 M PBS (pH = 7.4) was dropped on the sample zone and was allowed to stand for 15 min (Figure 21e). In this step, the solution flowed from the sample zone through the microfluidic channel to the electrochemical detection zone by capillary force. Subsequently, electrochemical detection was conducted by DPV using PGA/SPGE as the working electrode, Ag/AgCl as the reference electrode, and SPGE as the counter electrode. The parameters for the DPV measurement were as follows—an increment of 0.006 V, a pulse amplitude of 0.2 V, a pulse width of 0.1 s, and a pulse period of 0.6 s, with the potential varied from −0.4 to +0.4 V versus Ag/AgCl. The differential pulse voltammogram of DA is shown in Figure 21f.

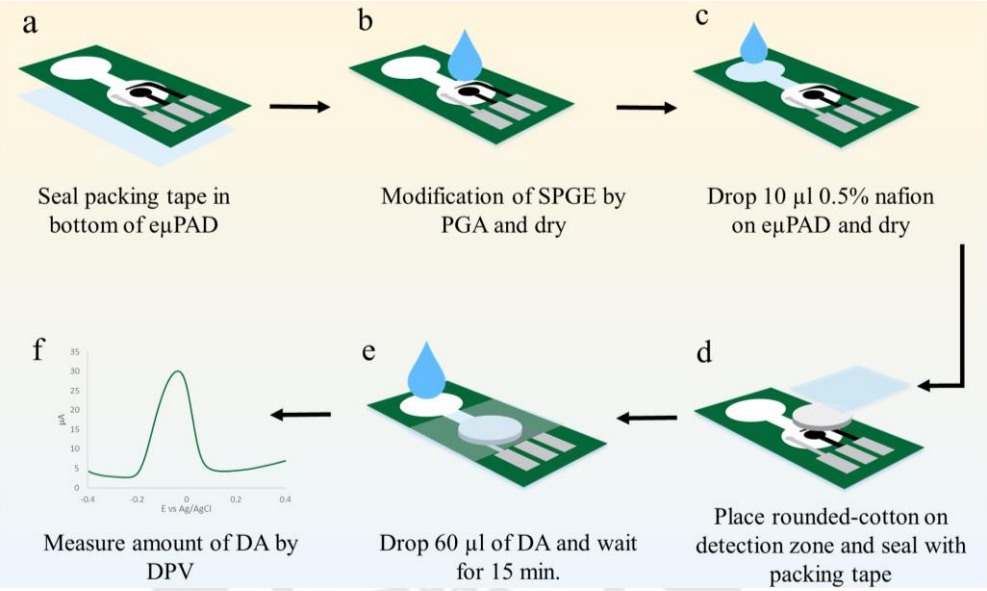

Figure 21 The representation of eμPAD for DA detection consisting of: (a) sealed packing tape at the bottom of eμPAD, (b) PGA modified SPGE step, (c) drop casting of 0.5% Nafion (d) completed multilayer eμPAD components, (e) determination of DA step and (f) differential pulse voltammogram of DA.

3.1.5 Determination of DA in real samples

To demonstrate the capability of the proposed eμPAD, it was evaluated for the detection of DA in artificial urine samples. The samples were diluted in PBS (pH 7.4), Thereafter, DA was spiked into the samples at concentrations of 10, 20, 40, 60, and 80 μM. The quantity of DA was measured using eμPAD; the recoveries of spiked standard DA were thoroughly studied. To confirm the accuracy of this device, the results obtained from the eμPAD were compared with those obtained using UV–Vis spectroscopy (Guo, Zhang, & Li, 2009).

3.2 A Novel L-cysteine sensor using in-situ electropolymerization of L-cysteine: potential to simple and selective detection

The contents of this section are based on the original research article (Khamcharoen, Henry, & Siangproh, 2022), see in appendix 2 for the full article.

3.2.1 Chemicals, materials and apparatus

L-cysteine, potassium ferricyanide ($K_3Fe(CN)_6$), sodium chloride (NaCl), calcium chloride ($CaCl_2$), l-ascorbic acid, D-glucose, D-sucrose, D-fructose, and folic

acid were purchased from Sigma-Aldrich (St. Louis, MO, USA). Nicotinic acid came from Hi-Media Laboratories Pvt. Ltd. (India). Thiamine came from Ajax (Australia). A 0.1 M Phosphate buffer solution (PBS), used as a supporting electrolyte, was prepared using sodium dihydrogen orthophosphate ($NaH_2PO_4.2H_2O$). di-Sodium hydrogen orthophosphate ($Na_2HPO_4.2H_2O$) came from Ajax (Australia). All aqueous solutions in this experiment were prepared in deionized (DI) water.

The electrode surface morphology was studied using a JSM-IT100 scanning electron microscope (SEM) (JEOL Ltd., Japan). The electrochemical measurement, using cyclic voltammetry (CV) and differential pulse voltammetry (DPV), was performed at room temperature on a CHI 1200C potentiostat (Austin, TX, USA). Electrochemical impedance spectroscopy (EIS) was used to characterize the electrode surface to confirm the successful modification using PalmSens4 (Houten, The Netherlands). A three-electrode system was fabricated by in-house screen-printing, silver/silver chloride (Ag/AgCl) and graphene inks were bought from Sun chemical (Slough, United Kingdom). The screen-printed blocks were produced by Chaiyaboon Co. Ltd. (Bangkok, Thailand). A three-dimensional (3D) oPAD pattern was generated using a Xerox Color Qube 8570 series wax printer (Xerox, Japan).

3.2.2 oPAD design and construction

An oPAD pattern was initially drawn using Adobe Illustrator CC software. The wax pattern was printed onto Whatman No.1 filter paper using a wax printer. Then the wax-printed paper was placed on a hot plate at temperature = 180 ºC for 30 s to allow wax diffusion into the paper's pore structure to create a hydrophobic feature on filter paper. Three SPGE electrodes were manually screened on paper using an in-house screen-printing method, as shown in Figure 22a. First, graphene ink was screened on paper to create working and counter electrodes, the geometric surface area of the working electrode is equal to 0.126 cm^2. Then the paper was placed into the oven at 60 ºC for 30 min. Ag/AgCl ink was screened on paper to create a reference electrode and conductive connecters. Then the completed paper was placed into the oven at temperature = 60 ºC for 30 min. Figure 22b shows the completed paper consists

of a working electrode, counter electrode, and reference electrode screened on wax-patterned paper (wide = 7 cm and height = 3 cm). The oPAD is ready for next electropolymerized modification and Cys detection without electrode pretreatments.

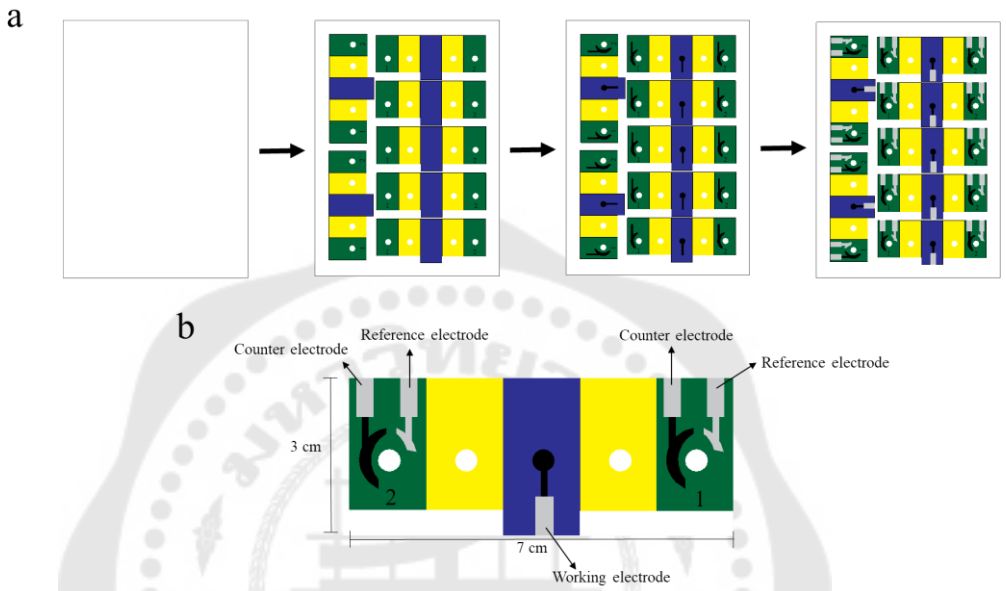

Figure 22 (a) Schematic demonstrates the preparation of origami electrochemical paper-based analytical device (b) The components of screen-printed electrode on origami paper-based analytical device

The newly designed oPAD was compared to the conventional electrochemical paper-based analytical device (ePAD), as shown in Figure 23a. The conventional ePAD proposed from previous reports (Charoenkitamorn, Chaiyo, Chailapakul, & Siangproh, 2018; Panraksa, Siangproh, Khampieng, Chailapakul, & Apilux, 2018; Pungjunun et al., 2019) had two main drawbacks that yielded poor electrochemical results. First, the electrodes were screened on the hydrophilic area of the paper, which has heterogeneous and different porosity to each device (Punjiya, Moon, Matharu, Rezaei Nejad, & Sonkusale, 2018). Second, some chemical compounds can be adsorbed into cellulose fiber of paper in hydrophilic areas (Punjiya et al., 2018; Renault, Li, Fosdick, & Crooks, 2013). Both reasons leading to low reproducibility and reliability for device-to-device. To overcome these limitations, we have developed an

oPAD by printing three electrodes on the hydrophobic area of a paper device (Figure 23a). Then, we constructed a spacer layer at the device for creating the solution reservoir (Figure 23b). This layer enables the solution to remain onto the working electrode surface and aligns three electrodes in the same planar during modification and detection, which is easier for the operation. The components of a single oPAD are shown in Figure 23b consists of; modification pad, spacers, detection pad, and working pad. Our new device is divided by 3 pads. The working pad is located at a center. The modification and detection pads were separated from each other to prevent Cys contamination from electropolymerization step to the Cys detection step.

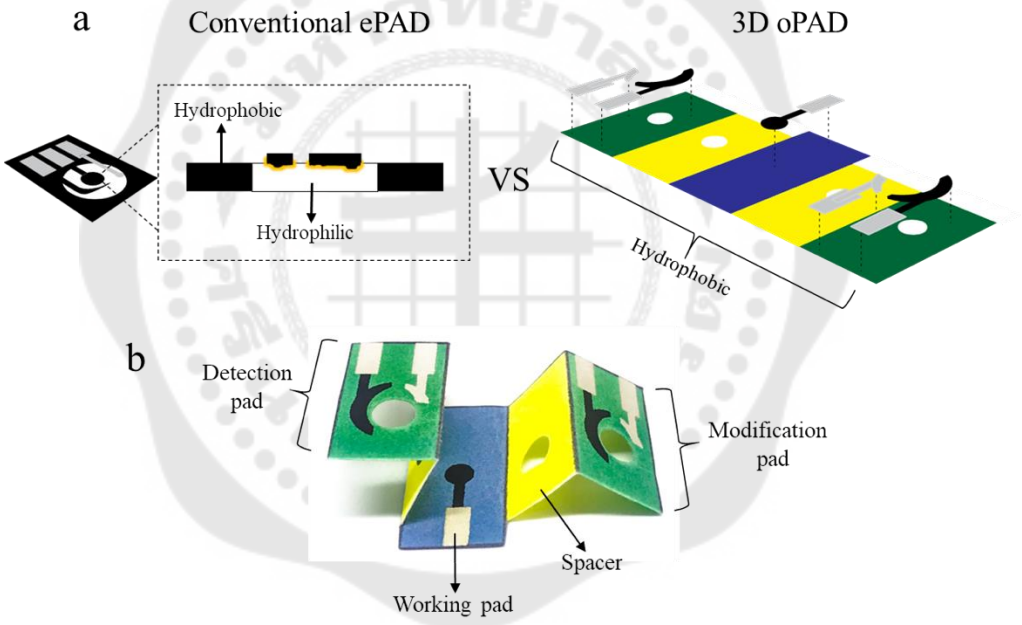

Figure 23 (a) The comparison configurations of a conventional ePAD vs. a new oPAD and (b) the components of oPAD including modification pad (green layer), spacers (yellow layer), detection pad (green layer) and working pad (blue layer)

3.2.3 Modification and detection procedure

The oPAD operational processes are shown in Figure 24. A hole was added as indicated by the white circle (hole diameter = 4 mm) (Figure 24a). Then the modification pad was folded down to cover the working pad (Figure 24b). Next, poly(Cys) was electropolymerized on SPGE by dropping 120 µL of 3 mM Cys in PBS at

pH = 8.0 onto the device (Figure 24c) and applying a potential using CV by sweeping the potential from -0.6 V to +2.0 V for 9 cycles at scan rate = 100 mV/s (Ferraz, Leite, & Malagutti, 2016). Afterward, the poly(Cys) film growth onto the electrode surface was rinsed with DI water and the modification side was torn off (Figure 24d). For the detection step, the paper at the detection pad was folded over the working pad (Figure 24e). Then, 120 µL of samples in PBS at pH = 8.0 was added to the device. The electrochemical measurement was performed by DPV (Figure 24f). The three-electrode system, including poly(Cys) modified SPGE served as a working electrode, SPGE served as a counter electrode, and Ag/AgCl served as a reference electrode. The total analysis time is around 10 minutes per sample.

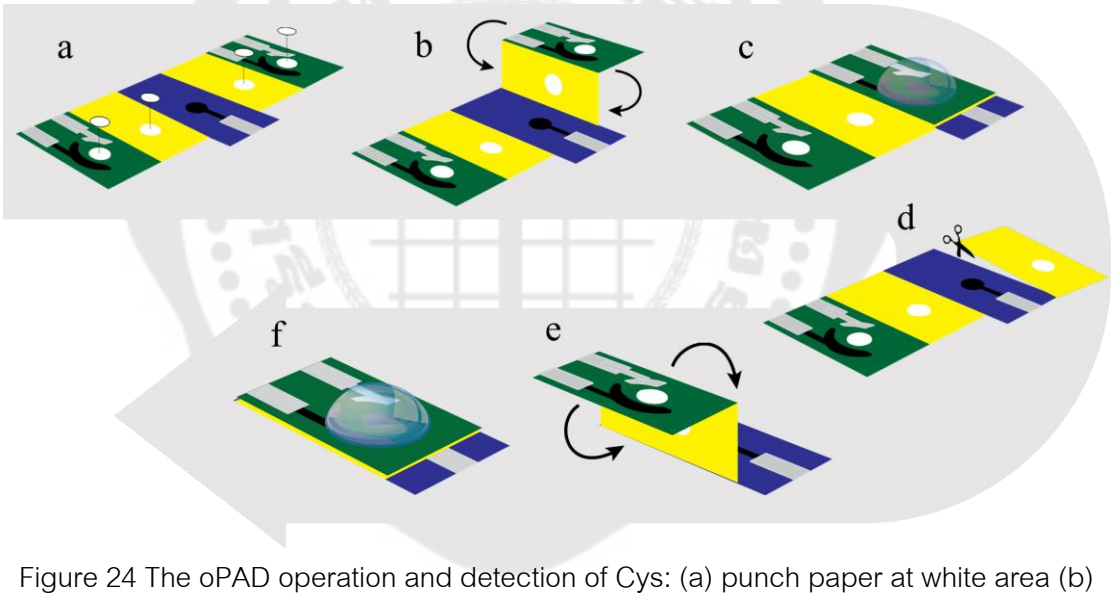

Figure 24 The oPAD operation and detection of Cys: (a) punch paper at white area (b) fold paper at modification side onto the top of working pad, (c) electropolymerization of poly(Cys), (d) tear the paper at modification side off, (e) fold paper at detection side on the top of working pad and (f) electrochemical measurement of Cys.

3.2.4 Sample preparation for analysis

To evaluate the power of a newly engineered oPAD for the detection of Cys in food products, the samples, including wheat flour, bread, and cake, were purchased from supermarkets in Bangkok, Thailand. For bread and cake, they were cut into small

pieces and 5.0 g of sample was weighed and dissolved with 50 mL of PBS pH = 8.0. Different concentrations of standard solutions of Cys were spiked into the samples and samples were diluted in the supporting electrolytes. The sample solutions were sonicated for 10 min. Finally, sample solutions were centrifuged at 6000 rpm for 20 min. All experiments were measured in triplicate.

3.3 Electrochemical capillary-flow immunoassay for detecting anti-SARS-CoV-2 nucleocapsid protein antibodies at the point of care

The contents of this section are based on the original research article (Samper et al., 2021), see in appendix 3 for the full article.

3.3.1 Reagent preparation

N-protein. Recombinant SARS-CoV-2 nucleocapsid protein (N-protein) was produced as described elsewhere (Fagre et al., 2021; Terry et al., 2021). Briefly, a bacteria-codon optimized gBlock was cloned into a pET28a bacterial expression with a C-terminal 6xHis tag. Recombinant protein was expressed in BL21(DE3) pLysS *E. coli* and purified by nickel affinity and size exclusion chromatography. To minimize aggregation, 50 mM HEPES buffer (pH 7.4), 500 mM NaCl was used throughout the purification process. N protein purity was assessed using SDS-PAGE gel electrophoresis. A solution of 0.5 mg/mL recombinant N protein was prepared in 45 mM trehalose and 4.5% glycerol, and striped onto a 3x16 mm nitrocellulose membrane (NCM, FF120, GE) using a reagent dispenser (Claremont Bio), so that 120 ng N protein was dispensed on each strip. N protein striped nitrocellulose membranes were stored at 4°C for up to a month before use, as stability over storage was illustrated elsewhere (Carrell et al., 2020).

HRP-antibody. Anti-mouse-IgG conjugated to horseradish peroxidase (HRP-antibody; ab97040, Abcam) was used as detection antibody. A solution of 5 µg/mL HRP-antibody was prepared in 0.01 M FeSO4-EDTA, 4% trehalose, and 0.1% BSA to enable storage of the dried antibodies for at least 5 months (Ramachandran, Fu, Lutz, & Yager, 2014). HRP-antibody reagent pads were made by pipetting 10 µL of this solution onto 3x5 mm glass fiber pads (Millipore Sigma, GXDX203000) and were then dried at 37°C for 30 min. They were stored at 4°C for up to a week before use.

Anti-N antibody. Antibody against SARS-CoV-2 N protein (GTX632269, GeneTex Inc.) was spiked in 0.1 M phosphate buffer saline pH 7.4 (PBS-based sample) or in blood sample. Whole human blood from healthy individuals was obtained from Lee Biosolutions.

Other reagents. The electrochemical substrate used throughout this study was 3,3′,5,5′-Tetramethylbenzidine (TMB), purchased from Sigma-Aldrich (T0440). The washing buffer solution consisted of 0.1 M phosphate buffer saline (pH 7.4) and 0.1% Tween80. All solutions were prepared using ultrapure water purified using Milli-Q system (Millipore Sigma).

3.3.2 Electrode fabrication

Electrodes were fabricated using a stencil-printing method described previously (Kava & Henry, 2021). Graphite powder (3569, Asbury Carbons) was hand mixed with carbon ink (E3178, Ercon Inc.) in the ratio 0.6 to 1 (%w/w) to create a graphite paste. Single-use stencils were made of 100-µm thick polyester films (PP2500, 3M), which were cut using a CO_2 laser cutter (Zing 1000, Epilog) following a pattern designed with CorelDRAW. A stencil was taped onto a whole polyester film (PP2500, 3M) and a squeegee was used to print the graphite paste onto the film. Upon removal of the stencil, the stencil-printed carbon electrodes (SPCE) were cured at 60°C for 30 min. SPCEs were then plasma treated at 500 mTorr, 125 W for 2 min to improve electrochemical performance (Kava & Henry, 2021). Finally, Ag/AgCl ink (901773, Sigma-Aldrich) was hand-painted on the reference electrode (RE) and cured at 60°C for 30 min. Plasma-treated electrodes, as fabricated here, have been shown to be stable for at least 10 days (Kava & Henry, 2021) and were used for up to a week following plasma treatment.

3.3.3 Capillary-flow device fabrication

The capillary-flow device was constructed by stacking 4 layers of 100-µm thick hydrophilic polyester film (PP2500, 3M) intercalated with 3 layers of 50-µm thick double-sided adhesive (467MP, 3M), similarly to previously described (Carrell et al., 2020). On each of these 7 layers, elements of the microfluidic circuit (channels, inlets, outlets and vent holes) were designed using CorelDRAW and cut with a CO_2 laser cutter,

to create the 3D microfluidic network shown in Figure 41a. An HRP-antibody reagent pad was placed in the device channel before adding the top layer of polyester film. over the sample inlet, to retain blood cells and deliver plasma to the microfluidic channel. Subsequently, a NCM striped with N protein was inserted at the outlet of the microfluidic channel, and a waste pad (Grade 1 CHR, Whatman plc) was placed over the end of the NCM to create a passive pump for the fluidic system. Finally, a SPCE was placed on top of the NCM, upside-down, so that the working electrode (WE) was in contact with the N protein strip. The SPCE was held in position on the NCM by the layer 4 adhesive (L4, Figure 41a(i)).

3.3.4 Device operation and electrochemical recording

The assay was initiated by adding a 10-μL blood sample onto the blood-filtration membrane. Then, 85 μL of washing buffer were added to the buffer inlet. Once the buffer had started to flow through the NCM, a 0.0 V potential was applied to the WE (vs the Ag/AgCl RE) using a portable potentiostat (PalmSens4) and chronoamperometry recording started. Following the sequential and automated delivery of sample, washing buffer, HRP-antibody and washing buffer to the NCM, 1 μL of TMB was added to the substrate inlet on the NCM, as indicated in Figure 41a(ii). In the presence of HRP in the detection zone, TMB gets oxidized into an electrochemically active product (oxTMB), which is then reduced at the electrode surface, generating an increase in the cathodic current. The electrochemical immunoassay detection mechanism is illustrated in Figure 41b.

CHAPTER 4
RESULTS AND DISCUSSION

In this chapter, the results and discussion of development of miniaturized electrochemical devices for detection of important analytes were presented. It can be divided into three projects following their proposed methods in the chapter 3.

4.1 A multilayer microfluidic paper coupled with an electrochemical platform developed for sample separation and detection of dopamine

The contents of this section are based on the original research article, see in appendix 1 for the full article.

4.1.1 Characterization of the modified electrode

The PGA film modified SPGE was prepared by electropolymerization of 20 mM glutamic acid in 0.1 M PBS (pH 7.4) using CV. The potential was varied from -0.5 to +1.6 V versus Ag/AgCl at a scan rate of 100 mV/s for 7 cycles. Cyclic voltammogram obtained during electropolymerization is shown in Figure 25a. From the figure, a well-defined peak current around +1.49 V can be observed during the first 3 cycles. After the fourth cycle, the broad peak current gradually increased with the increase in the number of scans. This indicated the growth and subsequent formation of the polymer film was on the surface of SPGE (X. Liu, Luo, Ding, & Ye, 2011).

The electrochemical behaviors of the unmodified SPGE and PGA/SPGE were compared and investigated using the techniques of CV and ESI. First, cyclic voltammograms of 5 mM $[Fe(CN)_6]^{3-/4-}$ in 0.1 M PBS (pH 7.4) were recorded using different electrodes in the potential range from -0.8 to +1.0 V. The redox peaks of $[Fe(CN)_6]^{3-/4-}$ are shown in Figure 25b. It was observed that the electrochemical signal of 5 mM $[Fe(CN)_6]^{3-/4-}$ obtained using PGA/SPGE increased by approximately two-fold when compared with that obtained from the unmodified SPGE. This implies that PGA/SPGE can be a candidate for detection of low concentrations of DA.

To explain the previously obtained results, the Randles–Sevcik Equation (2) was used to calculate the electroactive surface areas of the PGA/SPGE and unmodified SPGE. In the equation, i_p denotes the peak current; n, the number of electrons; F,

Faraday's constant; A, the electroactive surface area; C_0^*, the concentration of analyte ($[Fe(CN)_6]^{3-/4-}$); v, the scan rate; D_0, the diffusion coefficient of $[Fe(CN)_6]^{3-/4-}$; R, the ideal gas constant; and T, the temperature. Based on the known parameters from a previous study (n = 1, $C_0^* = 5 \times 10^{-6}$ mol/cm^3, v = 100 mV/s, $D_0 = 7.6 \times 10^{-6}$, R = 8.13447 J/K•mol and T = 298 K) (Punjiya et al., 2018), the electroactive surface areas were calculated. A comparison of the electroactive surface areas is shown in Figure 25c. PGA/SPGE provided a higher electroactive surface area than the unmodified SPGE. In addition, the value of peak separation (ΔEp) decreased from +0.950 V, obtained for the unmodified SPGE, to +0.361 V, obtained for the PGA/SPGE, indicating that the rate of electron transfer can be increased after the electropolymerization of PGA on the surface of SPGE (X. Liu et al., 2011).

$$i_p = 0.45nFAC_0^* \sqrt{\frac{nFvD_0}{RT}} \quad \text{.....equation 2}$$

Next, EIS was used to confirm the successful modification of the proposed electrode by investigating the electron transfer resistance (R_{ct}) for the redox couple of $[Fe(CN)_6]^{3-/4-}$ at the electrode surface. EIS was selected as the characterization technique, owing to its simplicity, surface sensitivity, and fast response. The results of EIS are presented using Nyquist plots. The Nyquist plots of both the unmodified SPGE and the PGA/SPGE were obtained using 5 mM $[Fe(CN)_6]^{3-/4-}$ in 0.1 M PBS (pH 7.4) (Figure 25d). Each point of the Nyquist plot refers to the impedance corresponding to a specific frequency, as it is scanned from high to low frequency. The diameter of the semicircle is equal to the charge transfer resistance (R_{ct}) at the interface of the electrode and solution (Ozcan, Ilkbas, & Atilir Ozcan, 2017). The values of R_{ct} of $[Fe(CN)_6]^{3-/4-}$ at the unmodified SPGE and the PGA/SPGE were calculated to be 6.8 and 2.3 kΩ, respectively. The value of R_{ct} significantly decreased after electropolymerization of PGA on the surface of SPGE. These results confirmed that the surface of SPGE was successfully modified with PGA.

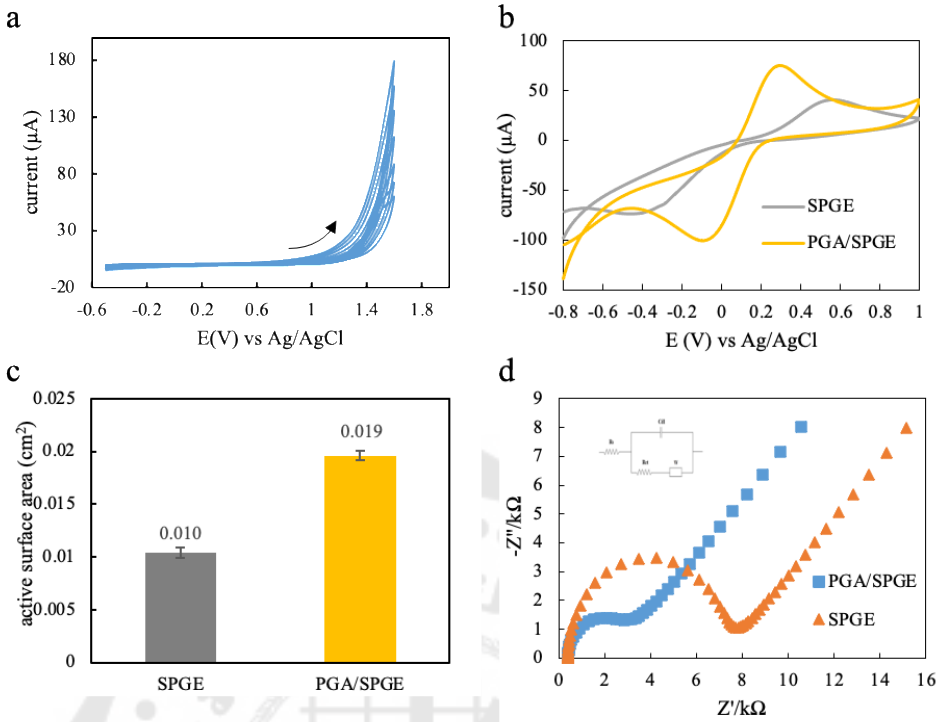

Figure 25 (a) The electropolymerization of 20 mM glutamic acid onto SPGE surface was performed using CV scanned between -0.5 V and +1.6 V, scan rate of 100 mV/s for 7 cycles. (b) Cyclic voltammograms of 5 mM $[Fe(CN)_6]^{3-/4-}$ in 0.1 M PBS pH 7.4 at SPGE (gray line) and PGA/SPGE (yellow line), scan rate 100 mV/s. (c) Electroactive surface areas of SPGE (grey bar) and PGA/SPGE

4.1.2 Electrochemical behavior of DA at PGA/SPGE

The electrochemical property of DA was investigated by CV and DPV, using the unmodified SPGE and PGA/SPGE. CV was performed to study the electrochemical behavior of DA with different materials of the working electrode. Figure 26a presents the comparison of cyclic voltammograms of DA using the unmodified SPGE (blue line) and PGA/SPGE (orange line). At the unmodified SPGE, the anodic and cathodic peaks were recorded at +0.3 and -0.15 V, respectively. Interestingly, PGA/SPGE provided a higher current of the anodic and cathodic peaks and shifted to a negative direction, recorded at +0.089 and -0.083 V, respectively. Moreover, DPV was employed to validate the better performance of the PGA/SPGE compared with the unmodified SPGE, as shown in Figure 26b. At the unmodified SPGE (blue line), the broad oxidation peak of DA was

observed at +0.01 V, and the oxidation current obtained was 6.096 μA. In contrast, the PGA/SPGE (orange line) provided a well-defined peak and shifted to a negative direction, with the peak potential at -0.07 V. In addition, there was a significant enhancement (two-fold) of the peak current for DA compared with the unmodified SPGE. Therefore, the results obtained using CV and DPV strongly suggest that the PGA/SPGE exhibited electrocatalytic activity toward the direct oxidation of DA. These results indicated that PGA/SPGE is an excellent electrode for detection of DA.

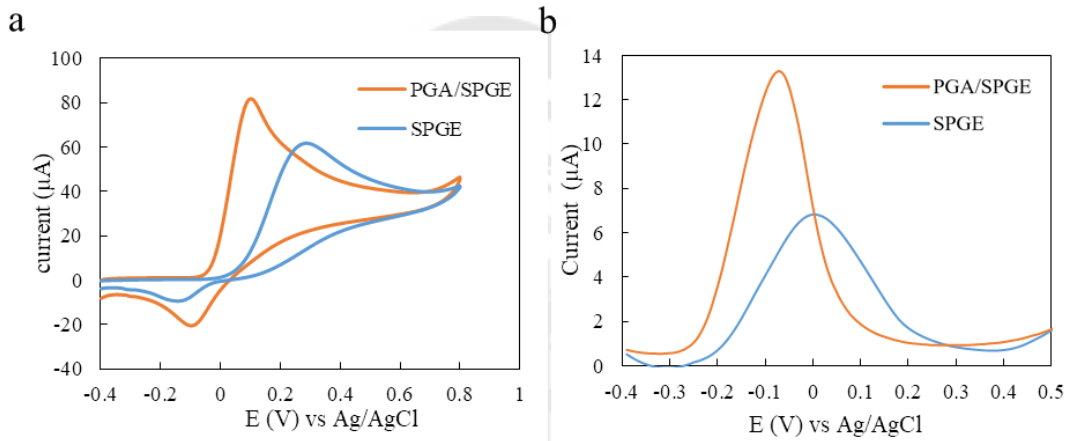

Figure 26 Cyclic voltammograms (a) and differential pulse voltammograms (b) of DA at SPGE (blue line) and PGA/SPGE (orange line) in PBS pH 7.4

To achieve the best electrochemical response for detection of DA, the critical parameters for the electropolymerization of PGA include the concentration of monomer glutamic acid and the number of scans used in CV. These two parameters are involved in controlling the thickness of the polymer on the electrode surface. First, the concentrations of glutamic acid were investigated in the range of 10–50 mM (Figure 27a). At 20 mM, glutamic acid provided the highest oxidation current of DA. Beyond 20 mM, the oxidation current of DA gradually decreased, which may influence the thickness of the film of PGA on the SPGE surface, which is too thick, leading to low electron transfer at the interface between the electrode and electrolyte. Therefore, 20 mM of glutamic acid was an optimal condition. Second, the number of scans in CV was varied in the range of 3–15 cycles (Figure 27b). As can be seen from the figure, the oxidation currents of DA gradually increased as the number of scans increased from 5 to 7

cycles. The oxidation currents were relatively stable after 7 cycles. Thus, the number of scans was fixed to 7 cycles.

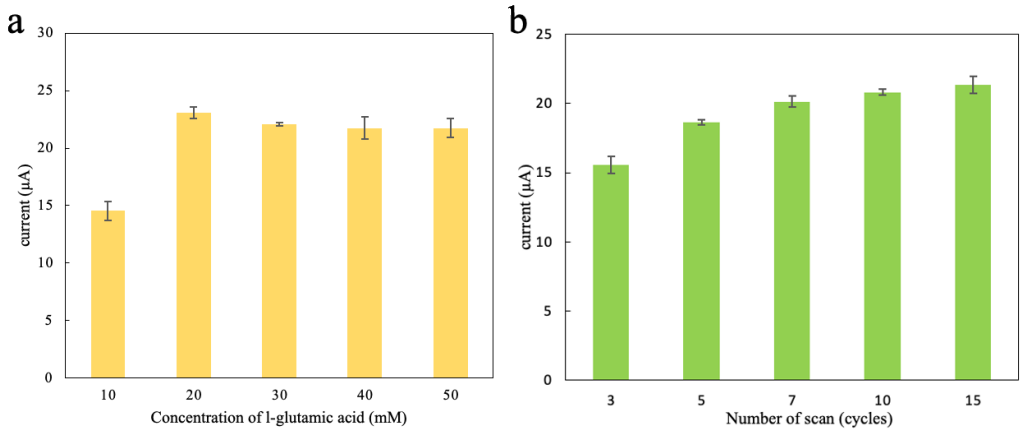

Figure 27 The oxidation currents of 100 μM DA in PBS pH 7.4 measured by DPV using PGA/SPGE have different (a) concentrations of l-glutamic acid, and (b) scan numbers.

4.1.3 Comparison of the design and configuration of devices

To confirm the capability of the eμPAD for successive sample separation and detection using only a single drop of the sample solution, stagnant electrochemical analysis (Figure 28) was conducted by dropping 100 μL of the mixture of DA and AA on the PGA/SPGE. In addition, the electrochemical measurement was performed by DPV. Figure 29a shows the individual differential pulse voltammograms of 100 μM DA and 100 μM AA in PBS (pH 7.4). The oxidation peaks of the two substances approximately appear at the same potential. Hence, distinguished peaks for DA and AA are extremely difficult to observe. Therefore, AA is considered to be a major electrochemical interference for the detection of DA at the PGA/SPGE using stagnant electrochemical analysis.

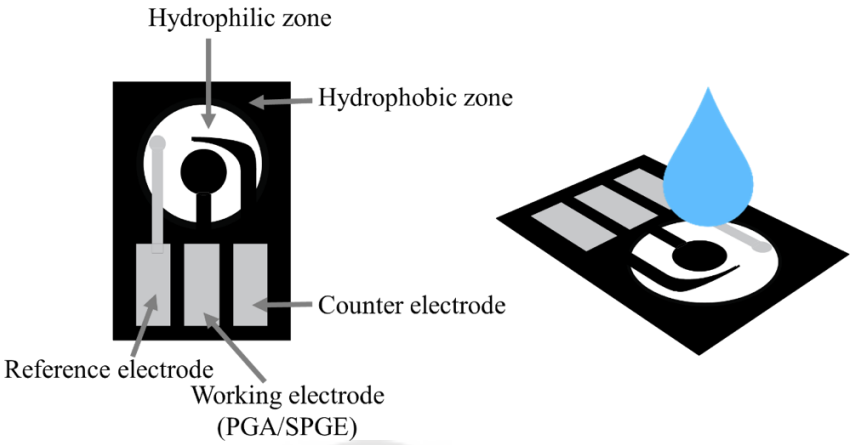

Figure 28 The illustration of paper-based screen-printed electrodes for electrochemical stagnant analysis

Based on the results confirmed from the stagnant electrochemical analysis, to overcome this problem, Nafion coated onto the eμPAD was suggested for the detection of DA in the presence of AA. As we know, Nafion has been widely used in biosensor applications (Babaei & Taheri, 2013; Parrilla, Canovas, & Andrade, 2017) owing to its structure that shows a highly permeable membrane, which allows only cations to pass through the membrane while strongly repelling anions away from the electrode surface. Based on this property, Nafion was used in this work for coating the eμPAD channel to block AA (anion), while allowing the DA in the solution to flow to the electrochemical detection zone and thereby be measured by the electrochemical technique. The influence of different concentrations of Nafion to block AA was first investigated. Figure 29b shows the oxidation current of 100 μM DA (orange bar) and 100 μM DA in the presence of 100 μM AA (blue bar) obtained with different concentrations of Nafion coated on the eμPAD channel. As can be seen from the figure, the difference in oxidation current of 100 μM DA and 100 μM DA in the presence of 100 μM AA considerably decreased with increase in the Nafion concentration. Up to 0.5% Nafion, the values of oxidation current for both are approximately equal. These results indicated that 0.5% Nafion can completely block 100 μM AA, while measuring the concentration of DA. Moreover, to the best of our knowledge, the maximum

concentration of AA in real samples is 80 μM (Rattanarat, Dungchai, Siangproh, Chailapakul, & Henry, 2012). Hence, 0.5% (v/v) Nafion was selected as an optimal condition for coating the eμPAD channel.

The pH effect was determined based on using Nafion as material for AA eliminating strategy. Due to Nafion is proven to block anionic molecule but allows only cationic molecule transport through Nafion structure. Therefore, the pH working condition was fixed in the range where DA exhibits positive charge, while AA shows negative charge. To obtain this expected behavior, their pK_a value were considered. The pK_a value of DA at amine group is 8.89 and pKa value of AA at hydroxyl group is 4.10 (Cheng, Zhang, Wang, Huang, & Ma, 2017). Thus, at pH = 7.4 is most suitable condition for showing cationic DA and anionic AA as well as for applying this device to determine DA in biological samples.

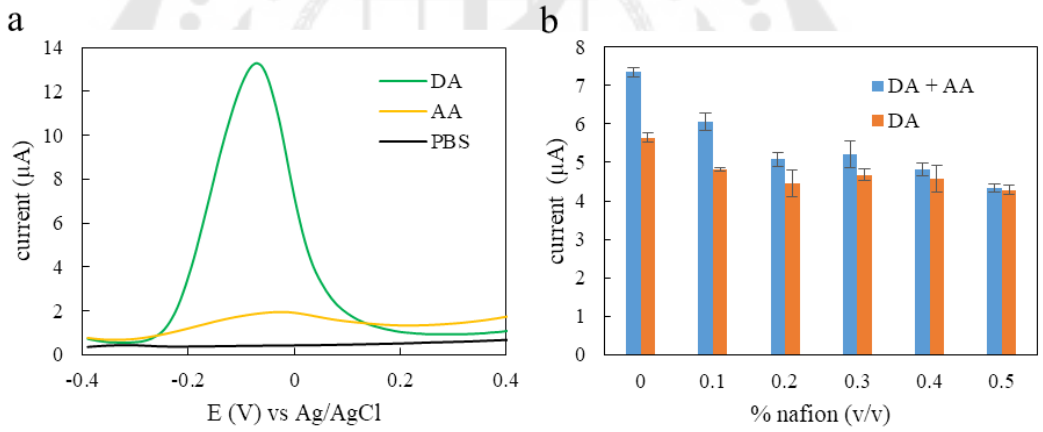

Figure 29 (a) Differential pulse voltammogram of a single 100 μM DA (green line), 100 μM AA (orange line), and PBS pH 7.4 (black line) at PGA/SPGE performed by stagnant analysis. (b) the oxidation current value of 100 μM DA (blue bar) and 100 μM DA in the presence of 100 μM AA (orange bar) obtained from different concentrations of Nafion coated into the eμPAD channel.

4.1.4 Improvement of the electrochemical response for the detection of DA using the eμPAD

Based on the results obtained from the eμPAD, the value of oxidation current for the detection of DA was very low due to two primary factors. The first factor is

the Nafion coated onto the sample zone and microfluidic channel. Owing to the structure of Nafion, which contains perfluoroalkyl backbones, it has strong hydrophobic properties (Yin et al., 2010). Hence, after coating Nafion onto the eμPAD, Nafion can penetrate into the pores of the paper, obstructing the flow of the solution in the microfluidic channel resulting in a slow flow rate and leading to low mass transport of DA from the bulk solution to the electrode interface. Moreover, due to the slow flow rate, the measurement requires a significant amount of time. The second factor is the flow rate on the eμPAD after the solution completely migrates to the dry region of the hydrophilic area, which leads to a decay in the flow rate; thereafter, the flow rate decreases with time. This phenomenon also causes a low mass transport at the electrode interface (J. A. Adkins et al., 2016). As previously mentioned, a multilayered eμPAD was designed and employed to overcome these disadvantages. In a previous work, a sealing method with the use of a packing tape was proposed. Sealing the top part of the μPAD using a packing tape can increase the flow rate by over two-fold, which is contrary to the open μPAD (Channon et al., 2018). From this idea a packing tape was used as a sealing material to increase the flow rate of the eμPAD. As shown in Figure 30a, we have designed and fabricated four different platforms. The first platform is the open eμPAD that is used for comparison. It can be observed that the use of the second platform (Figure 30b), which was sealed on the top using a packing tape, slightly increased the oxidation current corresponding to 100 μM DA, when compared with the open eμPAD (first platform). However, the obtained response is not highly sensitive enough for detection of DA in biological samples. Therefore, in literature, we found that the use of an absorbent pad can overcome the decay in flow rate with time, because the absorbent pad is used to absorb the solution from the sample zone through a porous structure and continuously enable capillary flow (quasi-steady flow with time) on the eμPAD (Medina-Sanchez, Cadevall, Ros, & Merkoci, 2015). Therefore, in this work, we used a round cotton pad instead of the absorbent pad. This is because the round cotton pad exhibits high porosity similar to the absorbent pad but has a lower cost. It is placed on top of the detection zone (third platform) to enable a quasi-steady flow. However, the

oxidation current obtained from the third platform was also slightly increased when compared with the open eμPAD (first platform), and no difference was observed from the second platform. Therefore, it is impossible to detect DA in a real sample with this platform as well. We have attempted to use the round cotton pad and the packing tape to create a novel device called a multilayered eμPAD. Our design was first fabricated as shown in the fourth platform. From the figure, it can be clearly seen that the multilayered eμPAD (fourth platform) provided the highest electrochemical response and high sensitivity for the detection of DA. We strongly believe that the excellent results obtained from the use of the packing tape and round cotton pad enabled a high flow rate and generated more completely mass transport of DA to electrode interface.

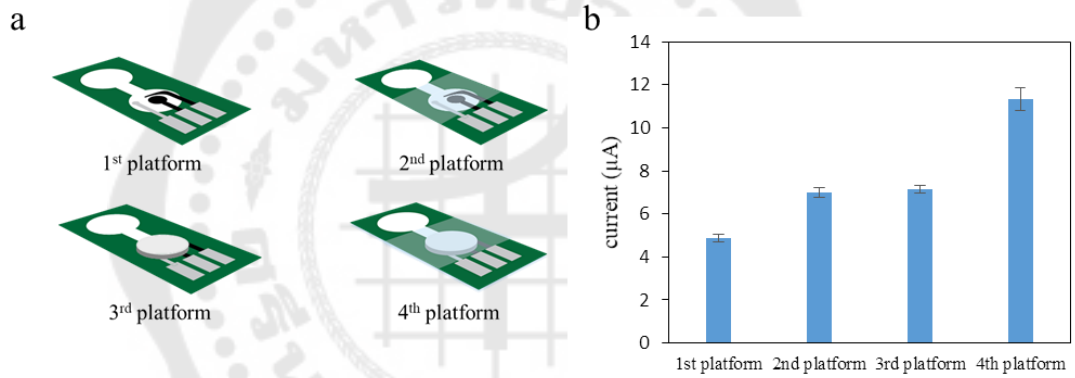

Figure 30 (a) The schematic representation for design and fabrication of eμPAD in different platforms. (b) The effect of different eμPAD platforms on the oxidation current for DA detection.

After achieving the optimal design, we evaluated the effect of the waiting time before performing the electrochemical measurement, as it also had a significant effect on the electrochemical response of the effect of different waiting time of 10, 15, and 20 min was investigated using the multilayered eμPAD. The oxidation current obtained from the different waiting times is shown in Figure 31. By increasing the waiting time, the oxidation current considerably increased as expected. However, we observed that the oxidation currents obtained between 15 and 20 min did not significantly differ. Accordingly, waiting time of 15 min was selected as the optimal waiting time for subsequent measurements.

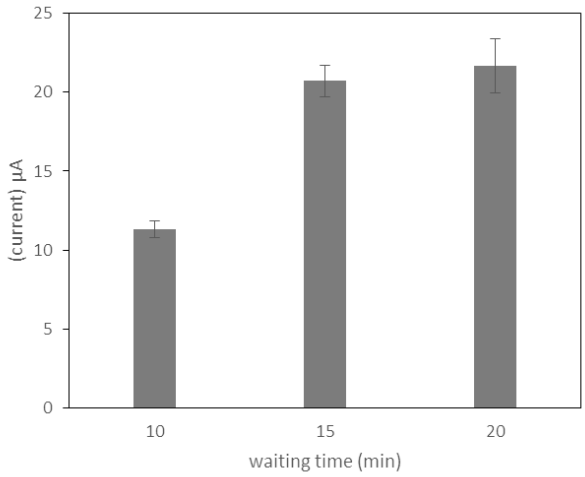

Figure 31 The oxidation currents of 100 µM DA in PBS pH 7.4 measured by DPV using a multilayer eµPAD at different waiting times

4.1.5 Analytical performance

The analytical performance of the multilayered eµPAD for detection of DA was evaluated, and several concentrations of DA were determined using DPV. Figure 32a shows the differential pulse voltammogram at various concentrations of DA using the multilayered eµPAD. The oxidation peak currents of DA gradually increased with increasing concentrations. The linear calibration plot between the oxidation current and concentration of DA was obtained over the range of 1–200 µM. A linear regression equation of $i_{pa} = 0.1987C_{DA} + 1.1301$ with correlation coefficients of $R^2 = 0.9994$ (Figure 32b) was obtained. The LOD (LOD = $3SD_{blank}$/slope) was found to be 0.41 µM. Moreover, the analytical performance of the proposed multilayered eµPAD was compared with that in the previous reports, and the results are summarized in Table 2. Although the LOD in some previous reports was lower than the proposed platform; nonetheless, those methods required several steps for modification of the electrodes and used expensive materials. However, the proposed platform only involved a single step for dropping sample solution onto the sample zone and allows the sample separation before analysis. Thereafter, the sample was allowed to successively penetrate to the sample separation and detection zones using a single device. This innovative device can be widely used in a variety of applications owing to its advantages, such as simplicity, fast response, and

the ability to perform sample separation. Another important point is that coating Nafion on the channel is more convenient and takes less time than the direct modification onto the electrode surface. Thus, the design presented here can be easily fabricated and extended to a range of complex assays with favorable preferences of a cost-effective and effortless platform, thereby facilitating its generic use.

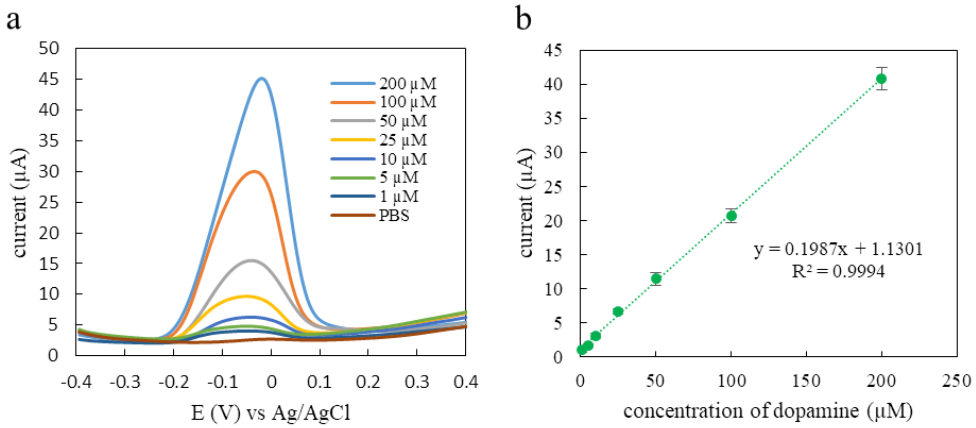

Figure 32 (a) Differential pulse voltamograms obtained from several concentrations of DA in PBS pH 7.4 using multilayer eμPAD, (b) calibration plot between concentration of DA (μM) and current (μA)

Table 2 Analytical performance of previous reports compared with the proposed multilayer eμPAD based on electrochemical detection of DA

Electrode	Technique	LOD (μM)	Linear range (μM)	Ref.
Poly(SDB)/CPE	DPV	0.8	5.0–10, 20–80 and 90–1000	(Reddaiah, Reddy, Raghu, & Reddy, 2013)
AgNPs/rGO/GCE	LSV	5.4	10–800	(Kaur, Pandiyan, Satpati, & Srivastava, 2013)

Table 2 (Continued)

Electrode	Technique	LOD (μM)	Linear range (μM)	Ref.
PImox-GO/GCE	DPV	0.63	12–278	(X. Liu et al., 2014)
HNP-PtTi/ GCE	DPV	3.2	4.0–500	(Zhao, Yu, Tian, & Xu, 2016)
G-DHE	DPV	0.2	5.0– 2000	(Yuan et al., 2018)
PtNi@MoS_2/GCE	DPV	0.1	0.5–150	(Ma, Zhang, Wu, Zhang, & Zeng, 2019)
multilayer eμPAD (PGA/SPGE)	DPV	0.41	1.0–200	This work

Abbreviaion

Poly(SDB)- poly(solochrome dark blue), CPE- carbon paste electrode, AgNPs- silver nanoparticles, rGO- reduced graphene oxide, LSV- linear sweep voltammetry, PImox- overoxidized polyimidazole, GO- graphene oxide, HNP- hierarchical nanoporous, G-DHE- graphene–diamond hybrid electrode and PtNi@MoS_2- PtNi bimetallic naoparticles loaded MoS_2 nanosheets.

4.1.6 Selectivity

Apart from the interference from AA, other common interferences that were observed in urine samples include uric acid, glucose, vitamin B, BSA, Na^+, and Ca^{2+}. As shown in Figure 33, the oxidation current of 100 μM DA in the presence of 100 μM uric acid, 1 mM glucose, 100 μM vitamins B_2 and B_6, 1000 μg/L BSA, 1 mM Na^+, and 1 mM Ca^{2+} do not interfere (change in signal was below 5%). These results indicated that the proposed multilayered eμPAD offers excellent selectivity for the detection of DA.

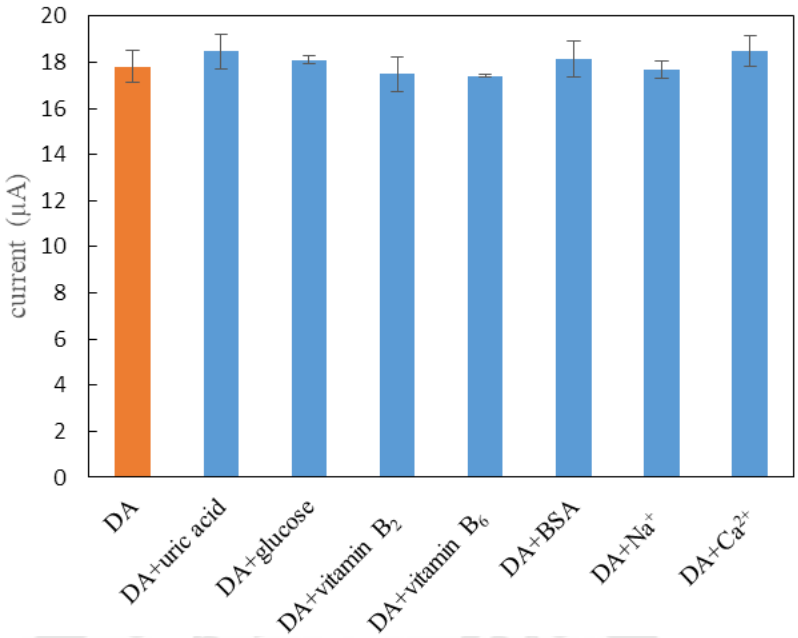

Figure 33 The interferences effect of 100 μM Uric acid, 1 mM glucose, 100 μM vitamin (B_2 and B_6), 1000 μg/L BSA, 1 mM Na^+ and 1 mM Ca^{2+} on the detection of 100 μM DA in PBS pH 7.4

4.1.7 Analytical application

The practicality of the proposed device was demonstrated by the detection of DA in artificial urine samples. Recovery test was conducted by increasing the specified concentrations (10, 20, 40, 60, and 80 μM) of DA using the standard addition method. As shown in Table 3, percentage recovery and relative standard deviation with three different devices were observed in the range of 96.6%–108.3% and 1.4%–5.0%, respectively. Finally, the results obtained with the proposed device were compared with those obtained using UV–Vis spectroscopy (Guo et al., 2009). Paired *t*-test at 95% confidence interval was evaluated; the calculated paired two-tailed value (0.13) of DA was below the critical *t* value (2.78). These results indicated that the proposed device is acceptable and reliable for the detection of DA in urine samples.

Table 3 The analytical application using a novel multilayer eμPAD for the detection of DA in artificial urine sample (n=3).

Sample	Spiked (μM)	Found (μM)	Recovery (%)	RSD (%)
Artificial urine	10	10.8±0.3	108.3	2.3
	20	20.2±0.7	101.0	3.6
	40	38.6±1.9	96.6	5.0
	60	59.2±1.7	98.7	2.8
	80	81.1±1.1	101.4	1.4

4.2 A novel L-cysteine sensor using in-situ electropolymerization of L-cysteine: potential to simple and selective detection

The contents of this section are based on the original research article, see in appendix 2 for the full article.

4.2.1 Characterization of a modified electrode

The poly(Cys) was synthesized on the SPGE surface via electropolymerization using 3 mM L-cysteine solution in PBS at pH 8.0 by cyclic voltammetry which scanned from -0.5 V to +2.0 V vs. Ag/AgCl for 9 cycles at a scan rate of 100 mV/s. The mechanism of poly(Cys) growth at the electrode surface can be explained by the SH functional group of Cys was oxidized during CV scan for oxidative direction, which appeared anodic peak at 0.60 V (Figure 34a). Then, two radicals of Cys were forming disulfide bound at electrode surface, after finishing cycle scanning and poly(Cys) was obtained (Martínez-Huitle, Cerro-Lopez, & Quiroz, 2009; Y. Wang et al., 2016). Furthermore, as seen in the inset of Figure 34a, the define peak currents decrease after the number of scans has risen also corresponding to passivation of polymer film at electrode surface.

Figure 34b shows representative cyclic voltammograms of 5 mM $[Fe(CN)_6]^{3-/4-}$ in 0.1 M PBS (pH = 8.0) for bare and poly(Cys) modified SPGE. The redox currents obtained from poly(Cys)/SPGE were higher than bare SPGE. In terms of peak

potential, the ΔE for poly(Cys)/SPGE decreased from +0.81 V to +0.54 V compared to bare SPGE. The Randles–Sevcik equation 3 was used to calculate the electroactive surface area (Charoenkitamorn et al., 2018) before and after electropolymerization using $[Fe(CN)_6]^{3-/4-}$ as the redox probe.

$$I_p=\left(2.69\times10^5\right)n^{3/2}AD_0^{1/2}\nu^{1/2}C_0^*\text{.....equation 3}$$

Where, n is number of electron of redox probe (n = 1), A is electroactive surface area (cm^2), D_0 is diffusion coefficient of $[Fe(CN)_6]^{3-/4-}$ = 7.6 × 10^{-6} cm^2/s, C_0^* is the concentration of $[Fe(CN)_6]^{3-/4-}$ and $I_p/\nu^{1/2}$ was obtained from the slope of relationship plot between the square root of scan rate and electrochemical current. The comparison of calculated electroactive surface areas is shown in Figure 34c. The areas were as followed: 0.037 cm^2 for bare SPGE, 0.040 cm^2 for poly(Cys) at 3 cycles, 0.046 cm^2 for poly(Cys) at 6 cycles, and 0.054 cm^2 for poly(Cys) at 9 cycles for scanning. From the results, it can be observed that poly(Cys) modified SPGE at 9 cycles of scan provides the highest electroactive surface area, which exhibits an excellent material for detection of Cys. Next, the surface coverages of bare and modified electrodes were calculated using equation 4 (Kumar et al., 2017).

$$\Gamma=\frac{Q}{nFA}\text{ .....equation 4}$$

Where Γ is surface coverage, Q is charge obtained from area under the oxidation peak of supporting electrolyte (Figure 34d), n is number of involved electron, F is Faraday's constant = 96,485 C/mol and A is electroactive surface area. The surface coverages were compared as followed: 9.9 × 10^{-8} mol/cm^2 for bare electrode and 3.8 × 10^{-7} mol/cm^2 for poly(Cys)-modified SPGE. The enriched electroactive surface area and surface coverage indicated the presence of polymer film onto electrode surface.

Figure 34e shows the EIS spectra for a bare SPGE compared with poly(Cys)-modified SPGE using different electropolymerization conditions to confirm polymer film growth on the electrode. The electron transfer resistance (R_{ct}) between the redox species of 5 mM $[Fe(CN)_6]^{3-/4-}$ in 0.1 M PBS (pH = 8.0) and electrode interface was measured (Zhang, Yu, Shen, Qi, & Wang, 2020). The R_{ct} for bare SPGE and

poly(Cys)/SPGE at 3, 6, and 9 scanned cycles was 52, 41, 28, and 8.0 kΩ, respectively. The decreasing R_{ct} values as a function of increasing electropolymerization scan number demonstrate successful electrode surface modification. The results also agree with the increasing electrode area and surface coverage results.

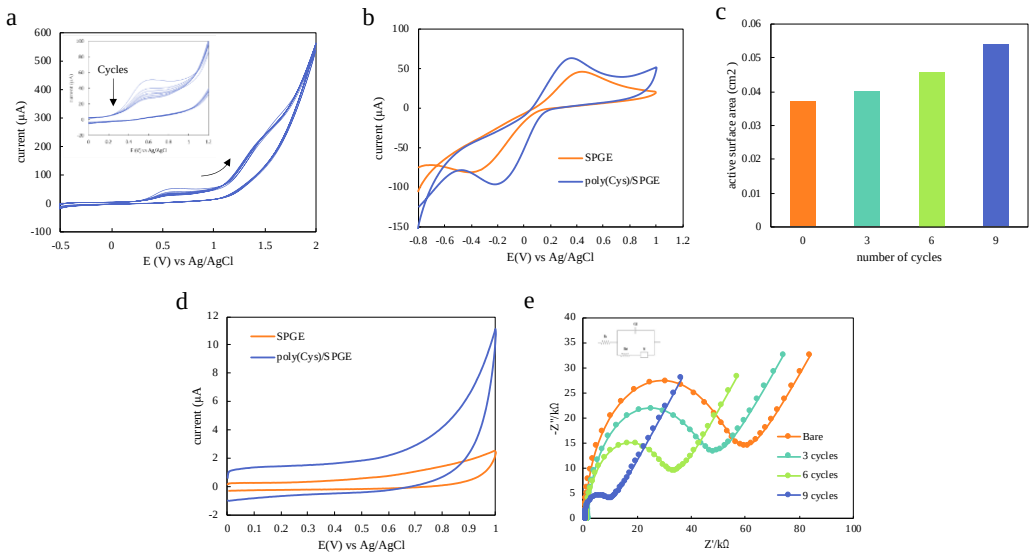

Figure 34 (a) CV diagram during the electropolymerization of poly(Cys) at SPGE. (b) CV performance of 5 mM $[Fe(CN)_6]^{3-/4-}$ in 0.1 M PBS (pH=8.0) at bare SPGE and poly(Cys)/SPGE at 9 scanned cycles. (c) Calculated electroactive surfaces at bare SPGE, poly(Cys)/SPGE at 3, 6 and 9 scanned cycles. (d) CV curves of supporting electrolyte (0.1 M PBS at pH 8.0). (e) EIS curves of bare SPGE, poly(Cys)/SPGE at 3, 6 and 9 scanned cycles.

Besides electrochemical characterization, the surface morphology was characterized by SEM. In Figure 35a, the SEM image clearly displayed roughness and crumble of graphene sheets over the surface of bare SPGE. Meanwhile, upon the electropolymerization turned into smoother surface (Figure 35b), this implied the formation of polymeric thin film of poly(Cys) covered up SPGE surface (Krishnan & Saraswathyamma, 2021). This result indicated the successful electrode modification of poly(Cys)/SPGE

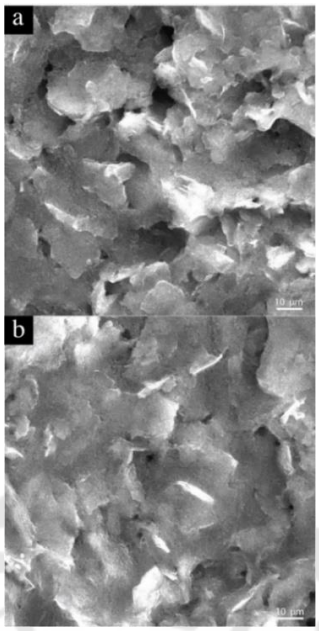

Figure 35 SEM images of (a) bare SPGE and (b) poly(Cys)/SPGE at 2000 magnification

4.2.2 Electrochemical behavior of Cys at poly(Cys)/SPGE

CV and DPV were used to compare the electrochemical responses of Cys detection using bare SPGE and poly(Cys)/SPGE. Figure 36a shows representative CVs of standard Cys at bare SPGE. The oxidation potential occurred at +0.50 V. However, the oxidation potential of Cys at poly(Cys)/SPGE was more negative at +0.41 V. For DPV, as shown in Figure 36b, the oxidation potential shifted negative from +0.36 V at bare SPGE to +0.18 V at poly(Cys)/SPGE (blue line). The obtained lower oxidation potential of Cys can confirm that poly(Cys) could act as an electrocatalyst for Cys detection. Furthermore, the oxidation current obtained for poly(Cys)/SPGE was twice as large as the current obtained at a bare SPGE. These results demonstrated that the electron transfer quickly occurred. The excellent electrochemical performance originates from high conductivity over poly(Cys)/SPGE, due to the presence of sulfhydryl group on polymeric chain structure (Sohouli, Ghalkhani, Rostami, Rahimi-Nasrabadi, & Ahmadi, 2020).

To investigate the mass transfer kinetics of Cys at the electrode interface, the oxidation current was measured as a function of scan rate in CV. As shown in Figure 36c, the peak current increases with increasing scan rates. Furthermore, the linear

relationship between the square root of scan rate and Cys oxidation current (inset Figure 36c), indicates diffusion-controlled mass transfer. Andrieux and Savèant's theoretical model (equation 5) was used to calculate a diffusion coefficient of Cys (D_0) by using information from the linear relationship of the square root of scan rates and electrooxidation currents of Cys (y = 168.37x - 5.4958) (Boni, Wong, Dutra, & Sotomayor, 2011).

$$I_p = 0.496FAC_sD_0^{1/2}\left(\frac{F}{RT}\right)^{1/2}\nu^{1/2}) \quad \text{.....equation 5}$$

Where F is Faraday's constant = 96,485 C/mol, R = 8.31447 J/mol·K, T = 298 K, A = 0.054 cm^3, and C_s is Cys concentration = 1×10^{-6} mol/cm^3, I_p is oxidative current of Cys and ν is scan rate. The diffusion coefficient (D_0) of Cys was 1.09×10^{-4} cm^2/s, this value is in agreement with that obtained in previous report (Geng, Li, Bo, & Guo, 2016). As results from CV curves in Figure 36c, peak potentials shifted to a positive direction when increasing the scan rate, indicating that Cys electrooxidation is an irreversible process. The equation 6 was used to calculate the number of electron transfers at the electrode interface (Nakthong, Kondo, Chailapakul, & Siangproh, 2020).

$$J_p = \left(2.99\times10^5\right)n\left[\left(1-\alpha\right)n_\alpha\right]^{1/2}AC_sD_0^{1/2}\nu^{1/2} \quad \text{.....equation 6}$$

The factor $\left(1-\alpha\right)n_\alpha$ was calculated from linear regression of log scan rates and oxidation peak potentials of Cys (E_{pa}) (y = 0.1638x + 0.8089), and the slope was obtained from this relationship, which can be calculated to $\left(1-\alpha\right)n_\alpha$ was found to be 0.18. After that, the number of electrons transfer can be estimated to be n = 1.85 or ~ 2.

The number of protons involved at the electrode surface also was investigated by observing the electrochemical behavior of Cys in the different pH conditions. Figure 36d shows CV curves of Cys at poly(Cys)/SPGE in pH range of 5.0–9.0; it is clearly seen that the oxidation peak potentials (E_{pa}) were shifted to a positive direction when pH values increased. Moreover, the linear relationship between pH values and oxidation peak potentials was plotted (y = -0.0648x + 1.0164), then the Nernst equation 7 was used to describe this relationship.

$$E_{pa} = E^0 + \left(\frac{0.0591}{n}\right) \log \left[\frac{(ox)a}{Rb}\right] - \left(0.0591 \frac{m}{n}\right) pH \text{.....equation 7}$$

Where m and n are the number of electrons and protons at the electrode interface, respectively (Thomas et al., 2014). The slope was calculated to be 0.0648, which is close to the theoretical value 0.0591. This result illustrates that the number of electron and proton transferred at the electrode interface are equal, which means m = n = 2. Thus, the mechanism of Cys oxidized at poly(Cys)/SPGE involves two electrons and two protons, which was in agreement with previous works (Rasheed, Pandey, Jabbar, Ponraj, & Mahmoud, 2019; Singh, Jaiswal, Tiwari, Foster, & Banks, 2018; Thota & Ganesh, 2016).

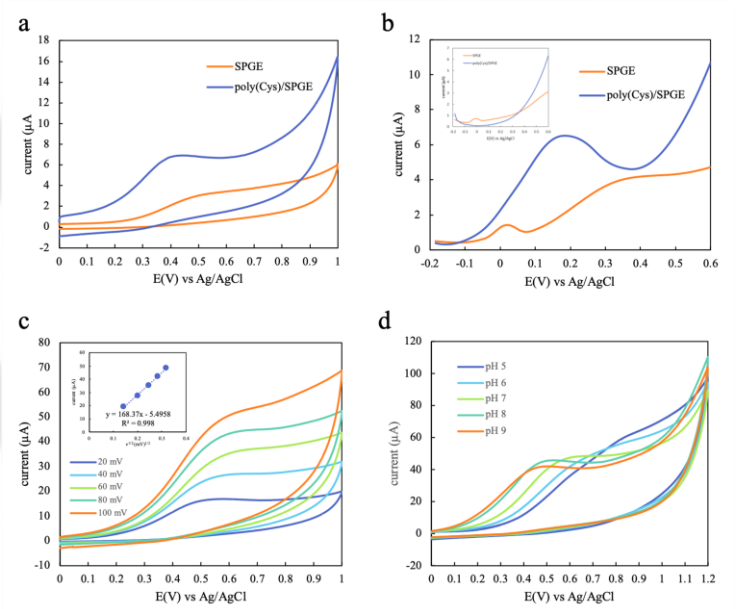

Figure 36 (a) and (b) represent CV and DPV diagrams of 100 μM Cys in PBS at pH = 8.0 using bare SPGE compared to poly(Cys)/SPGE. (c) CV curves of 1 mM Cys in PBS at pH = 8.0 at poly(Cys)/SPGE using different scan rate, inset shows linear relationship between square root of scan rates and electrochemical currents. (d) CV curves of 1 mM Cys in PBS at different pH values.

4.2.3 Optimization of experimental conditions

Several parameters in the modification and detection process were investigated to provide excellent sensitivity and analytical performance for Cys detection. The concentration of L-cysteine monomer and number of cycles in the

electropolymerized modification process were studied. These two parameters are directly involved with the thickness of the polymer at the electrode surface during modification. In Figure 37a and Figure 37b showed L-cysteine monomer at 3 mM and 9 cycle scans reached a maximum point of electrochemical responses. Otherwise, the current oxidation decreases after a maximum point of these two parameters, which might be affected by the thickness of poly(Cys) at the SPGE surface. This leads to obstacles of the electron transfer at the electrode interface. Therefore, 3 mM of L-cysteine monomers with 9 scanned cycle numbers were selected as an optimal condition to modify the poly(Cys) at SPGE. The effect of pH conditions to determine Cys was studied. As shown in Figure 37c, at pH 8.0 exhibited the highest electrochemical response. Thus, 0.1 M PBS at pH 8.0 was chosen for optimal supporting electrolyte employed in this method. In the detection process, quiet time before the electrochemical measurement also was optimized. In Figure 37d, the highest electrochemical response was reached at 2 s, then currents decreased when increasing the quiet time. Therefore, quiet time at 2 s was selected as an optimal condition. The result also indicated that this method provided a rapid analysis.

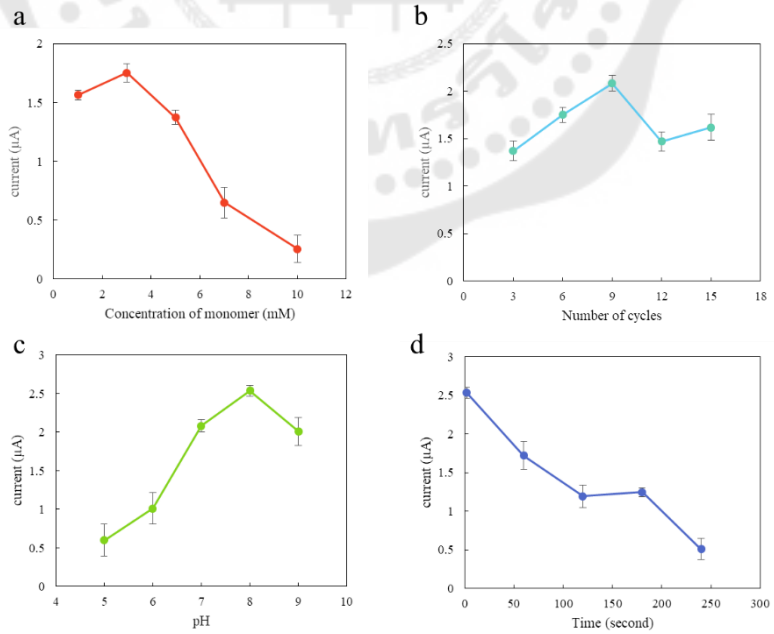

Figure 37 The effect of (a) concentration of L-cysteine monomer (b) number of scans (c) pH of supporting electrolyte (d) quiet time before electrochemical measurement

Moreover, various parameters regarding the DPV technique include increment, amplitude, pulse width, and pulse period were systematically optimized to receive the best analytical performance. These parameters influence the peak shape and the oxidation current of Cys. As shown in Figure 38, the maximum current was observed at an increment of 0.016 V, pulse amplitude of 0.25 V, a pulse width of 0.1 s, and a pulse period of 0.6 s.

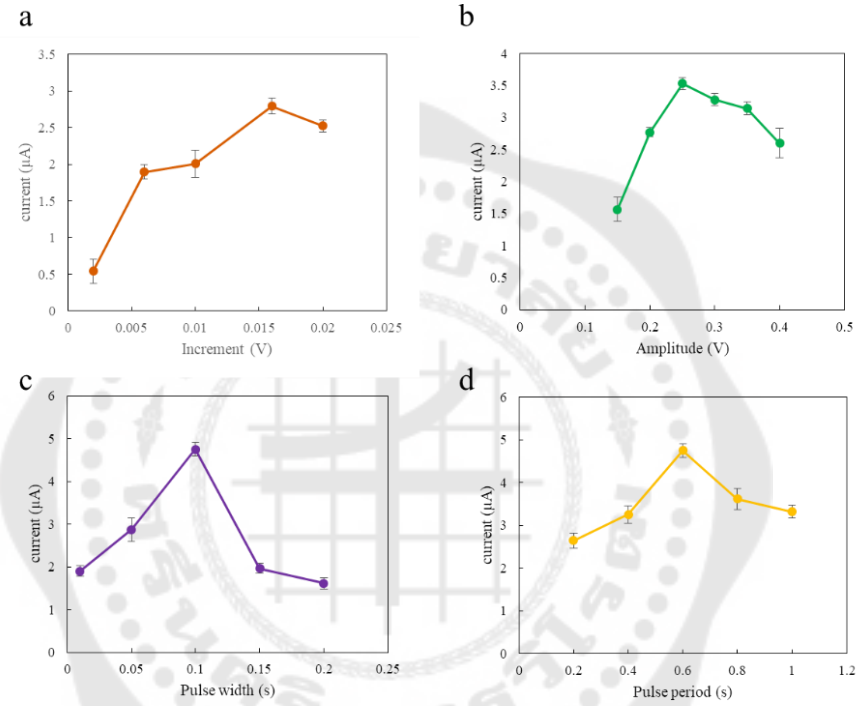

Figure 38 Effect of (a) Increment (b) Amplitude (c) Pulse width (d) Pulse period in DPV technique for the detection of 100 μM Cys in PBS pH 8.0

4.2.4 Analytical performance

The quantitative determination of Cys was performed by DPV based by generating a standard curve (Figure 39a and 39b). The linear concentration range of the sensor was found to be between 10 and 800 μM with a linear regression equation of $i_{pa} = 0.0517C_{Cys} + 0.6941$ ($R^2 = 0.9987$) (Figure 39c). The calculated limit of detection (LOD) was 5.5 μM (3SD/slope). The linear range and LOD obtained from this device are sufficiently sensitive for detecting Cys in food samples which is the main application of this work. Comparing the analytical performance of the proposed platform and the other techniques for the detection of Cys in food products was also performed. The new

platform exhibited a wider linear concentration range and a lower LOD than Raman microspectroscopy (Cebi, Dogan, Develioglu, Yayla, & Sagdic, 2017; Rasheed et al., 2019; Singh et al., 2018; Thota & Ganesh, 2016). Although the LC-MS/MS method (Dogan, Cebi, Develioglu, Olgun, & Sagdic, 2018) offered lower LOD, anyway, the proposed platform allowed for simple sample preparation and operation, sensitive detection, low-cost, and fast analysis. These characteristics lead to a very useful and practical technique for applying to real-world analysis.

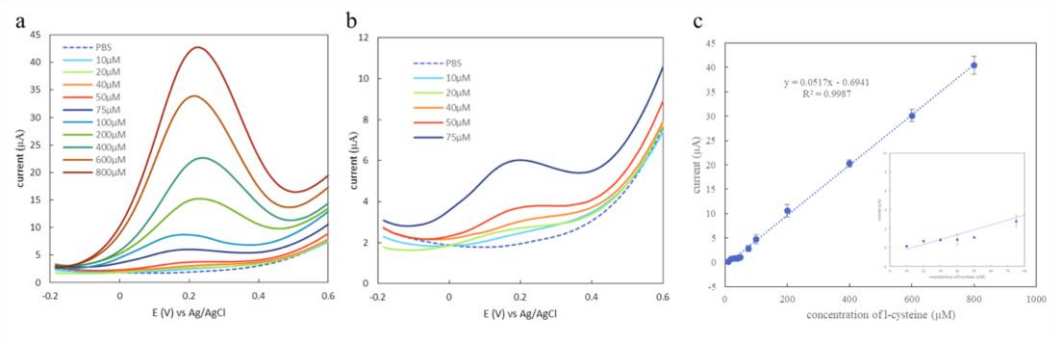

Figure 39 (a) and (b) DPV current responses from 0 μM to 800 μM Cys in PBS pH 8.0. (c) Linear relationship of Cys concentrations and oxidation currents. Error bars were obtained based on three replicates (n=3), standard deviations were shown in the range of 0.04–1.8 μA.

4.2.5 Selectivity

We next explored the specificity by detection of 100 μM Cys in the presence of common food additive compounds found in bakery products, including 1 mM thiamine (vitamin B_1), 1mM nicotinic acid (vitamin B_3), 1 mM folic acid (vitamin B_9), 1 mM ascorbic acid (vitamin C), 10 mM glucose, 10 mM fructose, 10 mM sucrose, 1000 mg/L Na^+, 1000 mg/L Fe^{2+}, and 1000 mg/L Ca^{2+}. In Figure 40, there are no significant change in current (less than 5%) when detecting Cys in the presence of these interferences. Thus, this proposed platform offered an excellent specificity in food samples toward Cys detection.

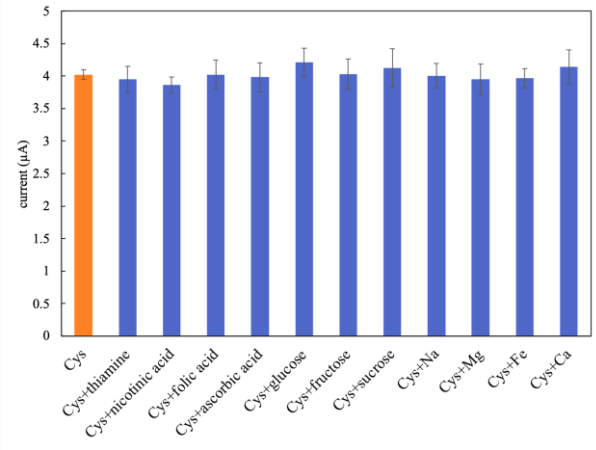

Figure 40 The interference study of the proposed platform for the detection of Cys in the presence of common food additive compounds. Error bars were obtained based on three replicates (n=3), standard deviations were shown in the range of 0.1–0.3 μA.

4.2.6 Real sample analysis

To demonstrate the proposed platform's sensing applicability, the determination of Cys in bakery products was tested. The standard addition method was used to measure the amount of Cys in real samples. The recovery test was studied by spiking the standard Cys (100, 200, and 600 μM) in wheat flours, bread, and cake. The recovery and relative standard deviation values (%) are listed in Table 4 to evaluate the accuracy and precision found in the acceptable value ranges of 84.2%–110.8% and 1.5%–4.9%, respectively. In addition, the amount of Cys was 63.0 mg/kg in wheat flour 1, 13.8 mg/kg in wheat flour 2, 44.6 mg/kg in bread, and 81.0 mg/kg in the cake. These results indicated the powerful sensing ability for the detection of Cys in food products.

Table 4 The analytical application of the proposed platform for the detection of Cys in bakery products (n=3)

Sample	Spiked (μM)	Found (μM)	Recovery (%)	RSD (%)
Wheat flour 1	100	110.8±4.6	110.8	4.2
	200	180.7±1.9	90.3	4.2
	600	604.7±21.3	100.8	3.5

Table 4 (Continued)

Sample	Spiked (μM)	Found (μM)	Recovery (%)	RSD (%)
Wheat flour 2	100	84.2±3.2	84.2	3.8
	200	207.4±7.3	103.7	3.5
	600	599.9±20.2	100.0	3.4
Bread	100	90.8±3.4	90.8	3.7
	200	215.7±9.6	107.8	4.5
	600	595.9±16.5	99.3	2.8
Cake	100	87.9±3.2	87.9	3.7
	200	216.4±3.2	108.2	1.5
	600	594.0±29.1	99.0	4.9

4.3 Electrochemical capillary-flow immunoassay for detecting anti-SARS-CoV-2 nucleocapsid protein antibodies at the point of care

The contents of this section are based on the original research article, see in appendix 3 for the full article.

4.3.1 Electrochemical capillary-flow device design.

The electrochemical capillary-flow device was developed with the aim of detecting anti-SARS-CoV-2 N protein specific antibodies with high sensitivity at the point of care. The design of the capillary-flow device was based on previous POC devices developed by our group (Carrell et al., 2020; Jang et al., 2020; Jang et al., 2021), and incorporated a SPCE to allow high-sensitivity detection. Assembled layers of laser-cut polyester and double-sided adhesive films created the microfluidic circuit shown in Figure 41a. This microfluidic circuit provided sequential delivery of the reagents used in the electrochemical immunoassay to a detection zone. The detection zone consisted of a NCM that was modified with a capturing agent, recombinant SARS-CoV-2 N protein, and a SPCE in contact with it. The SPCE had been plasma treated for improved electrochemical performance, as previously characterized (Kava & Henry, 2021). The

flow was maintained by an absorbent waste pad placed downstream from the detection zone.

The capillary flow-driven assay was initiated by adding a 10-μL sample of whole blood on the blood-filtration membrane. This allowed blood cells to be retained in the membrane, while plasma passed through it and entered the channel. Buffer was then added to the device, simultaneously filling all the device channels by capillary action, as illustrated by the arrows in Figure 41a(ii). This was possible thanks to a bare glass fiber pad (L3, Figure 41a(i)) and a vent hole (L7, Figure 41a(i)) that were added to the buffer channel to prevent air from being trapped. The buffer flow under the blood filtration membrane carried blood plasma to the NCM. If present in the sample, anti-N antibodies bound to the N proteins immobilized on the NCM (Figure 41b). While buffer kept flowing in the channels and through the NCM, washing away unbound sample components, HRP-antibodies were released from the reagent pad placed on L4 (Figure 41a) and subsequently delivered to the NCM. At this point, HRP-antibodies bound to anti-N antibodies if present on the NCM. To prevent non-specific absorption of HRP-antibody the blood filtration membrane, which could act as a passive pump due to evaporation, the center channel was split into two superimposed channels and a hydration channel was incorporated into the device (shown in dark grey in Figure 41a(ii)). This enabled the plasma to flow through the top channel while the washing buffer and the HRP-antibody flow through the bottom one (so called HRP-antibody delivery channel, shown in yellow in Figure 41a(ii)). Both channels converged at the end of the device, after the blood-filtration membrane but before the NCM. Evaporation of solution through the filtration membrane was also minimized by covering it with a lid made of polyester film (Figure 41a(i)). Following HRP-antibody delivery, the excess of HRP-antibody that had not bound to the NCM was washed off automatically by the washing buffer running through the device. Lastly, 1 μL of TMB substrate was added to the substrate inlet on the NCM, as indicated in Figure 41a(ii). From there, it flowed to the detection zone where it was oxidized by HRP when present. The resulting electroactive compound (oxTMB) was finally detected via chronoamperometry using the SPCE held

on the NCM. The complete sandwich immunoassay and electrochemical detection mechanism are illustrated in Figure 41b.

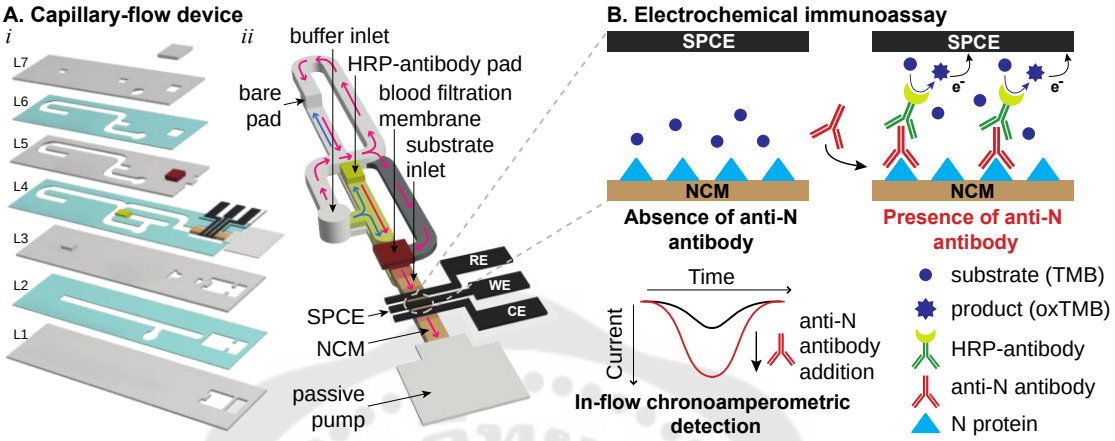

Figure 41 Schematic overview of the electrochemical capillary-flow immunoassay. (a) Exploded view (i) and 3-dimensional view (ii) of the capillary-flow device incorporating a stencil printed carbon electrode (SPCE) facing a nitrocellulose membrane (NCM). Exploded view (i) shows the 4 layers of polyester film (grey, L1, L3, L5, L7) and the 3 layers of double-sided adhesive (turquoise, L2, L4, L6) assembled to create the 3-dimensional microfluidic network represented in (ii). (b) Electrochemical immunoassay and detection mechanism.

4.3.2 Sequential delivery of reagents

The ability of the capillary-flow device to sequentially deliver reagents to the detection zone was demonstrated with a whole blood sample and color dyes to mimic reagents, as shown in Figure 42. Once the sample and the buffer were introduced in the device, the flow started and pulled the plasma through the NCM in 1 min (Figure 42a). Efficient blood cell filtration through the filtration membrane was confirmed by visually assessing the color of the solution flowing through the NCM and the absorbent waste pad. While dark red residue remained on the membrane, the fluid emerging through the membrane was clear (Figure 42a). This observation is consistent with results published by our group and others (Carrell et al., 2020; C. Liu et al., 2016; Su et al., 2020). Following plasma delivery to the NCM and a subsequent buffer wash (Figure 42b), the

yellow dye that had been dried on the reagent pad to mimic HRP-antibody was released through the HRP-antibody delivery channel and flowed to the detection zone (Figure 42c, 12 min). Simultaneously, buffer flowed through the hydration channel to keep the blood filtration membrane hydrated, driving the flow to the NCM. After approximately 1 min, the HRP-antibody-mimicking yellow solution stopped flowing through the NCM and washing buffer from the buffer channel was delivered instead, to wash out excess HRP-antibody (Figure 42d). Lastly, 1 μL of substrate-mimicking blue solution was added to the device at time 16 min and flowed past the detection zone in 4 min (Figure 42e, 20 min). Overall, these results confirm that the reagents are sequentially delivered to the detection zone in less than 20 min. Estimated incubation periods in the devices are 3 min for blood, 6 min for rehydrated HRP-antibody and 4 min for TMB on the detection zone, with automatic buffer washes between them.

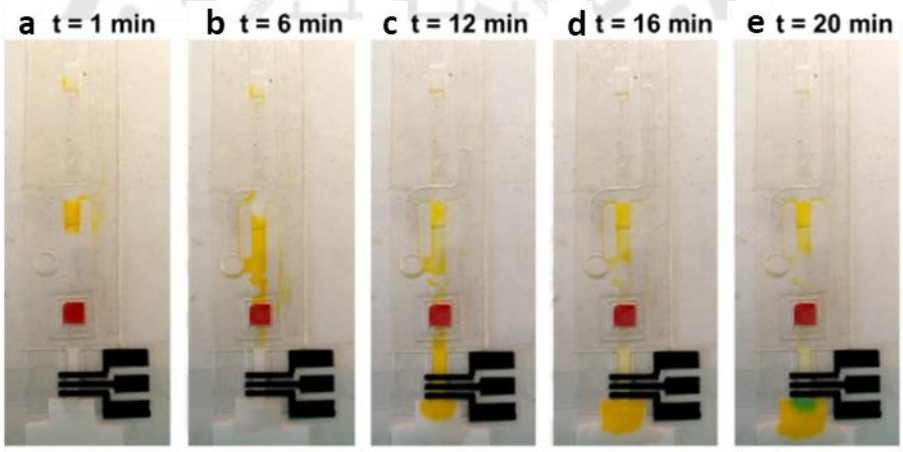

Figure 42 Sequential delivery of blood sample (a), washing buffer (b), HRP-antibodies (c) washing buffer (d) and TMB (e) to the detection area. HRP-antibody and TMB solutions are represented by yellow and blue dyes, respectively.

4.3.3 Static electrochemical detection of anti-N antibodies

Initial anti-N antibody assays were performed on PBS-based samples using a capillary-flow device identical to the one shown in Figure 41b, but without a blood filtration membrane and a hydration channel (Figure 43). The first anti-N antibody measurements were carried out under static conditions. In this set up, the NCM was removed from the capillary-flow device upon completion of the fluidic assay and before

addition of 1 µL of TMB substrate. Chronoamperometry measurements were started 2 min after the addition of TMB to the NCM. Three SPCEs were successively connected to several NCMs exposed to different anti-N antibody concentrations. Figure 44a displays the chronoamperograms recorded from a single SPCE exposed to five anti-N antibody concentrations ranging from 0 to 1 µg/mL and the calibration curve generated by this dataset is shown in Figure 44b, together with calibration curves of the other two SPCEs (insert).

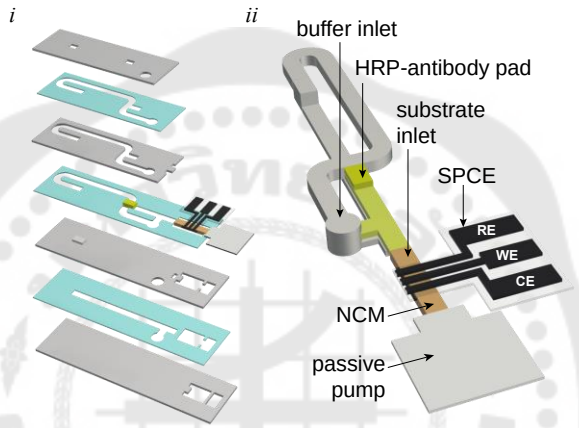

Figure 43 Capillary-flow device for PBS-based sample testing. Schematic of the capillary-flow device used for PBS-based sample testing. This device is identical to the one shown in Figure 41 of the main manuscript, except for the absence of both the blood-filtration membrane and the membrane hydration channel. (i) Exploded view of the capillary-flow device showing the 4 layers of polyester film (grey) and the 3 layers of double-sided adhesive (turquoise) assembled to create the 3-dimensional microfluidic network represented in (ii). (ii) 3-dimensional view of the device.

The current-to-concentration response of each SPCE followed a 4-parameter logistic (4PL) model, which is typical for immunoassays (O'Connell, Belanger, & Haaland, 1993). Inherent variability of electrodes that are stencil printed by hand resulted in different limits of detection (LOD) across the 3 SPCEs. Nevertheless, all three LODs were below 2 ng/mL, demonstrating the ability of this assay to consistently detect anti-N antibody concentrations in 5-µL PBS samples down to the low ng/mL range, which outperforms commercially available ("ABIN6952772 SARS-CoV-2 N-Protein IgG

Antibody (SARS-CoV-2 N IgG) ELISA Kit," ; "Anti-SARS-CoV-2 N protein Human IgG ELISA Kit Elisa Kit KE30001 Proteintech,") as well as recently-developed POC anti-N antibody assays (Kasetsirikul et al., 2020; Seunghyeon Kim et al., 2021; Z. Wang et al., 2020). These results prove that the capillary-flow device successfully delivers sample and detection antibody to the NCM and performs effective washing steps. It also demonstrates successful electrochemical detection of TMB as the immunoassay substrate, using a SPCE placed directly on the NCM.

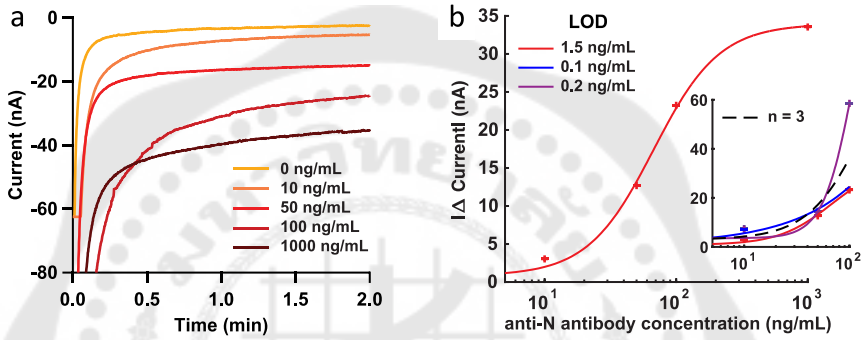

Figure 44 Static electrochemical detection of anti-N antibodies in PBS samples. (a) Chronoamperograms obtained from one SPCE consecutively connected to the NCM taken from five capillary-flow devices, each exposed to a 5-µL PBS-based sample of distinct anti-N antibody concentration. (b) Corresponding calibration curve showing blank-subtracted current at t=100 s (red). (Insert), amplification of B showing the measurements recorded with three independent SPCEs (red, blue and purple) and overall signal fit (black dashed line). Markers and error bars represent average and standard deviation (sd) over a 10 s interval centered in 100 s. Data fitted with a 4PL regression. LODs are calculated as the anti-N concentration corresponding to 3 sd of the blank signal.

4.3.4 In-flow electrochemical detection of anti-N antibodies

Following preliminary results in the static measurement setup, flow-based anti-N antibody tests were performed on PBS-based samples by running chronoamperometry under flow conditions. Chronoamperometry measurements were started upon delivery of buffer to the detection zone and ended upon flow completion.

Three SPCEs were successively connected to four capillary-flow devices that were supplied with PBS-based samples of four different anti-N antibody concentrations ranging from 0 to 100 ng/mL.

Under flow conditions, delivery of TMB to the detection zone produced a transient increase in the cathodic current (Figure 45a) that correlated to the concentration of anti-N antibody in the sample (Figure 45b). As in the static measurement setup, the current-to-concentration response of each SPCE followed a 4PL model and variability between electrodes stencil printed by hand was observed. LODs obtained were slightly higher than those achieved in the static setup, which can be due to dispersive blurring of TMB in the microfluidic flow. However, in-flow detection of anti-N antibodies in the low ng/mL range was still possible.

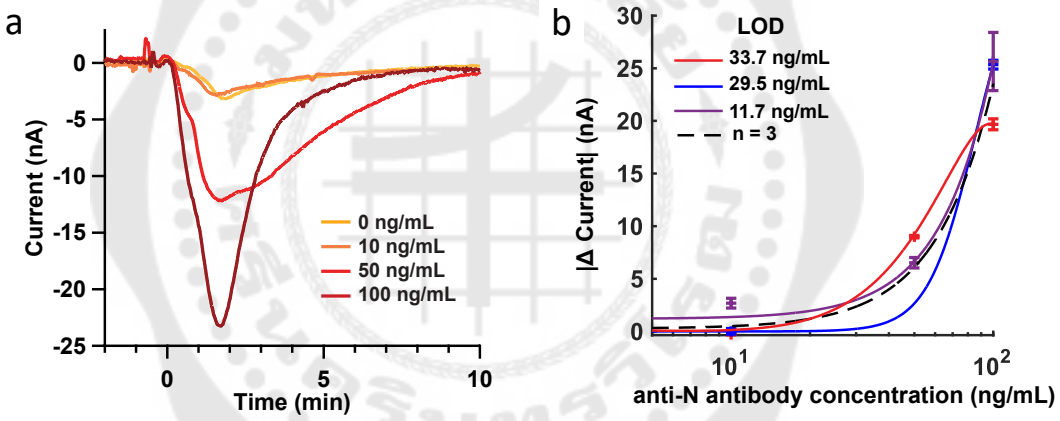

Figure 45 In-flow electrochemical detection of anti-N antibodies in PBS samples. (a) Excerpt of chronoamperograms recorded from one SPCE consecutively connected to four different capillary flow-devices, each supplied with a 5 µL PBS-based sample of distinct anti-N antibody concentration. Data was time-aligned with TMB delivery to the detection zone (t = 0). (b) Calibration curves obtained for three independent SPCEs (red from data shown in a, blue and purple) and overall fit for all three SPCEs (black dashed line). Markers and error bars represent average and sd over a 30 s interval centered in the current local minimum. Blank signal is subtracted from data. Data fitted with a 4PL regression. LODs are calculated as the anti-N concentration corresponding to 3 sd of the blank signal.

4.3.5 Detection of anti-N antibodies in whole human blood

Finally, whole human blood was spiked with different anti-N antibody concentrations ranging from 0 to 100 ng/mL. These samples were run on the complete fluidic device integrating the blood filtration membrane, as shown in Figure 41, and chronoamperometry measurements were carried out under flow conditions, as described previously. Three SPCEs were successively connected to four capillary-flow devices running these whole blood samples spiked with anti-N antibodies. In-flow chronoamperograms from one SPCE (Figure 46a) show the increase in the cathodic current recorded upon delivery of TMB to the detection zone. The correlation between the magnitude of this current and the concentration of anti-N antibody in the whole blood samples is shown in Figure 46b for all three SPCEs.

As for PBS-based samples, the current-to-concentration response of each SPCE followed a 4PL model and variability between electrodes was observed. This is shown by the difference in the magnitude of current response observed between the three SPCEs, and highlights the variability of our current electrochemical device. The magnitude of the currents recorded here was 20 times higher than for PBS-based samples. This signal increase was attributed to three main causes: (i) blood sample volume was 10 µL instead of 5 µL for the PBS-based samples, to cover the entire surface of the blood filtration membrane and to maximize analyte extraction; (ii) delivery of blood sample to the NCM was slowed down by the blood filtration membrane, allowing longer sample incubation time on the detection zone, hence enhancing analyte capture; and (iii) the higher viscosity of plasma compared to PBS could further decrease the sample flowrate through the NCM. The increased signal magnitude for whole blood samples lead to improved analytical performance, with higher sensitivity and lower LODs down to the 5 ng/mL range (Figure 46), which matches that of commercially available tests ("ABIN6952772 SARS-CoV-2 N-Protein IgG Antibody (SARS-CoV-2 N IgG) ELISA Kit," ; "Anti-SARS-CoV-2 N protein Human IgG ELISA Kit Elisa Kit KE30001 Proteintech,"). Table 5 provides a side-by-side comparison of the performance of our electrochemical capillary-flow device in relation to other tests for SARS-CoV-2 anti N

antibodies reported in the literature or commercially available. Note that our device is the only one providing a quantitative detection in whole blood samples at the point of care.

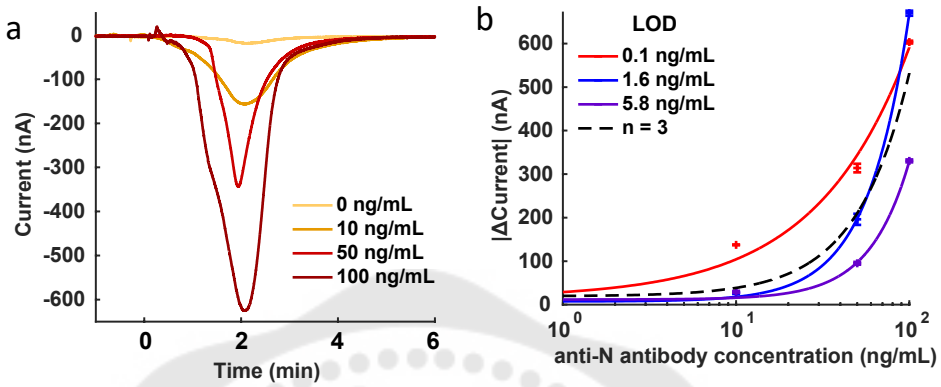

Figure 46 In-flow detection of anti-N antibodies in human whole blood samples. (a) Representative chronoamperograms recorded from one SPCE consecutively connected to four different capillary flow-devices supplied with 10-µL human whole blood samples spiked with different anti-N antibody concentrations. Data was time-aligned with TMB delivery to the detection zone (t = 0). (b) Calibration curves recorded with three independent SPCEs (red from data shown in a, blue and purple) and overall fit for all three SPCEs (black dashed line). Markers and error bars represent average and sd over a 30 s interval centered in the current local minimum. Blank signal is subtracted from data. Data fitted with a 4PL regression. LODs are calculated as the anti-N concentration corresponding to 3 sd of the blank signal.

Table 5 Estimated device cost. Estimated cost breakdown of reagents and materials for each device.

Technique	Sample matrix	LOD	Time	Cost	Ref.
Electrochemical LFIA	Whole blood	5 ng/mL	20 min	<$0.5	This work
Vertical-flow paper-based assay	Serum	750 ng/mL	15 min	Not reported	(S. Kim et al., 2021)

Table 5 (Continued)

Technique	Sample matrix	LOD	Time	Cost	Ref.
Luciferase immunosorbent assay	Serum	0.4 ng/mL	>1 day	Not reported	(Liang et al., 2021)
LFIA based on superparamagnetic nanoparticles	Buffer	5 ng/mL	10 min	Not reported	(Bayin et al., 2021)
Paper-based ELISA	Serum	9 mg/mL	30 min	$1.5	(Kasetsirikul et al., 2020)
Disposable ELISA	Whole blood	2.8 ng/mL	20 min	~$1	(Carrell et al., 2020)
Well plate ELISA kit	Serum or plasma	3.9 ng/mL	>1 day	$682/96	("ABIN6952772 SARS-CoV-2 N-Protein IgG Antibody (SARS-CoV-2 N IgG) ELISA Kit,"))
Indirect ELISA kit	Plasma	8 ng/mL	~2 h	$399/96	(("Anti-SARS-CoV-2 N protein Human IgG ELISA Kit Elisa Kit KE30001 Proteintech,")

4.3.6 Proof-of-concept detection on a smartphone

As a proof-of-concept experiment, the electrochemical capillary-flow device was coupled to an NFC potentiostat operated by a smartphone and this truly portable system was used to detect anti-N antibodies in whole blood samples. Commonly available in smartphones, NFC is a low-cost technology that enables wireless communication using a simple setup, making it ideal for use in POC applications. The NFC potentiostat (SIC4341, ISO14443A, Silicon Craft Technology PLC) was operated by an Android smartphone (Motorola One, XT1941) running a mobile application made available by Silicon Craft (SIC4341 Allstar Android app). The electrochemical capillary-flow device was connected to the NFC potentiostat via a socket mounted on the NFC potentiostat printed circuit board, in which the SPCE was inserted, as shown in Figure 47a.

The connection between the NFC potentiostat and the smartphone was established by simply placing the smartphone over the NFC potentiostat, and this wireless connection automatically powered it. First, basic electrochemistry was performed to demonstrate the well-functioning of the NFC potentiostat. A cyclic voltammogram recorded from a SPCE in ferri/ferrocyanide is shown in Figure 48. Then, to demonstrate the capability of this system to detect anti-N antibody, two electrochemical capillary-flow devices supplied with PBS-based samples of 0 (blank sample) and 1 µg/mL anti-N antibody were run and chronoamperometry was performed using the NFC potentiostat. The current responses from these two measurements are displayed in Figure 47a. A clear increase in the cathodic current recorded from the 1 µg/mL anti-N antibody sample was observed while the current from the blank sample remained constant throughout the 5 min measurement. While the concentration of anti-N antibody tested here was higher than the targeted clinical range, this proof-of-concept experiment demonstrates the capacity of the NFC potentiostat to be used for this assay. Further optimization of the NFC potentiostat current range is needed to allow the detection of current responses generated by samples of low anti-N antibody

concentrations. This fully portable wireless smartphone-based system would greatly facilitate detection at the point of care.

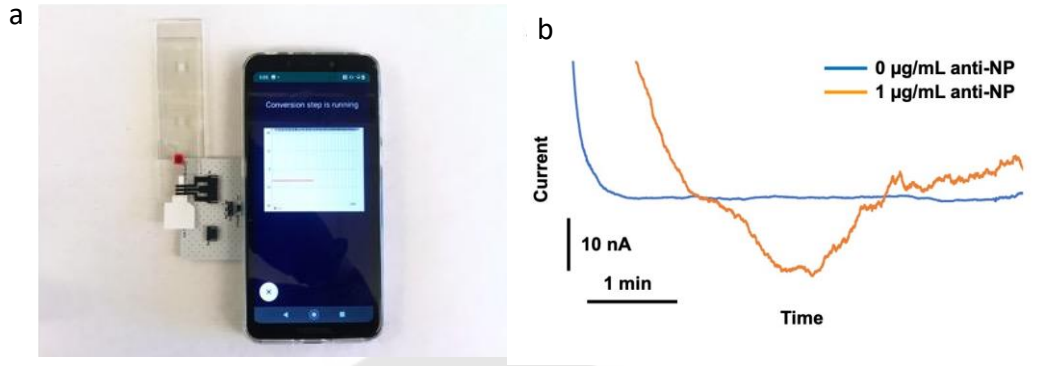

Figure 47 (a) Picture of the whole smartphone-based detection system, showing the electrochemical capillary-flow device connected to the NFC potentiostat, which is wirelessly operated from a smartphone. (b) In-flow chronoamperograms wirelessly recorded using the NFC potentiostat operated by a smartphone. Data is from two different capillary flow-devices supplied with 5-µL PBS-based samples of 0 and 1 µg/mL anti-N antibody concentrations.

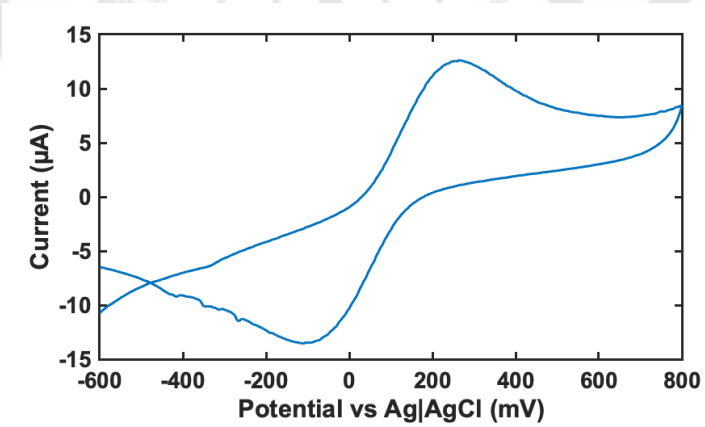

Figure 48 Cyclic voltammogram recorded from the NFC potentiostat. Cyclic voltammogram (CV) recorded from a stencil-printed carbon electrode (SPCE) in ferri/ferrocyanide using the NFC potentiostat. A 50 µL volume of 0.5 mM ferri/ferrocyanide in 0.1 M potassium nitrate was held on the SPCE using a well made of double-sided adhesive. Potential was scanned at 100 mV/s.

CHAPTER 5
CONCLUSIONS AND FUTURE WORKS

5.1 Conclusions

The outstanding strategies of miniaturized electrochemical devices for detection of important analytes were concluded as follow:

5.1.1 A multilayer microfluidic paper coupled with an electrochemical platform developed for sample separation and detection of dopamine

A newly engineered design of multilayer eμPAD which combined multistep for successive sample separation and detection of DA in the presence of AA as a common interference that can be found in biological samples. Nafion is deposited in paper microchannel, which works as an ion selective membrane to provide high selectivity by blocking AA from electrochemical detection of DA. Also, the device architecture allowed fast and quasi-steady flow rate to improve mass transfer kinetic of DA on electrode surface, then electrochemical response provided 2-time higher than simple device. A linear working concentration range of 1–200 μM, and LOD of 0.41 μM (3SD/slope) were obtained. Additionally, this analytical platform was applied for detection of DA in artificial urine samples which resulted in good recoveries and reliable results compared with UV-vis method.

5.1.2 A Novel L-cysteine sensor using in-situ electropolymerization of L-cysteine: potential to simple and selective detection

The first use of self-modification of poly(Cys) film modified SPGE for the electrochemical detection of Cys in food matrix samples was performed. Here, Cys was used as a monomer for electropolymerization at electrode surfaces to provide excellent electrocatalytic properties for the Cys detection. Several electrochemical studies were used to confirm polymeric film and electrochemical behavior of Cys at electrode surface. In addition, the new all-in-one electrochemical oPAD was constructed. The combination of electropolymerized modification and detection steps into a single device, that achieved the goals to improve precise results from device-to-device, avoids Cys contamination from modification to detection steps, and offers more convenient method

for the end-users. The interference effects were investigated to display the powerful ability of this sensing device for detection of Cys in bakery products. Under the optimized conditions, A linearity was found to be of 10–800 μM with a LOD of 5.5 μM. Finally, the recoveries were utilized to prove the accuracy of this method for detection of Cys in food product samples such as, wheat flour, bread, and cake. This novel sensor opens the vision of a model electrochemical device toward the food quality control and Halal food investigation applications.

5.1.3 Electrochemical capillary-flow immunoassay for detecting anti-SARS-CoV-2 nucleocapsid protein antibodies at the point of care

The alternatively lamination-based method was applied to develop capillary-driven microfluidic devices and combined with electrochemical detection for serology testing of SARS-CoV-2. This device integrated LFIA and SPE for rapid operation and highly sensitive detection of anti-N antibody. The device geometry of multilayer stacked from polyester film and DSA, that enabled sequential delivery of solution without using an external pumping machine. Hence, whole blood sample, secondary antibody, and washing buffer automating transported to detection zone on NCM where capture N protein was immobilized. At the detection zone, SPE was aligned above NCM to perform real-time chronoamperometric measurement. The device system minimized pipetting steps and analysis time for the ideal user-friendly to answer POC concept. The reliably working concentration range exhibited from 10 to 100 ng/mL and the LOD can be detected at 5 ng/mL of anti-N protein while using 10 μL from a human whole blood sample. Lastly, as a proof-of-concept for wireless portable SAR-CoV-2 diagnostic device, this sensing device was achievably integrated with NFC potentiostat operated by smartphone. This idea concept gets closer to the ideal of fully portable clinical diagnostic tools in the future.

5.2 Future works

The novelty of three developed electrochemical sensors provided a high beneficial impact as powerful analytical tools for clinical diagnostic and food analysis aspects. The simple fabrication, miniaturized devices and the use of low-cost materials permit assay to move from central laboratory to on-field analysis and/or in resource-

limited areas. Therefore, based on the knowledge of this dissertation, next steps will focus on the use of paper- and flexible thin film-based for the development of new analytical systems for detection of other important analytes. The strategies in flow-based systems and folding devices could be advantages to facilitate more convenient, powerful and speedy analytical methods. These models give them the opportunity to apply for a wide range of analytical applications, such as clinical diagnosis, food control and safety, and environmental monitoring in the future.

REFERENCES

ABIN6952772 SARS-CoV-2 N-Protein IgG Antibody (SARS-CoV-2 N IgG) ELISA Kit. (11 July 2021). https://www.antibodies-online.com/productsheets/ABIN6952772.pdf

Adkins, J., Boehle, K., & Henry, C. (2015). Electrochemical paper-based microfluidic devices. *Electrophoresis, 36*(16), 1811-1824.

Adkins, J. A., Noviana, E., & Henry, C. S. (2016). Development of a Quasi-Steady Flow Electrochemical Paper-Based Analytical Device. *Anal Chem, 88*(21), 10639-10647.

Akyazi, T., Basabe-Desmonts, L., & Benito-Lopez, F. (2018). Review on microfluidic paper-based analytical devices towards commercialisation. *Anal Chim Acta, 1001*, 1-17.

Anti-SARS-CoV-2 N protein Human IgG ELISA Kit Elisa Kit KE30001 Proteintech. (11 July 2021). https://www.ptglab.com/Products/Pictures/pdf/Virus-IgG-for-2019-nCoV-N-protein-ELISA-Kit-KE30001-datasheet.pdf

Augustyn, A., Bauer, P., Duignan, B., Eldridge, A., Gregersen, E., Luebering, J. E., . . . Zelazko, A. Dopamine CHEMICAL COMPOUND. https://www.britannica.com/science/dopamine

Babaei, A., & Taheri, A. R. (2013). Nafion/Ni(OH)2 nanoparticles-carbon nanotube composite modified glassy carbon electrode as a sensor for simultaneous determination of dopamine and serotonin in the presence of ascorbic acid. *Sens Actuators B Chem, 176*, 543-551.

Ballin, N. Z., Vogensen, F. K., & Karlsson, A. H. (2009). Species determination - Can we detect and quantify meat adulteration? In *Meat Science* (Vol. 83, pp. 165-174): Elsevier.

Bard, A. J., & Faulkner, L. R. (2001). *Electrochemical methods : fundamentals and applications* (2nd). New York: Wiley.

Basinc. Pulse Voltammetric Techniques. https://www.basinc.com/manuals/EC_epsilon/Techniques/Pulse/pulse

Bayin, Q., Huang, L., Ren, C., Fu, Y., Ma, X., & Guo, J. (2021). Anti-SARS-CoV-2 IgG and IgM detection with a GMR based LFIA system. *Talanta, 227*, 122207.

Boni, A. C., Wong, A., Dutra, R. A. F., & Sotomayor, M. D. P. T. (2011). Cobalt phthalocyanine as a biomimetic catalyst in the amperometric quantification of dipyrone using FIA. *Talanta, 85*(4), 2067-2073.

Carrell, C., Link, J., Jang, I., Terry, J., Scherman, M., Call, Z., . . . Henry, C. (2020). Point-of-Need Disposable ELISA System for COVID-19 Serology Testing.

Cebi, N., Dogan, C. E., Develioglu, A., Yayla, M. E., & Sagdic, O. (2017). Detection of l-Cysteine in wheat flour by Raman microspectroscopy combined chemometrics of HCA and PCA. *Food Chem, 228*, 116-124.

Channon, R. B., Menger, R. F., Wang, W., Carrão, D. B., Vallabhuneni, S., Kota, A. K., & Henry, C. S. (2021). Design and application of a self-pumping microfluidic staggered herringbone mixer. *Microfluidics and Nanofluidics, 25*(4), 31-31.

Channon, R. B., Nguyen, M. P., Scorzelli, A. G., Henry, E. M., Volckens, J., Dandy, D. S., & Henry, C. S. (2018). Rapid flow in multilayer microfluidic paper-based analytical devices. *Lab on a Chip, 18*(5), 793-802.

Charoenkitamorn, K., Chaiyo, S., Chailapakul, O., & Siangproh, W. (2018). Low-cost and disposable sensors for the simultaneous determination of coenzyme Q10 and alpha-lipoic acid using manganese (IV) oxide-modified screen-printed graphene electrodes. *Anal Chim Acta, 1004*, 22-31.

Chen, C.-A., Yuan, H., Chen, C.-W., Chien, Y.-S., Sheng, W.-H., & Chen, C.-F. (2021). An electricity- and instrument-free infectious disease sensor based on a 3D origami paper-based analytical device. *Lab on a Chip, 21*(10), 1908-1915.

Chen, C. A., Yeh, W. S., Tsai, T. T., Li, Y. D., & Chen, C. F. (2019). Three-dimensional origami paper-based device for portable immunoassay applications. *Lab on a Chip, 19*(4), 598-607.

Cheng, M., Zhang, X., Wang, M., Huang, H., & Ma, J. (2017). A facile electrochemical sensor based on well-dispersed graphene-molybdenum disulfide modified electrode for highly sensitive detection of dopamine. *J. Electroanal. Chem., 786*, 1-7.

da Costa, E. T., Mora, M. F., Willis, P. A., do Lago, C. L., Jiao, H., & Garcia, C. D. (2014).

Getting started with open-hardware: Development and control of microfluidic devices. *Electrophoresis, 35*(16), 2370-2377.

de Fatima Ulbrich, K., Winiarski, J. P., Jost, C. L., & Maduro de Campos, C. E. (2020). Mechanochemical synthesis of a Ni3-xTe2 nanocrystalline composite and its application for simultaneous electrochemical detection of dopamine and adrenaline. *Composites Part B: Engineering, 183*, 107649-107649.

De Souza, F. R., Alves, G. L., & Coltro, W. K. T. (2012). Capillary-driven toner-based microfluidic devices for clinical diagnostics with colorimetric detection. *Analytical Chemistry, 84*(21), 9002-9007.

Dempsey, E., & Rathod, D. (2018). Disposable Printed Lateral Flow Electrochemical Immunosensors for Human Cardiac Troponin T. *IEEE Sensors Journal, 18*(5), 1828-1834.

Dickinson, E. (2013, 14 january 2019). Modeling Electroanalysis: Cyclic Voltammetry. https://www.comsol.com/blogs/modeling-electroanalysis-cyclic-voltammetry/

Dogan, C. E., Cebi, N., Develioglu, A., Olgun, E. O., & Sagdic, O. (2018). Detection of cystine and cysteine in wheat flour using a robust LC-MS/MS method. *J. Cereal Sci., 84*, 49-54.

Dropsens. Screen-printed electrodes. http://www.dropsens.com/en/screen_printed_electrodes_pag.html

Dungchai, W., Chailapakul, O., & Henry, C. S. (2009). Electrochemical detection for paper-based microfluidics. *Anal Chem, 81*(14), 5821-5826.

ELISA Fundamental Principle, How It Works. (8 July 2021). https://www.bosterbio.com/protocol-and-troubleshooting/elisa-principle

Elizalde, E., Urteaga, R., & Berli, C. L. A. (2015). Rational design of capillary-driven flows for paper-based microfluidics. *Lab on a Chip, 15*(10), 2173-2180.

Fagre, A., Lewis, J., Eckley, M., Zhan, S., Rocha, S. M., Sexton, N. R., . . . Schountz, T. (2021). SARS-CoV-2 infection, neuropathogenesis and transmission among deer mice: Implications for spillback to New World rodents. *PLOS Pathogens, 17*(5), e1009585-e1009585.

Ferraz, B. R., Leite, F. R., & Malagutti, A. R. (2016). Simultaneous determination of ethionamide and pyrazinamide using poly(l-cysteine) film-modified glassy carbon electrode. *Talanta, 154*, 197-207.

Fiala, R. (2017, 28 January 2019). Cycling Voltammetry: principle. https://physics.mff.cuni.cz/kfpp/povrchy/method/cv-principles

Geng, D., Li, M., Bo, X., & Guo, L. (2016). Molybdenum nitride/nitrogen-doped multi-walled carbon nanotubes hybrid nanocomposites as novel electrochemical sensor for detection L-cysteine. *Sens. Actuators B Chem., 237*, 581-590.

Guo, L., Zhang, Y., & Li, Q. (2009). Spectrophotometric determination of dopamine hydrochloride in pharmaceutical, banana, urine and serum samples by potassium ferricyanide-Fe(III). *Anal Sci, 25*(12), 1451-1455.

Halal Certification for Food, Cosmetics and Pharmaceutilcal products (8 July 2021). https://www.halalcs.org/en/#section-1259

Harvey, D. (2021, 8 July 2021). Voltammetric and Amperometric Methods. https://chem.libretexts.org/Bookshelves/Analytical_Chemistry/Book%3A_Analytical_Chemistry_2.1_(Harvey)/11%3A_Electrochemical_Methods/11.04%3A_Voltammetric_and_Amperometric_Methods

Heinze, J. (1984). Cyclic Voltammetry-"Electrochemical Spectroscopy". *Angewandte Chemie, 23*(11), 831-918.

Honeychurch, K. C. (2012). 13 - Printed thick-film biosensors M. Prudenziati & J. Hormadaly *Printed Films* (pp. 366-409): Woodhead Publishing.

Horlock, C. (8 July 2021). Enzyme-linked immunosorbent assay (ELISA) https://www.immunology.org/public-information/bitesized-immunology/experimental-techniques/enzyme-linked-immunosorbent-assay

Islam, M., Natu, R., & Martinez-Duarte, R. (2015). A study on the limits and advantages of using a desktop cutter plotter to fabricate microfluidic networks. *Microfluidics and Nanofluidics, 19*(4), 973-985.

Jang, I., Carraõ, D. B., Menger, R. F., Moraes De Oliveira, A. R., & Henry, C. S. (2020). Pump-Free Microfluidic Rapid Mixer Combined with a Paper-Based Channel. *ACS*

Sensors, 5(7), 2230-2238.

Jang, I., Kang, H., Song, S., Dandy, D. S., Geiss, B. J., & Henry, C. S. (2021). Flow control in a laminate capillary-driven microfluidic device. *Analyst, 146*(6), 1932-1939.

Karahalil, E. (2020). Principles of halal-compliant fermentations: Microbial alternatives for the halal food industry. In *Trends in Food Science and Technology* (Vol. 98, pp. 1-9): Elsevier Ltd.

Kasetsirikul, S., Umer, M., Soda, N., Sreejith, K. R., Shiddiky, M. J. A., & Nguyen, N. T. (2020). Detection of the SARS-CoV-2 humanized antibody with paper-based ELISA. *Analyst, 145*(23), 7680-7686.

Kaur, B., Pandiyan, T., Satpati, B., & Srivastava, R. (2013). Simultaneous and sensitive determination of ascorbic acid, dopamine, uric acid, and tryptophan with silver nanoparticles-decorated reduced graphene oxide modified electrode. *Colloids Surf B Biointerfaces, 111*, 97-106.

Kava, A. A., & Henry, C. S. (2021). Exploring carbon particle type and plasma treatment to improve electrochemical properties of stencil-printed carbon electrodes. *Talanta, 221*, 121553-121553.

Kelly, M., Tarbin, J. A., Ashwin, H., & Sharman, M. (2006). Verification of compliance with organic meat production standards by detection of permitted and nonpermitted uses of veterinary medicines (tetracycline antibiotics). *Journal of Agricultural and Food Chemistry, 54*(4), 1523-1529.

Khamcharoen, W., Henry, C. S., & Siangproh, W. (2022). A novel l-cysteine sensor using in-situ electropolymerization of l-cysteine: Potential to simple and selective detection. *Talanta, 237*, 122983.

Khamcharoen, W., & Siangproh, W. (2021). A multilayer microfluidic paper coupled with an electrochemical platform developed for sample separation and detection of dopamine. *New Journal of Chemistry, 45*(29), 12886-12894.

Kim, S., Hao, Y., Miller, E. A., Tay, D. M. Y., Yee, E., Kongsuphol, P., . . . Sikes, H. D. (2021). Vertical Flow Cellulose-Based Assays for SARS-CoV-2 Antibody Detection in Human Serum. *ACS Sensors, 6*(5), 1891-1898.

Kim, S., Hao, Y., Miller, E. A., Tay, D. M. Y., Yee, E., Kongsuphol, P., . . . Sikes, H. D. (2021). Vertical Flow Cellulose-Based Assays for SARS-CoV-2 Antibody Detection in Human Serum. *ACS Sens, 6*(5), 1891-1898.

Konkel, L. (2018). What Is Dopamine? https://www.everydayhealth.com/dopamine/

Krishnan, R. G., & Saraswathyamma, B. (2021). Electro-generated poly (cysteine) film as a sensor platform towards the simultaneous electroanalysis of hydrazine and hydroxylamine. *Mater. Chem. Phys., 271*, 124880-124880.

Kumar, D. R., Kesavan, S., Nguyen, T. T., Hwang, J., Lamiel, C., & Shim, J. J. (2017). Polydopamine@electrochemically reduced graphene oxide-modified electrode for electrochemical detection of free-chlorine. *Sens Actuators B Chem., 240*, 818-828.

Lee, J. H., Choi, M., Jung, Y., Lee, S. K., Lee, C. S., Kim, J., . . . Kim, H. G. (2021). A novel rapid detection for SARS-CoV-2 spike 1 antigens using human angiotensin converting enzyme 2 (ACE2). *Biosensors and Bioelectronics, 171*, 112715-112715.

Li, Z., Yi, Y., Luo, X., Xiong, N., Liu, Y., Li, S., . . . Ye, F. (2020). Development and clinical application of a rapid IgM-IgG combined antibody test for SARS-CoV-2 infection diagnosis. *Journal of Medical Virology, 92*(9), 1518-1524.

Liang, Y., Yan, H., Huang, L., Zhao, J., Wang, H., Kang, M., . . . Tang, S. (2021). A luciferase immunosorbent assay for quantitative detection of IgG antibodies against SARS-CoV-2 nucleoprotein. *J Virol Methods, 292*, 114141.

Liu, C., Liao, S.-C., Song, J., Mauk, M. G., Li, X., Wu, G., . . . Bau, H. H. (2016). A high-efficiency superhydrophobic plasma separator. *Lab on a Chip, 16*(3), 553-560.

Liu, H., & Crooks, R. M. (2011). Three-dimensional paper microfluidic devices assembled using the principles of origami. *J Am Chem Soc, 133*(44), 17564-17566.

Liu, X., Luo, L., Ding, Y., & Ye, D. (2011). Poly-glutamic acid modified carbon nanotube-doped carbon paste electrode for sensitive detection of L-tryptophan. *Bioelectrochemistry, 82*(1), 38-45.

Liu, X., Zhang, L., Wei, S., Chen, S., Ou, X., & Lu, Q. (2014). Overoxidized polyimidazole/graphene oxide copolymer modified electrode for the simultaneous determination of ascorbic acid, dopamine, uric acid, guanine and adenine.

Biosens Bioelectron, 57, 232-238.

Ma, L., Zhang, Q., Wu, C., Zhang, Y., & Zeng, L. (2019). PtNi bimetallic nanoparticles loaded MoS2 nanosheets: Preparation and electrochemical sensing application for the detection of dopamine and uric acid. *Anal Chim Acta, 1055*, 17-25.

Martínez-Huitle, C. A., Cerro-Lopez, M., & Quiroz, M. A. (2009). Electrochemical behaviour of dopamine at covalent modified glassy carbon electrode with L-Cysteine: Preliminary results. *Mater. Res., 12*(4), 375-384.

Martinez, A. W., Phillips, S. T., Butte, M. J., & Whitesides, G. M. (2007). Patterned paper as a platform for inexpensive, low-volume, portable bioassays. *Angewandte Chemie - International Edition, 46*(8), 1318-1320.

Martinez, A. W., Phillips, S. T., & Whitesides, G. M. (2008). Three-dimensional microfluidic devices fabricated in layered paper and tape. *Proceedings of the National Academy of Sciences of the United States of America, 105*(50), 19606-19611.

Martinez, A. W., Phillips, S. T., Whitesides, G. M., & Carrilho, E. (2010). Diagnostics for the developing world: microfluidic paper-based analytical devices. *Anal Chem, 82*(1), 3-10.

Medina-Sanchez, M., Cadevall, M., Ros, J., & Merkoci, A. (2015). Eco-friendly electrochemical lab-on-paper for heavy metal detection. *Anal Bioanal Chem, 407*(28), 8445-8449.

Mina, M. J., Parker, R., & Larremore, D. B. (2020). Rethinking Covid-19 Test Sensitivity — A Strategy for Containment. *New England Journal of Medicine, 383*(22), e120-e120.

Nakthong, P., Kondo, T., Chailapakul, O., & Siangproh, W. (2020). Development of an unmodified screen-printed graphene electrode for nonenzymatic histamine detection. *Anal. Methods, 12*(44), 5407-5414.

Nantaphol, S., Channon, R. B., Kondo, T., Siangproh, W., Chailapakul, O., & Henry, C. S. (2017). Boron Doped Diamond Paste Electrodes for Microfluidic Paper-Based Analytical Devices. *Anal Chem, 89*(7), 4100-4107.

Nguyen, M. P., Meredith, N. A., Kelly, S. P., & Henry, C. S. (2018). Design considerations for reducing sample loss in microfluidic paper-based analytical devices. *Analytica*

Chimica Acta, 1017, 20-25.

Noviana, E., Carrão, D. B., Pratiwi, R., & Henry, C. S. (2020). Emerging applications of paper-based analytical devices for drug analysis: A review. In *Analytica Chimica Acta* (Vol. 1116, pp. 70-90): Elsevier B.V.

O'Connell, M. A., Belanger, B. A., & Haaland, P. D. (1993). Calibration and assay development using the four-parameter logistic model. *Chemometrics and Intelligent Laboratory Systems, 20*(2), 97-114.

Overview of ELISA. (8 July 2021). https://www.thermofisher.com/th/en/home/life-science/protein-biology/protein-biology-learning-center/protein-biology-resource-library/pierce-protein-methods/overview-elisa.html

Ozcan, A., Ilkbas, S., & Atilir Ozcan, A. (2017). Development of a disposable and low-cost electrochemical sensor for dopamine detection based on poly(pyrrole-3-carboxylic acid)-modified electrochemically over-oxidized pencil graphite electrode. *Talanta, 165*, 489-495.

Panraksa, Y., Siangproh, W., Khampieng, T., Chailapakul, O., & Apilux, A. (2018). Paper-based amperometric sensor for determination of acetylcholinesterase using screen-printed graphene electrode. *Talanta, 178*, 1017-1023.

Parrilla, M., Canovas, R., & Andrade, F. J. (2017). Paper-based enzymatic electrode with enhanced potentiometric response for monitoring glucose in biological fluids. *Biosens Bioelectron, 90*, 110-116.

Preechakasedkit, P., Siangproh, W., Khongchareonporn, N., Ngamrojanavanich, N., & Chailapakul, O. (2018). Development of an automated wax-printed paper-based lateral flow device for alpha-fetoprotein enzyme-linked immunosorbent assay. *Biosensors and Bioelectronics, 102*, 27-32.

Pungjunun, K., Chaiyo, S., Jantrahong, I., Nantaphol, S., Siangproh, W., & Chailapakul, O. (2018). Anodic stripping voltammetric determination of total arsenic using a gold nanoparticle-modified boron-doped diamond electrode on a paper-based device. *Mikrochim Acta, 185*(7), 324.

Pungjunun, K., Chaiyo, S., Praphairaksit, N., Siangproh, W., Ortner, A., Kalcher, K., . . .

Mehmeti, E. (2019). Electrochemical detection of NOx gas based on disposable paper-based analytical device using a copper nanoparticles-modified screen-printed graphene electrode. *Biosens Bioelectron, 143*, 111606-111606.

Punjiya, M., Moon, C. H., Matharu, Z., Rezaei Nejad, H., & Sonkusale, S. (2018). A three-dimensional electrochemical paper-based analytical device for low-cost diagnostics. *Analyst, 143*(5), 1059-1064.

Ramachandran, S., Fu, E., Lutz, B., & Yager, P. (2014). Long-term dry storage of an enzyme-based reagent system for ELISA in point-of-care devices. *Analyst, 139*(6), 1456-1462.

Rasheed, P. A., Pandey, R. P., Jabbar, K. A., Ponraj, J., & Mahmoud, K. A. (2019). Sensitive electrochemical detection of l-cysteine based on a highly stable Pd@Ti3C2T:X(MXene) nanocomposite modified glassy carbon electrode. *Anal. Methods, 11*(30), 3851-3856.

Rasmi, Y., Li, X., Khan, J., Ozer, T., & Choi, J. R. (2021). Emerging point-of-care biosensors for rapid diagnosis of COVID-19: current progress, challenges, and future prospects. *Analytical and Bioanalytical Chemistry, 413*(16), 4137-4159.

Rattanarat, P., Dungchai, W., Cate, D., Volckens, J., Chailapakul, O., & Henry, C. S. (2014). Multilayer paper-based device for colorimetric and electrochemical quantification of metals. *Anal Chem, 86*(7), 3555-3562.

Rattanarat, P., Dungchai, W., Siangproh, W., Chailapakul, O., & Henry, C. S. (2012). Sodium dodecyl sulfate-modified electrochemical paper-based analytical device for determination of dopamine levels in biological samples. *Anal Chim Acta, 744*, 1-7.

Reddaiah, K., Reddy, M. M., Raghu, P., & Reddy, T. M. (2013). An electrochemical sensor based on poly (solochrome dark blue) film coated electrode for the determination of dopamine and simultaneous separation in the presence of uric acid and ascorbic acid: a voltammetric method. *Colloids Surf B Biointerfaces, 106*, 145-150.

Renault, C., Li, X., Fosdick, S. E., & Crooks, R. M. (2013). Hollow-channel paper analytical devices. *Anal Chem, 85*(16), 7976-7979.

Reuben, B. (2009, 8 July 2021). Bread chemistry on the rise https://www.chemistryworld.com/features/bread-chemistry-on-the-rise/3004720.article

Sajid, M., Kawde, A. N., & Daud, M. (2015). Designs, formats and applications of lateral flow assay: A literature review. *Journal of Saudi Chemical Society, 19*(6), 689-705.

Samper, I. C., Sanchez-Cano, A., Khamcharoen, W., Jang, I., Siangproh, W., Baldrich, E., . . . Henry, C. S. (2021). Electrochemical Capillary-Flow Immunoassay for Detecting Anti-SARS-CoV-2 Nucleocapsid Protein Antibodies at the Point of Care. *ACS Sens, 6*(11), 4067-4075.

Sawka, A. M., Jaeschke, R., Singh, R. J., & Young, W. F. (2003). A comparison of biochemical tests for pheochromocytoma: Measurement of fractionated plasma metanephrines compared with the combination of 24-hour urinary metanephrines and catecholamines. *Journal of Clinical Endocrinology and Metabolism, 88*(2), 553-558.

Shiroma, L. Y., Santhiago, M., Gobbi, A. L., & Kubota, L. T. (2012). Separation and electrochemical detection of paracetamol and 4-aminophenol in a paper-based microfluidic device. *Anal Chim Acta, 725*, 44-50.

Singh, M., Jaiswal, N., Tiwari, I., Foster, C. W., & Banks, C. E. (2018). A reduced graphene oxide-cyclodextrin-platinum nanocomposite modified screen printed electrode for the detection of cysteine. *J. Electroanal. Chem., 829*, 230-240.

Sohouli, E., Ghalkhani, M., Rostami, M., Rahimi-Nasrabadi, M., & Ahmadi, F. (2020). A noble electrochemical sensor based on TiO2@CuO-N-rGO and poly (L-cysteine) nanocomposite applicable for trace analysis of flunitrazepam. *Mater. Sci. Eng. C, 117*, 111300-111300.

Su, X., Zhang, J., Zhang, D., Wang, Y., Chen, M., Weng, Z., . . . Xia, N. (2020). High-Efficiency Plasma Separator Based on Immunocapture and Filtration. *Micromachines 2020, Vol. 11, Page 352, 11*(4), 352-352.

Terry, J. S., Anderson, L. B. R., Scherman, M. S., McAlister, C. E., Perera, R., Schountz, T., & Geiss, B. J. (2021). Development of a SARS-CoV-2 nucleocapsid specific

monoclonal antibody. *Virology, 558*, 28-37.

Thomas, T., Mascarenhas, R. J., Oj, D. S., Detriche, S., Mekhalif, Z., & Martis, P. (2014). Pristine multi-walled carbon nanotubes/SDS modified carbon paste electrode as an amperometric sensor for epinephrine. *Talanta, 125*, 352-360.

Thota, R., & Ganesh, V. (2016). Simple and facile preparation of silver-polydopamine (Ag-PDA) core-shell nanoparticles for selective electrochemical detection of cysteine. *RSC Adv., 6*(55), 49578-49587.

Triarhou, L. C. (2013). Dopamine and Parkinson's Disease.

Tuaillon, E., Bolloré, K., Pisoni, A., Debiesse, S., Renault, C., Marie, S., . . . Van de Perre, P. (2020). Detection of SARS-CoV-2 antibodies using commercial assays and seroconversion patterns in hospitalized patients. *Journal of Infection, 81*(2), e39-e45.

Vogels, C. B. F., Brito, A. F., Wyllie, A. L., Fauver, J. R., Ott, I. M., Kalinich, C. C., . . . Grubaugh, N. D. (2020). Analytical sensitivity and efficiency comparisons of SARS-CoV-2 RT–qPCR primer–probe sets. *Nature Microbiology, 5*(10), 1299-1305.

Von Bargen, C., Dojahn, J., Waidelich, D., Humpf, H. U., & Brockmeyer, J. (2013). New sensitive high-performance liquid chromatography-tandem mass spectrometry method for the detection of horse and pork in halal beef. *Journal of Agricultural and Food Chemistry, 61*(49), 11986-11994.

Wang, C. C., Hennek, J. W., Ainla, A., Kumar, A. A., Lan, W. J., Im, J., . . . Whitesides, G. M. (2016). A Paper-Based Pop-up Electrochemical Device for Analysis of Beta-Hydroxybutyrate. *Analytical Chemistry, 88*(12), 6326-6333.

Wang, J. (2000). *Analytical electrochemistry* (2nd). New York: Wiley-VCH.

Wang, Y., Liu, G., Hou, X., Huang, Y., Li, C., & Wu, K. (2016). Assembling gold nanorods on a poly-cysteine modified glassy carbon electrode strongly enhance the electrochemical reponse to tetrabromobisphenol A. *Microchim. Acta, 183*(2), 689-696.

Wang, Z., Zheng, Z., Hu, H., Zhou, Q., Liu, W., Li, X., . . . Ma, Y. (2020). A point-of-care selenium nanoparticle-based test for the combined detection of anti-SARS-CoV-2

IgM and IgG in human serum and blood. *Lab on a Chip, 20*(22), 4255-4261.

Xu, L., Cai, C. B., Cui, H. F., Ye, Z. H., & Yu, X. P. (2012). Rapid discrimination of pork in Halal and non-Halal Chinese ham sausages by Fourier transform infrared (FTIR) spectroscopy and chemometrics. *Meat Science, 92*(4), 506-510.

Yin, H., Zhou, Y., Ma, Q., Ai, S., Ju, P., Zhu, L., & Lu, L. (2010). Electrochemical oxidation behavior of guanine and adenine on graphene–Nafion composite film modified glassy carbon electrode and the simultaneous determination. *PROCESS BIOCHEM, 45*(10), 1707-1712.

Yuan, Q., Liu, Y., Ye, C., Sun, H., Dai, D., Wei, Q., . . . Lin, C. T. (2018). Highly stable and regenerative graphene-diamond hybrid electrochemical biosensor for fouling target dopamine detection. *Biosens Bioelectron, 111*, 117-123.

Zhan, L., Wu, W. B., Yang, X. X., & Huang, C. Z. (2014). Gold nanoparticle-based enhanced ELISA for respiratory syncytial virus. *New Journal of Chemistry, 38*(7), 2935-2940.

Zhang, X., Yu, Y., Shen, J., Qi, W., & Wang, H. (2020). Design of organic/inorganic nanocomposites for ultrasensitive electrochemical detection of a cancer biomarker protein. *Talanta, 212*, 120794-120794.

Zhao, D., Yu, G., Tian, K., & Xu, C. (2016). A highly sensitive and stable electrochemical sensor for simultaneous detection towards ascorbic acid, dopamine, and uric acid based on the hierarchical nanoporous PtTi alloy. *Biosens Bioelectron, 82*, 119-126.

Appendix

Appendix 1

NJC

ROYAL SOCIETY OF CHEMISTRY

PAPER

Cite this: *New J. Chem.*, 2021, 45, 12886

A multilayer microfluidic paper coupled with an electrochemical platform developed for sample separation and detection of dopamine†

Wisarut Khamcharoen and Weena Siangproh *

Received 9th May 2021,
Accepted 16th June 2021

DOI: 10.1039/d1nj02271g

rsc.li/njc

One of the primary challenges for the development of electrochemical sensors for dopamine (DA) is the lack of selectivity due to the major interference from ascorbic acid (AA) which is oxidized at a potential close to the working potential of DA. In this work, we present a means for simple and cost-effective electrochemical detection of DA in the presence of interference using a microfluidic paper-based analytical device (eμPAD) to improve the selectivity and sensitivity. The device was made by incorporating the sample separation and the electrochemical detection elements into a single device, which required a single drop of the sample solution. For sample separation, Nafion was cast on the sample zone and microfluidic channel to block AA, before the solution was allowed to continuously flow to the detection zone. A multilayered eμPAD was fabricated by placing a round cotton pad on the detection zone to enable the generation of a quasi-steady flow rate. Thereafter, a packing tape was used to seal the top part of the device to increase the flow rate and prevent volatilization of the sample on the eμPAD. The concentration of DA that could be measured by the poly(glutamic acid) modified screen-printed graphene electrode was in the range of 1–200 μM, and the limit of detection (LOD) was 0.41 μM (3SD/slope). The proposed platform provides an accurate and satisfactory method for the detection of DA in real samples compared with UV-Vis spectroscopy.

1. Introduction

Over the past decade, the demand for simple and affordable medical diagnostic systems has rapidly increased. Point-of-care (POC) testing is a medical diagnostic testing that plays a significant role in facilitating a convenient platform for the end-users. It can be performed at bedside, thereby resulting in reduced time, complications, and cost for the detection of analytes.[1–3] Moreover, POC testing enables a comfortable diagnosis, routine monitoring, and effective management of diseases, which can help doctors diagnose diseases at an early stage.[4] As previously mentioned, this platform is going to offer a high beneficial impact on global health, particularly in developing countries. In numerous cases, POC testing was not successful, because several biomarkers related to human diseases are present at low concentrations and suffer from interference from other compounds in the biological samples.[5] Thus, the design and fabrication of a novel platform for successive separation and detection of the analyte using a simple POC system is extremely challenging.

For decades, the microfluidic paper-based analytical device (μPAD) has been used for analytical methods. The incredible properties of the μPAD resulted in significant revolution in the field of analytical chemistry. This is an excellent and challenging route to create a new alternative platform for POC applications. The μPAD has been reported to have diverse advantages in the enhancement of the performance of analytical methods, which leads to high efficiency. Nowadays, the μPAD fabricated from paper is widely used in analytical experiments. It has several advantages, such as cost-effectiveness, ease of use, portability, ease of elimination, and use of a small amount of sample reagent, leading to generation of reduced waste from the analysis as well. Furthermore, the solution is driven in the μPAD by capillary action, without the use of an external pump.[6,7] Owing to these benefits, the μPAD is considered as an innovative platform for equipment free testing and is used as a smart sensing device for numerous kinds of applications, including environmental monitoring,[8,9] food safety,[10,11] and clinical applications.[12–15] For detection, the integration of the μPAD with electrochemical detection has attracted considerable attention in this decade owing to its several advantages, such as high sensitivity and selectivity, in comparison with

Department of Chemistry, Faculty of Science, Srinakharinwirot University, Sukhumvit 23, Wattana, Bangkok 10110, Thailand. E-mail: weena@g.swu.ac.th, weenasi@hotmail.com

† Electronic supplementary information (ESI) available. See DOI: 10.1039/d1nj02271g

other detection methods. Moreover, an electrochemical μPAD (eμPAD) can be easily designed to have other functions, such as sample separation,[16] preconcentration,[17] preparation,[18] and washing.[19] It can also be coupled with colorimetry to enable dual mode of detection.[20] In terms of sample preparation, the capability of the eμPAD allows multiple steps of sample preparation to be incorporated into a single device.[21] This benefit leads to reduced steps for experimental testing as well as prevents loss of samples during the analysis; thus, it is suited for ideal POC devices. Generally, the use of a traditional eμPAD leads to a poor electrochemical response. This is due to the effect of slow flow rate and noncontinuous flow on devices, during the transport of the sample solution to the detection zone by capillary action.[22] Thus, a new design of the eμPAD platform is proposed to improve the efficiency of electrochemical response obtained from the target analyte.

Dopamine (DA) is one of the most important catecholamine neurotransmitters found in the central nervous system. It plays a significant role in the metabolism and functions of the cardiovascular, renal, and endocrine systems.[23] As a result, deficiency in the levels of DA is associated with various diseases,[24–26] particularly Parkinson's disease.[27] Therefore, a simple and sensitive analytical method for the detection and/or monitoring of the level of DA in human fluid samples is important. Over the years, the electrochemical technique has been an attractive analytical method owing to its excellent performance and advantages, such as fast analysis, high sensitivity, low cost, and simple instrumentation. However, significant problems in the electroanalysis of DA are often associated with the presence of ascorbic acid (AA) in real samples, since DA and AA are oxidized at nearly the same potential. Moreover, traditional electrodes also demonstrate slow electron transfer and poor electrocatalytic properties for the direct oxidation of DA. This leads to poor selectivity and sensitivity for the detection of DA in sample matrices.[28] The key strategy to solve the AA interference problem and also enhance sensitivity for DA detection is the use of electrodes modified with numerous materials. The goals are to reduce the over-potential of AA far away from the DA peak, and/or prevent AA transport to the electrode surface.[29] Examples of modifiers include overoxidized polyimidazole/graphene oxide copolymer,[30] graphene anchored with Pd–Pt nanoparticles,[31] phenylethynyl ferrocene/graphene nanocomposite,[32] and polydopamine/reduced graphene oxide.[33] These proposed materials provide a good LOD and can be used for the detection of DA in the presence of AA. However, these modified electrodes require expensive materials and several steps for electrode modification, which is a time-consuming process, making it increasingly difficult for the end users. In addition, the electrodes modified with these complicated materials could be influenced by low reproducibility of the method. Thus, a simple electroanalytical method that can overcome these limitations is required.

To simplify the detection of DA even further, a multilayer eμPAD has been designed and fabricated by integrating the sample separation and electrochemical detection elements into a single device. The selectivity was achieved by using a Nafion membrane, since the inside of the Nafion nanoporous structure contains negatively charged sulfonic groups, which strongly repulse anionic molecules away from the membrane.[34,35] Therefore, Nafion was deposited on a microfluidic paper-based channel to block AA from the sample to obtain sample separation before the solution directly flows to the detection area. For the electrochemical measurement, poly(glutamic acid) (PGA) was used as a modifier on the surface of the screen-printed graphene electrode (SPGE) to enhance the electrochemical response of DA. Moreover, a multilayered eμPAD was also designed and fabricated to overcome the limitations of the previous platforms. To the best of our knowledge, this is the first report of the use of a single eμPAD for successive sample separation, without the requirement of external separation prior to analysis, and electrochemical detection of DA. A single drop of the sample solution is sufficient to completely perform the assay; therefore, only a minimal volume of the solution is needed. The proposed device was then applied for the detection of DA in artificial urine samples. The proposed device is disposable and cost effective as well as exhibits high sensitivity and selectivity for the detection of DA in the presence of AA while maintaining simplicity.

2. Experimental

2.1. Chemicals, materials, and apparatus

All chemicals used in this work were of analytical grade and used without any purification. DA, AA, uric acid, Nafion, l-glutamic acid, bovine serum albumin (BSA), potassium ferricyanide [$K_3Fe(CN)_6$], sodium chloride (NaCl), calcium chloride ($CaCl_2$), and vitamins B_2 and B_6 were purchased from Sigma-Aldrich (St. Louis, MO, USA). Glucose was obtained from Merck (Darmstadt, Germany). The artificial urine sample was purchased from Carolina Biological Supply Company (Burlington, USA). Phosphate buffer solution (PBS) (0.1 M), used as the supporting electrolyte, was prepared using sodium dihydrogen orthophosphate ($NaH_2PO_4{\cdot}2H_2O$) and disodium hydrogen orthophosphate ($Na_2HPO_4{\cdot}2H_2O$), which were obtained from Ajax (Australia). N-Propanol was purchased from Unilab (Mumbai, India). All aqueous solutions were prepared in deionized (DI) water.

Electrochemical techniques, such as cyclic voltammetry (CV) and differential pulse voltammetry (DPV), were performed using a CHI1200C potentiostat (Austin, TX, USA). Electrochemical impedance spectroscopy (EIS) was employed to confirm the successful modification of the electrodes using PalmSens4 (Houten, The Netherlands). Graphene and silver/silver chloride (Ag/AgCl) inks were purchased from Sun Chemical (Slough, United Kingdom). The screen-printed blocks were generated by Chaiyaboon Co. Ltd (Bangkok, Thailand). The eμPAD pattern was fabricated using a Xerox Color Qube 8570 series wax printing machine (Xerox, Japan). The Silcot cotton pad was purchased from Unicharm Products Co., Ltd (Tokyo, Japan), and the packing tape was purchased from 3M Thailand Company (Bangkok, Thailand).

2.2. Design and preparation of the eμPAD

The eμPAD pattern was designed using Adobe illustrator CC. Thereafter, the wax pattern was printed on the Whatman

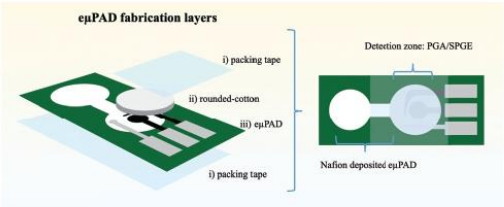

Fig. 1 Illustration of eμPAD layers, fabricated from (i) packing tape, (ii) round cotton pad and (iii) eμPAD layer.

Grade 1 filter paper using a wax printing machine. Subsequently, the wax-printed paper was placed on a hot plate at a temperature of 175 °C for 30 s, for melting the wax into the cellulosic structure of the paper to differentiate between the hydrophobic and hydrophilic areas. For the electrochemical detection zone, three electrodes, namely, working, reference, and counter electrodes, were screened by in-house screen printing. First, the graphene ink was screened on the detection zone, as shown in Fig. S1a (ESI†), to obtain the working and counter electrodes and placed in the oven at a temperature of 55 °C for 30 min. Subsequently, the Ag/AgCl ink was screened on the detection zone to complete the electrochemical cell, as shown in Fig. S1a (ESI†), and placed in the oven at a temperature of 55 °C for 30 min. Fig. S1b (ESI†) illustrates the μPAD coupled with electrochemical detection consisting of the sample zone (cycle, diameter = 10 mm), electrochemical detection zone (cycle, diameter = 12 mm), and microfluidic channel that is connected between the previously mentioned zones (channel, 3 mm × 5 mm).

2.3. Components of the eμPAD

The eμPAD has four layers (Fig. 1); (i) the two layers of packing tape, which were used to seal the top and bottom parts of the device to increase the flow rate and to prevent leakage and volatilization of the sample solution; (ii) a round cotton pad (circle, diameter = 10 mm), which was placed on the electrochemical detection zone to generate a quasi-steady flow rate on the device for the whole experiment; and (iii) the eμPAD layer, in which PGA was modified on the SPGE and 0.5% Nafion was drop-cast on the sample zone and microfluidic channel.

2.4. Operation of the eμPAD and procedure for electrochemical detection of DA

For operation, the bottom part of the eμPAD was sealed using a packing tape (Fig. 2a). The surface of the SPGE was modified with PGA by electropolymerization of 20 mM glutamic acid in 0.1 M PBS (pH 7.4); thereafter, 100 μL of the modifier was dropped on the detection zone and the potential was applied from −0.5 to +1.6 V using CV with a scan rate of 0.1 V s^{-1} for 7 cycles (Fig. 2b). The eμPAD was rinsed with DI water and dried at room temperature. Thereafter, 0.5% Nafion was prepared in n-propanol, and 10 μL of the solution was drop-cast on the sample zone and microfluidic channel (Fig. 2c) and dried at room temperature. Finally, the round cotton pad was placed on the electrochemical detection zone, and the top part of the device was sealed with a packing tape (Fig. 2d).

For the detection of DA, 60 μL of the DA solution in 0.1 M PBS (pH = 7.4) was dropped on the sample zone and was allowed to stand for 15 min (Fig. 2e). In this step, the solution flowed from the sample zone through the microfluidic channel to the electrochemical detection zone by capillary force. Subsequently, electrochemical detection was conducted by DPV using PGA/SPGE as the working electrode, Ag/AgCl as the reference electrode, and SPGE as the counter electrode. The parameters for the DPV measurement were as follows—an increment of 0.006 V, a pulse amplitude of 0.2 V, a pulse width of 0.1 s, and a pulse period of 0.6 s, with the potential varied from −0.4 to +0.4 V *versus* Ag/AgCl. The differential pulse voltammogram of DA is shown in Fig. 2f.

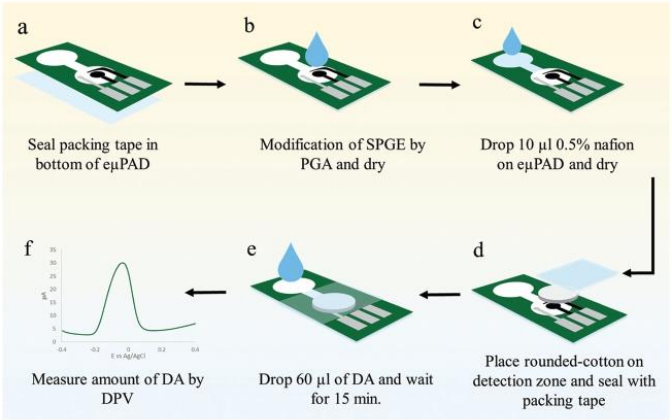

Fig. 2 The representation of the eμPAD for DA detection consisting of (a) sealed packing tape at the bottom of the eμPAD, (b) PGA modified SPGE step, (c) drop casting of 0.5% Nafion, (d) completed multilayer eμPAD components, (e) determination of the DA step and (f) differential pulse voltammogram of DA.

2.5. Determination of DA in real samples

To demonstrate the capability of the proposed eμPAD, it was evaluated for the detection of DA in artificial urine samples. The samples were diluted in PBS (pH 7.4), Thereafter, DA was spiked into the samples at concentrations of 10, 20, 40, 60, and 80 μM. The quantity of DA was measured using the eμPAD; the recovery of spiked standard DA was thoroughly studied. To confirm the accuracy of this device, the results obtained from the eμPAD were compared with those obtained using UV-Vis spectroscopy.[36]

3. Results and discussion

3.1. Characterization of the modified electrode

The PGA film modified SPGE was prepared by electropolymerization of 20 mM glutamic acid in 0.1 M PBS (pH 7.4) using CV. The potential was varied from −0.5 to +1.6 V *versus* Ag/AgCl at a scan rate of 100 mV s^{-1} for 7 cycles. The cyclic voltammogram obtained during electropolymerization is shown in Fig. 3a. From the figure, a well-defined peak current around +1.49 V can be observed during the first 3 cycles. After the fourth cycle, the broad peak current gradually increased with the increase in the number of scans. This indicated the growth and subsequent formation of the polymer film on the surface of the SPGE.[37]

The electrochemical behaviors of the unmodified SPGE and PGA/SPGE were compared and investigated using the techniques of CV and ESL† First, cyclic voltammograms of 5 mM $[Fe(CN)_6]^{3-/4-}$ in 0.1 M PBS (pH 7.4) were recorded using different electrodes in the potential range from −0.8 to +1.0 V. The redox peaks of $[Fe(CN)_6]^{3-/4-}$ are shown in Fig. 3b. It was observed that the electrochemical signal of 5 mM $[Fe(CN)_6]^{3-/4-}$ obtained using the PGA/SPGE increased approximately two-fold when compared with that obtained from the unmodified SPGE. This implies that the PGA/SPGE can be a candidate for detection of low concentrations of DA.

To explain the previously obtained results, the Randles–Sevcik equation (eqn (1)) was used to calculate the electroactive surface areas of the PGA/SPGE and unmodified SPGE. In the equation, i_p denotes the peak current; n, the number of electrons; F, Faraday's constant; A, the electroactive surface area; C_0^*, the concentration of the analyte ($[Fe(CN)_6]^{3-/4-}$); v, the scan rate; D_0, the diffusion coefficient of $[Fe(CN)_6]^{3-/4-}$; R, the ideal gas constant; and T, the temperature. Based on the known parameters from a previous study ($n = 1$, $C_0^* = 5 \times 10^{-6}$ mol cm^{-3}, v = 100 mV s^{-1}, $D_0 = 7.6 \times 10^{-6}$, R = 8.13447 J K^{-1} mol^{-1} and T = 298 K),[38] the electroactive surface areas were calculated.

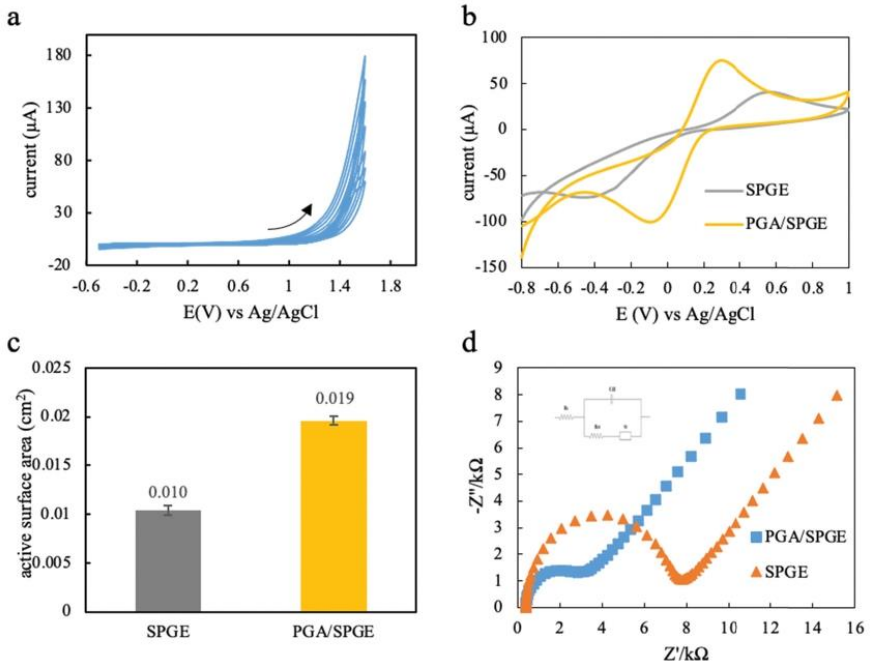

Fig. 3 (a) The electropolymerization of 20 mM glutamic acid onto SPGE surface was performed using CV scanned between −0.5 V and +1.6 V, at a scan rate of 100 mV s^{-1} for 7 cycles. (b) Cyclic voltammograms of 5 mM $[Fe(CN)_6]^{3-/4-}$ in 0.1 M PBS pH 7.4 at SPGE (gray line) and PGA/SPGE (yellow line), at a scan rate of 100 mV s^{-1}. (c) Electroactive surface areas of the SPGE (grey bar) and PGA/SPGE (yellow bar). (d) Nyquist plots of the SPGE and PGA/SPGE obtained from 5 mM $[Fe(CN)_6]^{3-/4-}$ at SPGE (orange) and PGA/SPGE (blue), respectively.

A comparison of the electroactive surface areas is shown in Fig. 3c. The PGA/SPGE provided a higher electroactive surface area than the unmodified SPGE. In addition, the value of peak separation (ΔE_p) decreased from +0.950 V, obtained for the unmodified SPGE, to +0.361 V, obtained for the PGA/SPGE, indicating that the rate of electron transfer can be increased after the electropolymerization of PGA on the surface of the SPGE.[37]

$$i_p = 0.45nFAC_0^*\sqrt{\frac{nF\nu D_0}{RT}} \quad (1)$$

Next, EIS was used to confirm the successful modification of the proposed electrode by investigating the electron transfer resistance (R_{ct}) for the redox couple of $[Fe(CN)_6]^{3-/4-}$ at the electrode surface. EIS was selected as the characterization technique, owing to its simplicity, surface sensitivity, and fast response. The results of EIS are presented using Nyquist plots. The Nyquist plots of both unmodified SPGE and PGA/SPGE were obtained using 5 mM $[Fe(CN)_6]^{3-/4-}$ in 0.1 M PBS (pH 7.4) (Fig. 3d). Each point of the Nyquist plot refers to the impedance corresponding to a specific frequency, as it is scanned from high to low frequency. The diameter of the semicircle is equal to the charge transfer resistance (R_{ct}) at the interface of the electrode and solution.[39] The values of R_{ct} of $[Fe(CN)_6]^{3-/4-}$ at the unmodified SPGE and PGA/SPGE were calculated to be 6.8 and 2.3 kΩ, respectively. The value of R_{ct} significantly decreased after electropolymerization of PGA on the surface of the SPGE. These results confirmed that the surface of the SPGE was successfully modified with PGA.

3.2. Electrochemical behavior of DA at the PGA/SPGE

The electrochemical property of DA was investigated by CV and DPV, using the unmodified SPGE and PGA/SPGE. CV was performed to study the electrochemical behavior of DA with different materials of the working electrode. Fig. 4a presents the comparison of cyclic voltammograms of DA using the unmodified SPGE (blue line) and PGA/SPGE (orange line). At the unmodified SPGE, the anodic and cathodic peaks were recorded at +0.3 and −0.15 V, respectively. Interestingly, the PGA/SPGE provided a higher current of the anodic and cathodic peaks and shifted to a negative direction, recorded at +0.089 and −0.083 V, respectively. Moreover, DPV was employed to validate the better performance of the PGA/SPGE compared with the unmodified SPGE, as shown in Fig. 4b. At the unmodified SPGE (blue line), the broad oxidation peak of DA was observed at +0.01 V, and the oxidation current obtained was 6.096 μA. In contrast, the PGA/SPGE (orange line) provided a well-defined peak and shifted to a negative direction, with the peak potential at −0.07 V. In addition, there was a significant enhancement (two-fold) of the peak current for DA compared with the unmodified SPGE. Therefore, the results obtained using CV and DPV strongly suggest that the PGA/SPGE exhibited electrocatalytic activity toward the direct oxidation of DA. These results indicated that the PGA/SPGE is an excellent electrode for detection of DA.

To achieve the best electrochemical response for detection of DA, the critical parameters for the electropolymerization of PGA include the concentration of monomer glutamic acid and

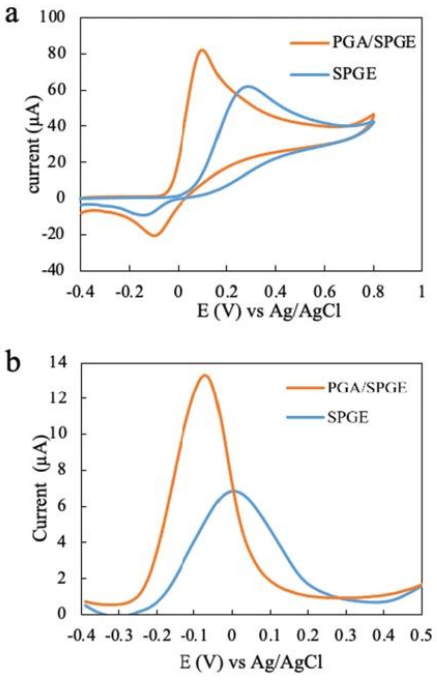

Fig. 4 Cyclic voltammograms (a) and differential pulse voltammograms (b) of DA at SPGE (blue line) and PGA/SPGE (orange line) in PBS pH 7.4.

the number of scans used in CV. These two parameters are involved in controlling the thickness of the polymer on the electrode surface. First, the concentration of glutamic acid was investigated in the range of 10–50 mM (Fig. S2, ESI†). At 20 mM, glutamic acid provided the highest oxidation current of DA. Beyond 20 mM, the oxidation current of DA gradually decreased, which may influence the thickness of the film of PGA on the SPGE surface, which is too thick, leading to low electron transfer at the interface between the electrode and electrolyte. Therefore, 20 mM glutamic acid was an optimal condition. Second, the number of scans in CV was varied in the range of 3–15 cycles (Fig. S3, ESI†). As can be seen from the figure, the oxidation currents of DA gradually increased as the number of scans increased from 5 to 7 cycles. The oxidation currents were relatively stable after 7 cycles. Thus, the number of scans was fixed to 7 cycles.

3.3. Comparison of the design and configuration of devices

To confirm the capability of the eμPAD for successive sample separation and detection using only a single drop of the sample solution, stagnant electrochemical analysis (Fig. S4, ESI†) was conducted by dropping 100 μL of the mixture of DA and AA on the PGA/SPGE. In addition, the electrochemical measurement was performed by DPV. Fig. 5a shows the individual differential pulse voltammograms of 100 μM DA and 100 μM AA in PBS (pH 7.4). The oxidation peaks of the two substances appear

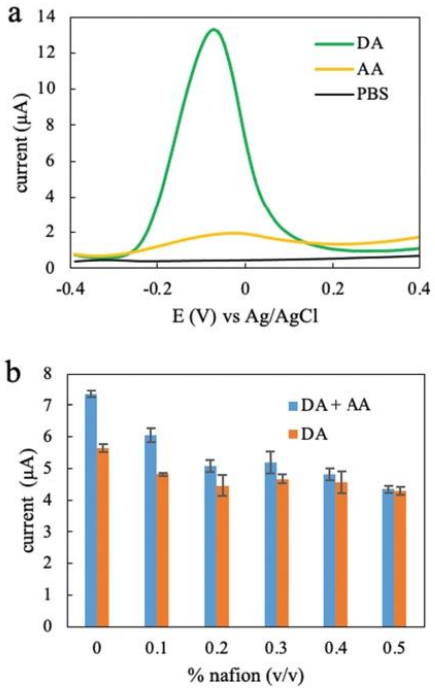

Fig. 5 (a) Differential pulse voltammogram of 100 μM DA (green line), 100 μM AA (orange line), and PBS pH 7.4 (black line) at PGA/SPGE performed by stagnant analysis. (b) The oxidation current value of 100 μM DA (blue bar) and 100 μM DA in the presence of 100 μM AA (orange bar) obtained with different concentrations of Nafion coated on the eμPAD channel.

approximately at the same potential. Hence, distinguished peaks for DA and AA are extremely difficult to observe. Therefore, AA is considered as a major electrochemical interference for the detection of DA at the PGA/SPGE using stagnant electrochemical analysis.

To overcome the AA interference problem which was confirmed from the results of stagnant electrochemical analysis, Nafion coating onto the eμPAD was suggested for the detection of DA in the presence of AA. As we know, Nafion has been widely used in biosensor applications[40,41] owing to its structure that shows a highly permeable membrane, which allows only cations to pass through the membrane while strongly repelling anions away from the electrode surface. Based on this property, Nafion was used in this work for coating the eμPAD channel to block AA (anion) while allowing the DA in the solution to flow to the electrochemical detection zone and thereby be measured by the electrochemical technique. The influence of different concentrations of Nafion to block AA was first investigated. Fig. 5b shows the oxidation current of 100 μM DA (orange bar) and 100 μM DA in the presence of 100 μM AA (blue bar) obtained with different concentrations of Nafion coated on the eμPAD channel. As can be seen from the figure, the difference in the oxidation current of 100 μM DA and 100 μM DA in the presence of 100 μM AA considerably decreased with the increase in Nafion concentration. Up to 0.5% Nafion, the values of oxidation current for both are approximately equal. These results indicated that 0.5% Nafion can completely block 100 μM AA, while measuring the concentration of DA. Moreover, to the best of our knowledge, the maximum concentration of AA in real samples is 80 μM.[28] Hence, 0.5% (v/v) Nafion was selected as an optimal condition for coating the eμPAD channel.

The pH effect was determined based on the use of Nafion as a material for the AA elimination strategy since Nafion has been proven to block anionic molecule transport but allow only cationic molecule transport. Therefore, the pH working condition was fixed in the range where DA exhibits positive charge while AA shows negative charge. To obtain this expected behavior, their pK_a values were considered. The pK_a value of DA at the amine group is 8.89 and the pK_a value of AA at the hydroxyl group is 4.10.[42] Thus, pH 7.4 is the most suitable condition for obtaining cationic DA and anionic AA as well as for applying this device to determine DA in biological samples.

3.4. Improvement of the electrochemical response for the detection of DA using the eμPAD

Based on the results obtained from the eμPAD, the value of oxidation current for the detection of DA was very low due to two primary factors. The first factor is the Nafion coated onto the sample zone and microfluidic channel. Owing to the structure of Nafion, which contains perfluoroalkyl backbones, it has strong hydrophobic properties.[43] Hence, after coating Nafion onto the eμPAD, Nafion can penetrate into the pores of the paper, obstructing the flow of the solution in the microfluidic channel resulting in a slow flow rate and leading to low mass transport of DA from the bulk solution to the electrode interface. Moreover, due to the slow flow rate, the measurement requires a significant amount of time. The second factor is the flow rate on the eμPAD after the solution completely migrates to the dry region of the hydrophilic area, which leads to a decay in the flow rate; thereafter, the flow rate decreases with time. This phenomenon also causes a low mass transport at the electrode interface.[6] As previously mentioned, a multilayered eμPAD was designed and employed to overcome these disadvantages. In a previous work, a sealing method with the use of a packing tape was proposed. Sealing the top part of the μPAD using a packing tape can increase the flow rate by over two-fold, which is contrary to that observed with the open μPAD.[22] From this idea a packing tape was used as a sealing material to increase the flow rate of the eμPAD. As shown in Fig. 6, we have designed and fabricated four different platforms. The first platform is the open eμPAD that is used for comparison. It can be observed that the use of the second platform (Fig. 6b), which was sealed on the top using a packing tape, slightly increased the oxidation current corresponding to 100 μM DA, when compared with the open eμPAD (first platform). However, the obtained response is not highly sensitive enough for detection of DA in biological samples. From the literature, we found that the use of an

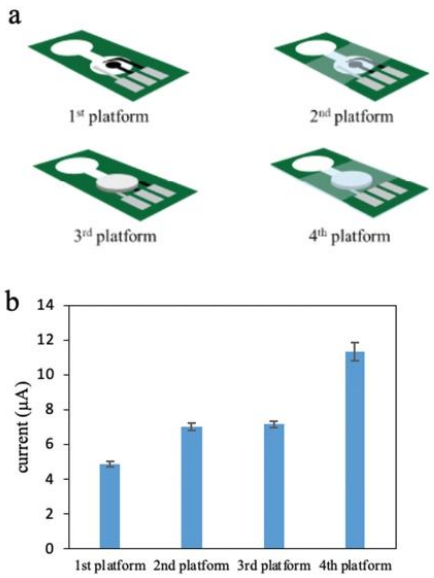

Fig. 6 (a) The schematic representation of the design and fabrication of the eμPAD in different platforms. (b) The effect of different eμPAD platforms on the oxidation current for DA detection.

absorbent pad can overcome the decay in flow rate with time, because the absorbent pad is used to absorb the solution from the sample zone through a porous structure and continuously enable capillary flow (quasi-steady flow with time) on the eμPAD.[44] Therefore, in this work, we used a round cotton pad instead of the absorbent pad. This is because the round cotton pad exhibits high porosity similar to the absorbent pad but has a lower cost. It was placed on top of the detection zone (third platform) to enable a quasi-steady flow. However, the oxidation current obtained from the third platform was also slightly increased when compared with the open eμPAD (first platform), and no difference was observed from the second platform. Therefore, it is impossible to detect DA in a real sample with this platform as well. We have attempted to use the round cotton pad and the packing tape to create a novel device called a multilayered eμPAD. Our design was first fabricated as shown in the fourth platform (Fig. 6). From the figure, it can be clearly seen that the multilayered eμPAD (fourth platform) provided the highest electrochemical response and high sensitivity for the detection of DA. We strongly believe that the excellent results obtained from the use of the packing tape and the round cotton pad enabled a high flow rate and generated more complete mass transport of DA to the electrode interface.

After achieving the optimal design, we evaluated the effect of the waiting time before performing the electrochemical measurement, as it also had a significant effect on the electrochemical response. The effect of different waiting times of 10, 15, and 20 min was investigated using the multilayered eμPAD. The oxidation current obtained from the different waiting times is shown in Fig. S5 (ESI†). By increasing the waiting time, the oxidation current considerably increased as expected. However, we observed that the oxidation currents obtained between 15 and 20 min did not significantly differ. Accordingly, a waiting time of 15 min was selected as the optimal waiting time for subsequent measurements.

3.5. Analytical performance

The analytical performance of the multilayered eμPAD for detection of DA was evaluated, and several concentrations of DA were determined using DPV. Fig. 7a shows the differential pulse voltammogram at various concentrations of DA using the multilayered eμPAD. The oxidation peak currents of DA gradually increased with increasing concentrations. The linear calibration plot between the oxidation current and the concentration of DA was obtained over the range of 1–200 μM. A linear regression equation of $i_{pa} = 0.1987C_{DA} + 1.1301$ with a correlation coefficient of $R^2 = 0.9994$ (Fig. 7b) was obtained. The LOD (LOD = $3SD_{blank}$/slope) was found to be 0.41 μM. Moreover, the analytical performance of the proposed multilayered eμPAD was compared with that in the previous reports, and the results are summarized in Table S1 (ESI†). Although the LOD in some previous reports was

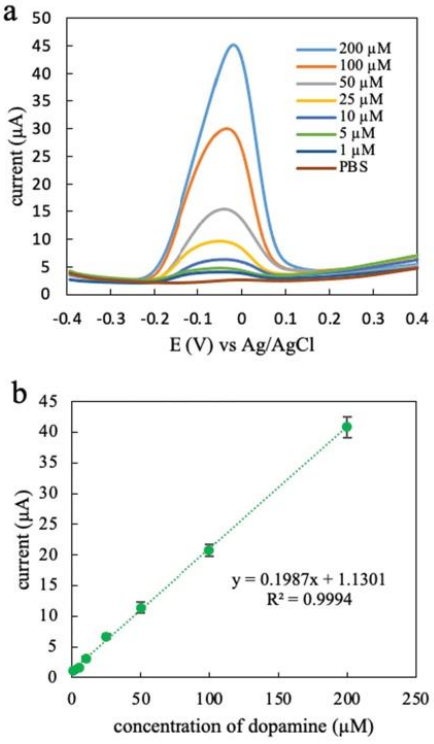

Fig. 7 (a) Differential pulse voltammograms obtained from several concentrations of DA in PBS pH 7.4 using the multilayer eμPAD, (b) calibration plot between concentration of DA (μM) and current (μA).

Table 1 The analytical application using a novel multilayer eμPAD for the detection of DA in artificial urine samples (n = 3)

Sample	Spiked (μM)	Found (μM)	Recovery (%)	RSD (%)
Artificial urine	10	10.8 ± 0.3	108.3	2.3
	20	20.2 ± 0.7	101.0	3.6
	40	38.6 ± 1.9	96.6	5.0
	60	59.2 ± 1.7	98.7	2.8
	80	81.1 ± 1.1	101.4	1.4

lower compared to that of the proposed platform, those methods required several steps for modification of the electrodes and used expensive materials. On the other hand, the proposed platform only involved a single step for dropping the sample solution onto the sample zone and allowed sample separation before analysis. Thereafter, the sample was allowed to successively penetrate into the sample separation and detection zones using a single device. This innovative device can be widely used in a variety of applications owing to its advantages, such as simplicity, fast response, and the ability to perform sample separation. Another important point is that coating Nafion on the channel is more convenient and takes less time than the direct modification onto the electrode surface. Thus, the design presented here can be easily fabricated and extended to a range of complex assays with favorable preferences of a cost-effective and effortless platform, thereby facilitating its generic use.

3.6. Selectivity

Apart from the interference from AA, other common interferences that were observed in urine samples include uric acid, glucose, vitamin B, BSA, Na^+, and Ca^{2+}. As shown in Fig. S6 (ESI†), the oxidation current of 100 μM DA in the presence of 100 μM uric acid, 1 mM glucose, 100 μM vitamins B_2 and B_6, 1000 μg L^{-1} BSA, 1 mM Na^+, and 1 mM Ca^{2+} does not interfere (change in signal was below 5%). These results indicated that the proposed multilayered eμPAD offers excellent selectivity for the detection of DA.

3.7. Analytical application

The practicality of the proposed device was demonstrated by the detection of DA in artificial urine samples. The recovery test was conducted by increasing the specified concentrations (10, 20, 40, 60, and 80 μM) of DA using the standard addition method. As shown in Table 1, percentage recovery and relative standard deviation with three different devices were observed in the range of 96.6–108.3% and 1.4–5.0%, respectively. Finally, the results obtained with the proposed device were compared with those obtained using UV-Vis spectroscopy.[36] The paired t-test at 95% confidence interval was evaluated; the calculated paired two-tailed value (0.13) of DA was below the critical t value (2.78). These results indicated that the proposed device is acceptable and reliable for the detection of DA in urine samples.

4. Conclusion

Successive sample separation and detection utilizing only a single drop of the sample solution with a multilayered eμPAD were successfully proposed for detection of DA. In this work, Nafion coated on the eμPAD channel was used to block AA that should not flow to the electrochemical detection zone. The PGA/SPGE was used as the working electrode and it exhibited excellent sensitivity to quantify the concentration of DA in urine samples by DPV. In addition, this newly designed and fabricated multilayered eμPAD platform increases the electrochemical response for detection of DA, which can be applied for detection in real samples. A packing tape and a round cotton pad were used to maintain a high and quasi-steady flow rate to the device. Finally, to demonstrate the capability of the device, the multilayered eμPAD was successfully applied for the detection of DA in artificial urine samples. This platform exhibits excellent advantages compared with those in the previous reports, such as low cost, simple steps for fabrication, reduced steps for electrode preparation, disposability, portability, and short analysis time. Consequently, this multilayered eμPAD, in which sample separation and detection were integrated into a single device, serves as an alternative electrochemical detection platform for POC diagnostic systems to detect other important biomarkers in the future.

Author contributions

Wisarut Khamcharoen: conceptualization, methodology, validation, writing – original draft. Weena Siangproh: resources, funding acquisition, project administration, supervision, writing – reviewing and editing.

Conflicts of interest

There are no conflicts to declare.

Acknowledgements

WK would like to thank the Science Achievement Scholarship of Thailand (SAST) and Srinakharinwirot University. WS would like to acknowledge the financial support from the National Research Council of Thailand (NRCT) and Srinakharinwirot University through Research Grants for Talented Mid-Career Researchers.

References

1 H. A. Joung, Z. S. Ballard, A. Ma, D. K. Tseng, H. Teshome, S. Burakowski, O. B. Garner, D. di Carlo and A. Ozcan, *Lab Chip*, 2019, **19**, 1027–1034.
2 F. Li, M. You, S. Li, J. Hu, C. Liu, Y. Gong, H. Yang and F. Xu, *Biotechnol. Adv.*, 2020, **39**, 107442.
3 T. Songjaroen, V. Primpray, T. Manosarn, W. Khumchanta, T. Sakuldamrongpanich, S. Kulkeratiyut and W. Laiwattanapaisal, *J. Immunoassay Immunochem.*, 2018, **39**, 292–307.
4 S. K. Vashist, *Biosensors*, 2017, **7**, 62.

5 W. Suntornsuk and L. Suntornsuk, *Electrophoresis*, 2020, **41**, 287–305.
6 J. A. Adkins, E. Noviana and C. S. Henry, *Anal. Chem.*, 2016, **88**, 10639–10647.
7 E. Carrilho, A. W. Martinez and G. M. Whitesides, *Anal. Chem.*, 2009, **81**, 7091–7095.
8 K. Ogawa and T. Kaneta, *Anal. Sci.*, 2016, **32**, 31–34.
9 M. P. Nguyen, S. P. Kelly, J. B. Wydallis and C. S. Henry, *Anal. Chim. Acta*, 2020, **1100**, 156–162.
10 Y. Zhao, D. Zeng, C. Yan, W. Chen, J. Ren, Y. Jiang, L. Jiang, F. Xue, D. Ji, F. Tang, M. Zhou and J. Dai, *Analyst*, 2020, **145**, 3106–3115.
11 E. Trofimchuk, Y. Hu, A. Nilghaz, M. Z. Hua, S. Sun and X. Lu, *Food Chem.*, 2020, **316**, 126396.
12 W. Tan, L. Zhang, J. C. G. Doery and W. Shen, *Lab Chip*, 2020, **20**, 394–404.
13 W. Y. Lim, C. H. Goh, T. M. Thevarajah, B. T. Goh and S. M. Khor, *Biosens. Bioelectron.*, 2020, **147**, 111792.
14 E. L. Rossini, M. I. Milani, E. Carrilho, L. Pezza and H. R. Pezza, *Anal. Chim. Acta*, 2018, **997**, 16–23.
15 C. T. Kokkinos, D. L. Giokas, A. S. Economou, P. S. Petrou and S. E. Kakabakos, *Anal. Chem.*, 2018, **90**, 1092–1097.
16 L. Y. Shiroma, M. Santhiago, A. L. Gobbi and L. T. Kubota, *Anal. Chim. Acta*, 2012, **725**, 44–50.
17 S. Nantaphol, R. B. Channon, T. Kondo, W. Siangproh, O. Chailapakul and C. S. Henry, *Anal. Chem.*, 2017, **89**, 4100–4107.
18 S. H. Lee, J. H. Lee, V. K. Tran, E. Ko, C. H. Park, W. S. Chung and G. H. Seong, *Sens. Actuators, B*, 2016, **232**, 514–522.
19 S. Mohammadi, L. S. Busa, M. Maeki, R. M. Mohamadi, A. Ishida, H. Tani and M. Tokeshi, *Anal. Bioanal. Chem.*, 2016, **408**, 7559–7563.
20 P. Rattanarat, W. Dungchai, D. Cate, J. Volckens, O. Chailapakul and C. S. Henry, *Anal. Chem.*, 2014, **86**, 3555–3562.
21 S. Nantaphol, A. A. Kava, R. B. Channon, T. Kondo, W. Siangproh, O. Chailapakul and C. S. Henry, *Anal. Chim. Acta*, 2019, **1056**, 88–95.
22 R. B. Channon, M. P. Nguyen, A. G. Scorzelli, E. M. Henry, J. Volckens, D. S. Dandy and C. S. Henry, *Lab Chip*, 2018, **18**, 793–802.
23 S. Palanisamy, K. Shuhao and S. M. Chen, *Microchim. Acta*, 2013, **180**, 1037–1042.
24 K. L. Davis, R. S. Kahn, G. Ko and M. Davidson, *Am. J. Psychiatry*, 1991, **148**, 1474–1486.
25 L. Liu, Q. Li, N. Li, J. Ling, R. Liu, Y. Wang, L. Sun, X. H. Chen and K. Bi, *J. Sep. Sci.*, 2011, **34**, 1198–1204.
26 T. Puumala and J. Sirvio, *Neuroscience*, 1998, **83**, 489–499.
27 L. Studer, M. Psylla, B. Buhler, L. Evtouchenko, C. M. Vouga, K. L. Leenders, R. W. Seiler and C. Spenger, *Brain Res. Bull.*, 1996, **41**, 143–150.
28 P. Rattanarat, W. Dungchai, W. Siangproh, O. Chailapakul and C. S. Henry, *Anal. Chim. Acta*, 2012, **744**, 1–7.
29 T. Q. Xu, Q. L. Zhang, J. N. Zheng, Z. Y. Lv, J. Wei, A. J. Wang and J. J. Feng, *Electrochim. Acta*, 2014, **115**, 109–115.
30 X. Liu, L. Zhang, S. Wei, S. Chen, X. Ou and Q. Lu, *Biosens. Bioelectron.*, 2014, **57**, 232–238.
31 J. Yan, S. Liu, Z. Zhang, G. He, P. Zhou, H. Liang, L. Tian, X. Zhou and H. Jiang, *Colloids Surf., B*, 2013, **111**, 392–397.
32 M. Liu, L. Wang, J. Deng, Q. Chen, Y. Li, Y. Zhang, H. Li and S. Yao, *Analyst*, 2012, **137**, 4577–4583.
33 N. Huang, S. Zhang, L. Yang, M. Liu, H. Li, Y. Zhang and S. Yao, *ACS Appl. Mater. Interfaces*, 2015, **7**, 17935–17946.
34 E. Leppänen, A. Peltonen, J. Seitsonen, J. Koskinen and T. Laurila, *J. Electroanal. Chem.*, 2019, **843**, 12–21.
35 E. Mynttinen, N. Wester, T. Lilius, E. Kalso, B. Mikladal, I. Varjos, S. Sainio, H. Jiang, E. I. Kauppinen, J. Koskinen and T. Laurila, *Anal. Chem.*, 2020, **92**, 8218–8227.
36 L. Guo, Y. Zhang and Q. Li, *Anal. Sci.*, 2009, **25**, 1451–1455.
37 X. Liu, L. Luo, Y. Ding and D. Ye, *Bioelectrochemistry*, 2011, **82**, 38–45.
38 M. Punjiya, C. H. Moon, Z. Matharu, H. Rezaei Nejad and S. Sonkusale, *Analyst*, 2018, **143**, 1059–1064.
39 A. Ozcan, S. Ilkbas and A. Atilir Ozcan, *Talanta*, 2017, **165**, 489–495.
40 A. Babaei and A. R. Taheri, *Sens. Actuators, B*, 2013, **176**, 543–551.
41 M. Parrilla, R. Canovas and F. J. Andrade, *Biosens. Bioelectron.*, 2017, **90**, 110–116.
42 M. Cheng, X. Zhang, M. Wang, H. Huang and J. Ma, *J. Electroanal. Chem.*, 2017, **786**, 1–7.
43 H. Yin, Y. Zhou, Q. Ma, S. Ai, P. Ju, L. Zhu and L. Lu, *Process Biochem.*, 2010, **45**, 1707–1712.
44 M. Medina-Sanchez, M. Cadevall, J. Ros and A. Merkoci, *Anal. Bioanal. Chem.*, 2015, **407**, 8445–8449.

Appendix 2

Talanta 237 (2022) 122983

Contents lists available at ScienceDirect

Talanta

journal homepage: www.elsevier.com/locate/talanta

A novel L-cysteine sensor using in-situ electropolymerization of L-cysteine: Potential to simple and selective detection

Wisarut Khamcharoen [a], Charles S. Henry [b], Weena Siangproh [a,*]

[a] Department of Chemistry, Faculty of Science, Srinakharinwirot University, Sukhumvit 23, Wattana, Bangkok, 10110, Thailand
[b] Department of Chemistry, Colorado State University, Fort Collins, CO, 80523-1872, United States

ARTICLE INFO

Keywords:
Poly(Cysteine)
L-cysteine
Origami electrochemical paper-based analytical device
Electrochemistry

ABSTRACT

This work presents an all-in-one origami paper-based electrochemical platform for simple and inexpensive L-cysteine (Cys) detection using Cys as a monomer for modifying electrode surfaces. The proposed method combines the steps of electropolymerization and detection into a single device to offer a highly convenient method for the end-user. In comparison, the sensitivity toward Cys detection is a significantly increased using this modified electrode. The developed device provided a linear concentration range of 10–800 μM with a limit of detection of 5.5 μM. For application, the device was successfully applied to detect Cys in different food products such as wheat flour, bread, and cake with satisfactory results, yielding excellent intra-day and inter-day relative standard deviations (1.5–4.9%) and recoveries (84.2–110.8%). This discovery is important from the viewpoint of the development of Cys detection in other applications in the future.

1. Introduction

L-cysteine (Cys) is one of 20 amino acids and is considered a non-essential amino acid that plays an important role in the functional system of the human body [1]. For example, Cys is involved in the stabilization of protein structure. However, abnormal concentrations of Cys might be related to several symptoms, such as liver damage, hair depigmentation, and stunted growth [2–4]. Hence, the development of effective methodologies for the Cys content has been developed continuously. Aside from being a biomarker for human diseases, Cys has also been used for various applications, including the cosmetic [5], pharmaceutical [6], and food industry [7]. In terms of the food industry, Cys or E920 is widely used as an additive in food products, for example, in bakeries, in which it breaks up the disulfide bonds of the gluten network in wheat flour. This property facilitates greater dough elasticity, which offers faster mixing time and dough relaxation, reducing production time and creating a soft texture in bakery products. Thus, food quality control by monitoring of the amount of Cys in food products is another important and very challenging issue.

The Cys used in the bakery industry is mostly extracted from human hair and feathers from animals such as goose, duck, sheep, and pig [8]. Cys sources produced from any parts of the human body and forbidden animals cannot be used as food additives per regulations in terms of religion. Furthermore, even Cys sources from animals which have not been slaughtered according to Islamic law are not allowed to be used in food ingredients [9]. Even though recently some companies offered Cys synthesized from enzymatic reaction and fermentation, these sources are a small portion of Cys sources in the global market. Based on the small amount of synthesized Cys leading to the use of Cys from forbidden sources. Therefore, it is difficult for analytical chemists to verify whether the Cys came from Halal or non-Halal sources. To protect the Muslim community and avoid non-Halal Cys ingredients, many Muslim countries ban Cys made from non-Halal additive ingredients in food supplies. For example, the Turkish Food Codex Regulation listed Cys as a forbidden additive ingredient in wheat flour. If they find Cys in any Halal bakery products, the company will lose its Halal status and face legal penalties [9]. Thus, detecting Cys in Halal food products is urgent for protecting the Muslim community and raising awareness of food products from non-Muslim countries exported to Muslim markets worldwide. Due to over 3 billion people worldwide are Muslims who reach out to the Halal industries, one of the biggest and fastest growing industries globally.

Previously, Raman microspectroscopy [9] and liquid chromatography-tandem mass spectrometry (LC-MS/MS) [10] were used for the detection of Cys in wheat flours and bakery products. These reports showed good accuracy and precision; however, these

* Corresponding author.
E-mail addresses: weenasi@hotmail.com, weena@g.swu.ac.th (W. Siangproh).

https://doi.org/10.1016/j.talanta.2021.122983
Received 12 June 2021; Received in revised form 14 October 2021; Accepted 19 October 2021
Available online 20 October 2021
0039-9140/

time-consuming methods required complex sample preparation, expensive equipment, and a specialist to operate the equipment and perform the procedures. Consequently, a method that overcomes these limitations is necessary to offer a low-cost, rapid, and simple platform to detect Cys in Halal food products. Most researchers have developed methods for Cys detection in clinical samples using techniques such as spectrophotometric approaches [11,12], high performance liquid chromatography [13,14], and electrochemical techniques [15–17].

Particularly, electrochemistry is an excellent analytical technique for Cys detection because of its advantages, including rapid analysis time, cost-effectiveness, simplicity, accuracy, and precision. Moreover, the new generation of electrochemical instruments is reduced in size to hand-held instruments that can be applied to the on-site analysis. Interestingly, only a complicated traditional electrochemical method was reported to detect Cys for food quality control application [18]. Amino acid polymer-modified electrodes have been widely utilized in sensing applications because these materials provide the best physical and chemical properties, such as high conductivity, stability, compatibility, and simple fabrication [19–22]. Poly(cysteine) (Poly(Cys)) is an alternative amino acid polymer that has attracted more attention in this decade. The material highlights related to the variety of functional groups after modification at the electrode surface revealed carboxyl, amine, and sulfhydryl, therefore offering outstanding electron transfer of analytes at the electrode interface [23]. Unlike molecularly imprinted polymers (MIPs) modified electrodes involve three-dimensional structure of polymer cross-linker around target analyte template for selective strategy which requires a complex and longtime procedure [24]. To overcome these mentioned while remains a selectivity, the idea to develop Cys sensor by using the Cys electropolymerized to form poly (Cys) at the screen-printed graphene electrode (SPGE) surface was prompted proposed. This work used Cys as a monomer for polymeric film modified electrodes to improve electrocatalytic activity of Cys. Furthermore, the highlight of this work is to provide only a single step electropolymerization for electrode modification which significantly offers a more simplicity in preparation step than MIPs as well as the saving cost.

The interest in electrochemical sensors for food analysis in this decade is based on cost-effectiveness, simple platform, rapid detection, portability, and sustainability of the platform [25]. Origami paper-based analytical devices (oPADs) provide important features for designing and developing a new electrochemical platform for Cys detection. Many reports have taken advantage of this platform and integrated it with electrochemical detection to solve specific problems [26–28]. For these reasons, we sought to develop an innovative platform based on the electrochemical sensor and an all-in-one oPAD to simplify Cys analysis.

In this work, we present a platform using electrochemical oPAD for the detection of Cys. An in-situ poly(Cys) modified SPGE was used to amplify the electrochemical responses of Cys. Furthermore, an all-in-one origami paper-based platform coupled with electrochemical detection was created to generate a simple technique using a single device to perform modification and detection. Good analytical detection performances were observed with limit of detection in micro molar range, good sensitivity and selectivity, and excellent response precision and stability. To demonstrate the concept, Halal food products were used as a sample model. The proposed device was applied to detect Cys in food products such as wheat flours, bread, and cake. The device is simple, low-cost, disposable, portable, sensitive, and selective to detect Cys in food products. Therefore, the beneficial advantages of fabrication and the ability to conduct the complex procedures qualify this new device as a tool for food quality control and Halal food investigation and other applications such as clinical analysis.

2. Experimental

2.1. Chemicals, materials and apparatus

L-cysteine, potassium ferricyanide ($K_3Fe(CN)_6$), sodium chloride (NaCl), calcium chloride ($CaCl_2$), l-ascorbic acid, D-glucose, D-sucrose, D-fructose, and folic acid were purchased from Sigma-Aldrich (St. Louis, MO, USA). Nicotinic acid came from Hi-Media Laboratories Pvt. Ltd. (India). Thiamine came from Ajax (Australia). A 0.1 M Phosphate buffer solution (PBS), used as a supporting electrolyte, was prepared using sodium dihydrogen orthophosphate ($NaH_2PO_4.2H_2O$). di-Sodium hydrogen orthophosphate ($Na_2HPO_4.2H_2O$) came from Ajax (Australia). All aqueous solutions in this experiment were prepared in deionized (DI) water.

The electrode surface morphology was studied using a JSM-IT100 scanning electron microscope (SEM) (JEOL Ltd., Japan). The electrochemical measurement, using cyclic voltammetry (CV) and differential pulse voltammetry (DPV), was performed at room temperature on a CHI 1200C potentiostat (Austin, TX, USA). Electrochemical impedance spectroscopy (EIS) was used to characterize the electrode surface to confirm the successful modification using PalmSens4 (Houten, The Netherlands). A three electrode system was fabricated by in-house screen-printing, silver/silver chloride (Ag/AgCl) and graphene inks were bought from Sun chemical (Slough, United Kingdom). The screen-printed blocks were produced by Chaiyaboon Co. Ltd. (Bangkok, Thailand). A three-dimensional (3D) oPAD pattern was generated using a Xerox Color Qube 8570 series wax printer (Xerox, Japan).

2.2. oPAD design and construction

An oPAD pattern was initially drawn using Adobe Illustrator CC software. The wax pattern was printed onto Whatman No.1 filter paper using a wax printer. Then the wax-printed paper was placed on a hot plate at temperature = 180 °C for 30 s to allow wax diffusion into the paper's pore structure to create a hydrophobic feature on filter paper. Three SPGE electrodes were manually screened on paper using an in-house screen-printing method, as shown in Fig. S1a. First, graphene ink was screened on paper to create working and counter electrodes, the geometric surface area of the working electrode is equal to 0.126 cm^2. Then the paper was placed into the oven at 60 °C for 30 min. Ag/AgCl ink was screened on paper to create a reference electrode and conductive connecters. Then the completed paper was placed into the oven at temperature = 60 °C for 30 min. Fig. S1b shows the completed paper consists of a working electrode, counter electrode, and reference electrode screened on wax-patterned paper (wide = 7 cm and height = 3 cm). The oPAD is ready for next electropolymerized modification and Cys detection without electrode pretreatments.

The newly designed oPAD was compared to the conventional electrochemical paper-based analytical device (ePAD), as shown in Fig. 1a. The conventional ePAD proposed from previous reports [29–31] had two main drawbacks that yielded poor electrochemical results. First, the electrodes were screened on the hydrophilic area of the paper, which has heterogeneous and different porosity to each device [32]. Second, some chemical compounds can be adsorbed into cellulose fiber of paper in hydrophilic areas [33]. Both reasons leading to low reproducibility and reliability for device-to-device. To overcome these limitations, we have developed an oPAD by printing three electrodes on the hydrophobic area of a paper device (Fig. 1a). Then, we constructed a spacer layer at the device for creating the solution reservoir (Fig. 1b). This layer enables the solution to remain onto the working electrode surface and aligns three electrodes in the same planar during modification and detection, which is easier for the operation. The components of a single oPAD are shown in Fig. 1b consists of; modification pad, spacers, detection pad, and working pad. Our new device is divided by 3 pads. The working pad is located at a center. The modification and detection pads were separated from each other to prevent Cys contamination from

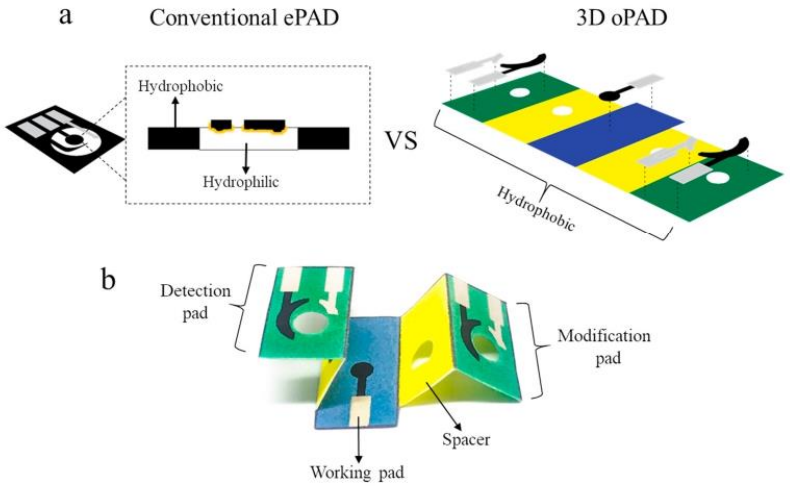

Fig. 1. (a) The comparison configurations of a conventional ePAD vs. a new oPAD and (b) the components of oPAD including modification pad (green layer), spacers (yellow layer), detection pad (green layer) and working pad (blue layer). (For interpretation of the references to colour in this figure legend, the reader is referred to the Web version of this article.)

electropolymerization step to the Cys detection step.

2.3. Modification and detection procedure

The oPAD operational processes are shown in Fig. 2. A hole was added as indicated by the white circle (hole diameter = 4 mm) (Fig. 2a). Then the modification pad was folded down to cover the working pad (Fig. 2b). Next, poly(Cys) was electropolymerized on SPGE by dropping 120 μL of 3 mM Cys in PBS at pH = 8.0 onto the device (Fig. 2c) and applying a potential using CV by sweeping the potential from −0.6 V to +2.0 V for 9 cycles at scan rate = 100 mV/s [34]. Afterward, the poly (Cys) film growth onto the electrode surface was rinsed with DI water and the modification side was torn off (Fig. 2d). For the detection step, the paper at the detection pad was folded over the working pad (Fig. 2e). Then, 120 μL of samples in PBS at pH = 8.0 was added to the device. The electrochemical measurement was performed by DPV (Fig. 2f). The three-electrode system, including poly(Cys) modified SPGE served as a working electrode, SPGE served as a counter electrode, and Ag/AgCl served as a reference electrode. The total analysis time is around 10 min per sample.

2.4. Sample preparation for analysis

To evaluate the power of a newly engineered oPAD for the detection of Cys in food products, the samples, including wheat flour, bread, and cake, were purchased from supermarkets in Bangkok, Thailand. For bread and cake, they were cut into small pieces and 5.0 g of sample was weighed and dissolved with 50 mL of PBS pH = 8.0. Different concentrations of standard solutions of Cys were spiked into the samples and samples were diluted in the supporting electrolytes. The sample solutions were sonicated for 10 min. Finally, sample solutions were centrifuged at 6000 rpm for 20 min. All experiments were measured in

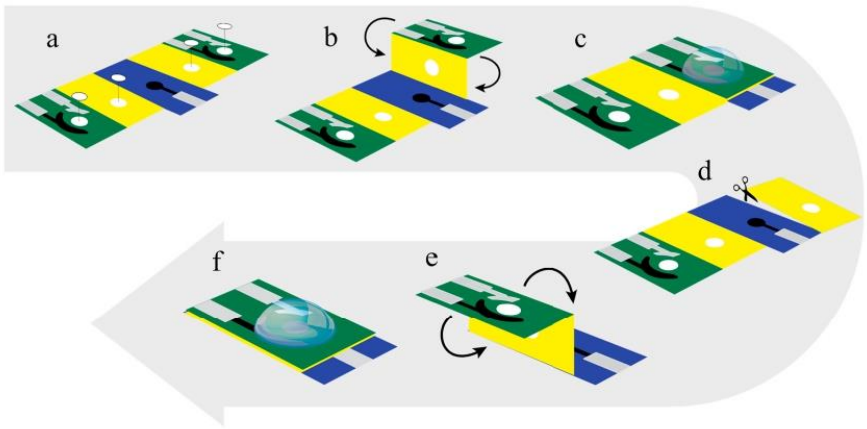

Fig. 2. The oPAD operation and detection of Cys: (a) punch paper at white area (b) fold paper at modification side onto the top of working pad, (c) electropolymerization of poly(Cys), (d) tear the paper at modification side off, (e) fold paper at detection side on the top of working pad and (f) electrochemical measurement of Cys.

triplicate.

3. Results and discussion

3.1. Characterization of a modified electrode

The poly(Cys) was synthesized on the SPGE surface via electropolymerization using 3 mM L-cysteine solution in PBS at pH 8.0 by cyclic voltammetry which scanned from −0.5 V to +2.0 V vs. Ag/AgCl for 9 cycles at a scan rate of 100 mV/s. The mechanism of poly(Cys) growth at the electrode surface can be explained by the SH functional group of Cys was oxidized during CV scan for oxidative direction, which appeared anodic peak at 0.60 V (Fig. 3a). Then, two radicals of Cys were forming disulfide bound at electrode surface, after finishing cycle scanning and poly(Cys) was obtained [35,36]. Furthermore, as seen in the inset of Fig. 3a, the define peak currents decrease after the number of scans has risen also corresponding to passivation of polymer film at electrode surface.

Fig. 3b shows representative cyclic voltammograms of 5 mM $[Fe(CN)_6]^{3-/4-}$ in 0.1 M PBS (pH = 8.0) for bare and poly(Cys) modified SPGE. The redox currents obtained from poly(Cys)/SPGE were higher than bare SPGE. In terms of peak potential, the ΔE for poly(Cys)/SPGE decreased from +0.81 V to +0.54 V compared to bare SPGE. The Randles–Sevcik equation (1) was used to calculate the electroactive surface area [31] before and after electropolymerization using $[Fe(CN)_6]^{3-/4-}$ as the redox probe.

$$I_p = \left(2.69 \times 10^5\right) n^{3/2} A D_0^{1/2} \nu^{1/2} C_0^* \quad (1)$$

where, n is number of electron of redox probe ($n = 1$), A is electroactive surface area (cm^2), D_0 is diffusion coefficient of $[Fe(CN)_6]^{3-/4-} = 7.6 \times 10^{-6}$ cm^2/s, C_0^* is the concentration of $[Fe(CN)_6]^{3-/4-}$ and $I_p/\nu^{1/2}$ was obtained from the slope of relationship plot between the square root of scan rate and electrochemical current. The comparison of calculated electroactive surface areas is shown in Fig. 3c. The areas were as followed: 0.037 cm^2 for bare SPGE, 0.040 cm^2 for poly(Cys) at 3 cycles, 0.046 cm^2 for poly(Cys) at 6 cycles, and 0.054 cm^2 for poly(Cys) at 9 cycles for scanning. From the results, it can be observed that poly(Cys) modified SPGE at 9 cycles of scan provides the highest electroactive surface area, which exhibits an excellent material for detection of Cys. Next, the surface coverages of bare and modified electrodes were calculated using equation (2) [37].

$$\Gamma = \frac{Q}{nFA} \quad (2)$$

where Γ is surface coverage, Q is charge obtained from area under the oxidation peak of supporting electrolyte (Fig. 3d), n is number of involved electron, F is Faraday's constant = 96,485 C/mol and A is electroactive surface area. The surface coverages were compared as followed: 9.9×10^{-8} mol/cm^2 for bare electrode and 3.8×10^{-7} mol/cm^2 for poly(Cys)-modified SPGE. The enriched electroactive surface area and surface coverage indicated the presence of polymer film onto electrode surface.

Fig. 3e shows the EIS spectra for a bare SPGE compared with poly (Cys)-modified SPGE using different electropolymerization conditions to confirm polymer film growth on the electrode. The electron transfer resistance (R_{ct}) between the redox species of 5 mM $[Fe(CN)_6]^{3-/4-}$ in 0.1 M PBS (pH = 8.0) and electrode interface was measured [38]. The R_{ct} for bare SPGE and poly(Cys)/SPGE at 3, 6, and 9 scanned cycles was 52, 41, 28, and 8.0 kΩ, respectively. The decreasing R_{ct} values as a function of increasing electropolymerization scan number demonstrate successful electrode surface modification. The results also agree with the increasing electrode area and surface coverage results.

Besides electrochemical characterization, the surface morphology was characterized by SEM. In Fig. 4a, the SEM image clearly displayed roughness and crumble of graphene sheets over the surface of bare SPGE. Meanwhile, upon the electropolymerization turned into smoother surface (Fig. 4b), this implied the formation of polymeric thin film of poly(Cys) covered up SPGE surface [39]. This result indicated the successful electrode modification of poly(Cys)/SPGE.

3.2. Electrochemical behavior of Cys at poly(Cys)/SPGE

CV and DPV were used to compare the electrochemical responses of Cys detection using bare SPGE and poly(Cys)/SPGE. Fig. 5a shows

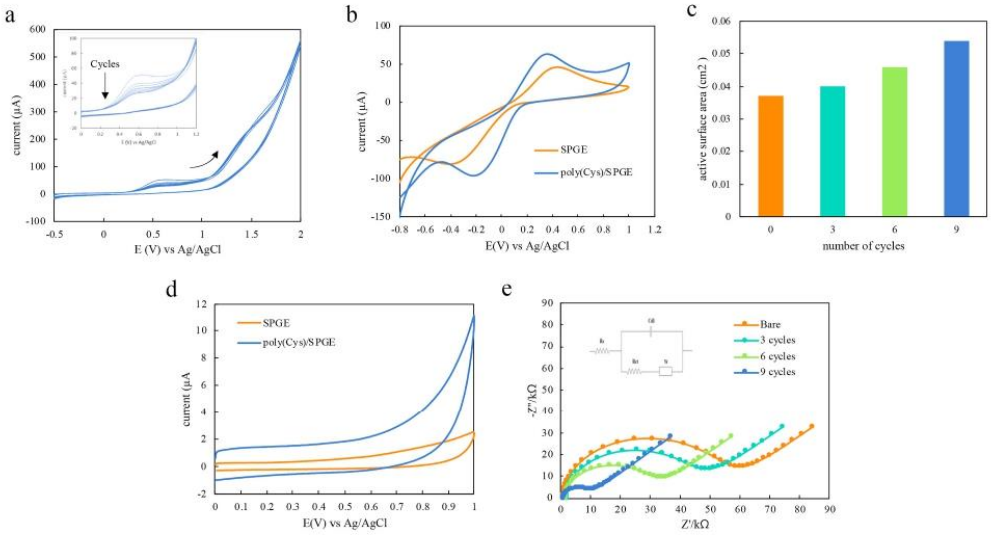

Fig. 3. (a) CV diagram during the electropolymerization of poly(Cys) at SPGE. (b) CV performance of 5 mM $[Fe(CN)_6]^{3-/4-}$ in 0.1 M PBS (pH = 8.0) at bare SPGE and poly(Cys)/SPGE at 9 scanned cycles. (c) Calculated electroactive surfaces at bare SPGE, poly(Cys)/SPGE at 3, 6 and 9 scanned cycles. (d) CV curves of supporting electrolyte (0.1 M PBS at pH 8.0). (e) EIS curves of bare SPGE, poly(Cys)/SPGE at 3, 6 and 9 scanned cycles.

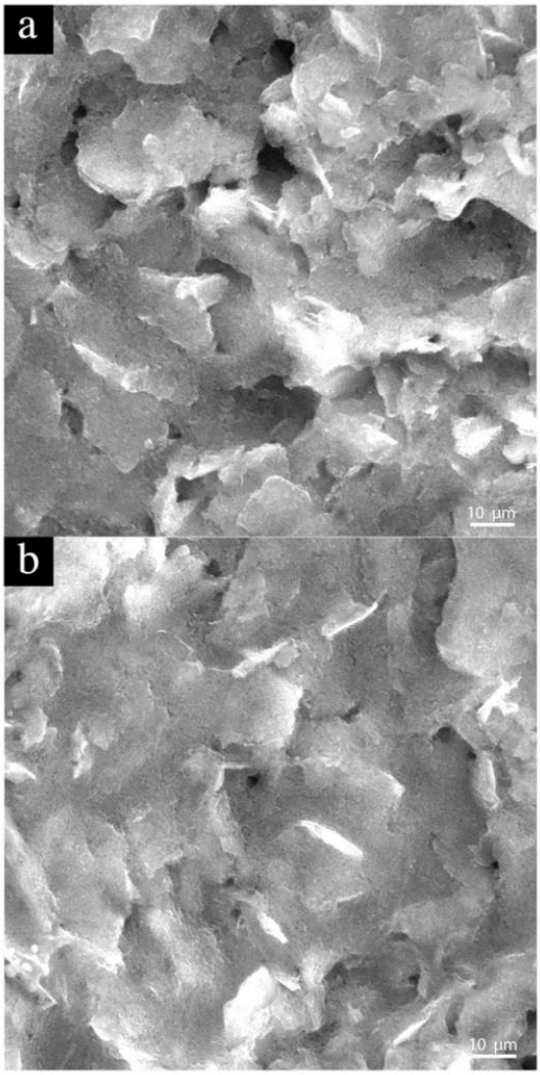

Fig. 4. SEM images of (a) bare SPGE and (b) poly(Cys)/SPGE at 2000 magnification.

representative CVs of standard Cys at bare SPGE. The oxidation potential occurred at +0.50 V. However, the oxidation potential of Cys at poly (Cys)/SPGE was more negative at +0.41 V. For DPV, as shown in Fig. 5b, the oxidation potential shifted negative from +0.36 V at bare SPGE to +0.18 V at poly(Cys)/SPGE (blue line). The obtained lower oxidation potential of Cys can confirm that poly(Cys) could act as an electrocatalyst for Cys detection. Furthermore, the oxidation current obtained for poly(Cys)/SPGE was twice as large as the current obtained at a bare SPGE. These results demonstrated that the electron transfer quickly occurred. The excellent electrochemical performance originates from high conductivity over poly(Cys)/SPGE, due to the presence of sulfhydryl group on polymeric chain structure [40].

To investigate the mass transfer kinetics of Cys at the electrode interface, the oxidation current was measured as a function of scan rate in CV. As shown in Fig. 5c, the peak current increases with increasing scan rates. Furthermore, the linear relationship between the square root of scan rate and Cys oxidation current (inset Fig. 5c), indicates diffusion-controlled mass transfer. Andrieux and Savèant's theoretical model (equation (3)) was used to calculate a diffusion coefficient of Cys (D_0) by using information from the linear relationship of the square root of scan rates and electrooxidation currents of Cys (y = 168.37x − 5.4958) [41].

$$I_p = 0.496FAC_sD_0^{1/2}\left(\frac{F}{RT}\right)^{1/2}\nu^{1/2} \quad (3)$$

where F is Faraday's constant = 96,485 C/mol, R = 8.31447 J/mol·K, T = 298 K, A = 0.054 cm^3, and C_s is Cys concentration = 1×10^{-6} mol/cm^3, I_p is oxidative current of Cys and ν is scan rate. The diffusion coefficient (D_0) of Cys was 1.09×10^{-4} cm^2/s, this value is in agreement with that obtained in previous report [42]. As results from CV curves in Fig. 5c, peak potentials shifted to a positive direction when increasing the scan rate, indicating that Cys electrooxidation is an irreversible process. The equation (4) was used to calculate the number of electron transfers at the electrode interface [43].

$$J_p = \left(2.99 \times 10^5\right)n[(1-\alpha)n_\alpha]^{1/2}AC_sD_0^{1/2}\nu^{1/2} \quad (4)$$

The factor $(1-\alpha)n_\alpha$ was calculated from linear regression of log scan rates and oxidation peak potentials of Cys (E_{pa}) (y = 0.1638x + 0.8089), and the slope was obtained from this relationship, which can be calculated to $(1-\alpha)n_\alpha$ was found to be 0.18. After that, the number of electrons transfer can be estimated to be n = 1.85 or ~2.

The number of protons involved at the electrode surface also was investigated by observing the electrochemical behavior of Cys in the different pH conditions. Fig. 5d shows CV curves of Cys at poly(Cys)/SPGE in pH range of 5.0–9.0; it is clearly seen that the oxidation peak potentials (E_{pa}) were shifted to a positive direction when pH values increased. Moreover, the linear relationship between pH values and oxidation peak potentials was plotted (y = −0.0648x + 1.0164), then the Nernst equation (5) was used to describe this relationship.

$$E_{pa} = E^0 + \left(\frac{0.0591}{n}\right)\log\left[\frac{(ox)a}{Rb}\right] - \left(0.0591\frac{m}{n}\right)pH \quad (5)$$

where m and n are the number of electrons and protons at the electrode interface, respectively [44]. The slope was calculated to be 0.0648, which is close to the theoretical value 0.0591. This result illustrates that the number of electron and proton transferred at the electrode interface are equal, which means m = n = 2. Thus, the mechanism of Cys oxidized at poly(Cys)/SPGE involves two electrons and two protons, which was in agreement with previous works [45–47].

3.3. Optimization of experimental conditions

The optimization of several parameters was systematically studied and described in supplementary information.

3.4. Analytical performance

The quantitative determination of Cys was performed by DPV based by generating a standard curve (Fig. 6a and b). The linear concentration range of the sensor was found to be between 10 and 800 μM with a linear regression equation of $i_{pa} = 0.0517C_{Cys} + 0.6941$ ($R^2 = 0.9987$) (Fig. 6c). The calculated limit of detection (LOD) was 5.5 μM (3SD/slope). The linear range and LOD obtained from this device are sufficiently sensitive for detecting Cys in food samples which is the main application of this work. Comparing the analytical performance of the proposed platform and the other techniques for the detection of Cys in food products was also performed. The new platform exhibited a wider linear concentration range and a lower LOD than Raman microspectroscopy [9]. Although the LC-MS/MS method [10] offered lower

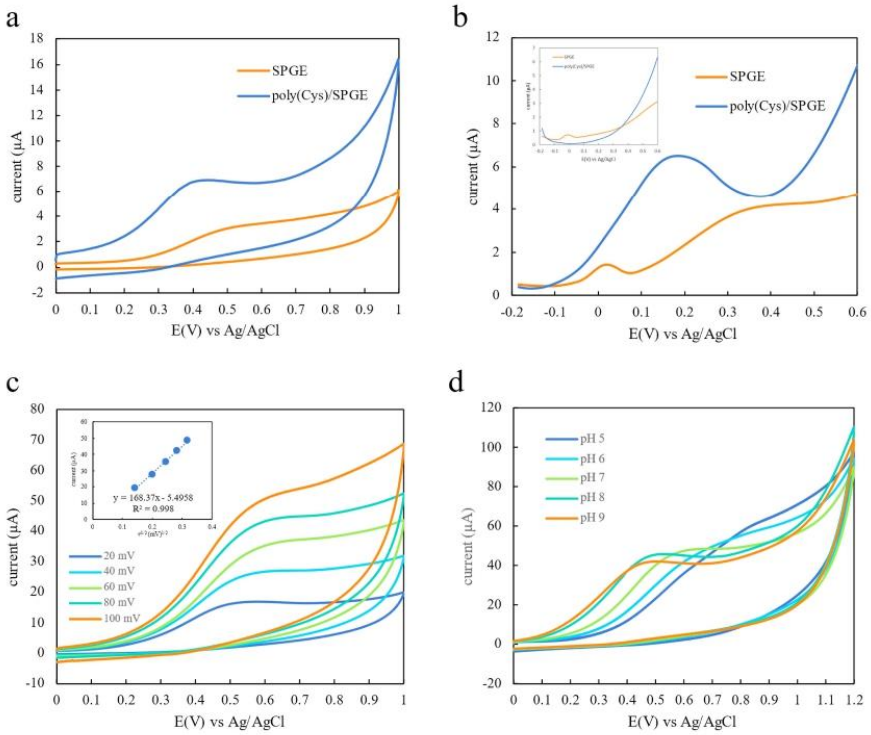

Fig. 5. (a) and (b) represent CV and DPV diagrams of 100 μM Cys in PBS at pH = 8.0 using bare SPGE compared to poly(Cys)/SPGE. (c) CV curves of 1 mM Cys in PBS at pH = 8.0 at poly(Cys)/SPGE using different scan rate, inset shows linear relationship between square root of scan rates and electrochemical currents. (d) CV curves of 1 mM Cys in PBS at different pH values.

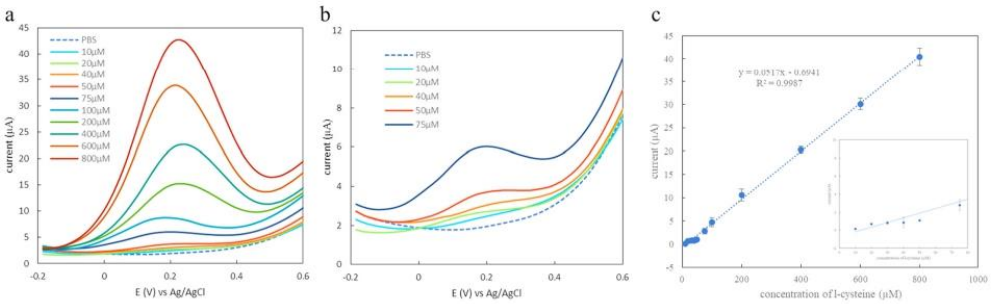

Fig. 6. (a) and (b) DPV current responses from 0 μM to 800 μM Cys in PBS pH 8.0. (c) Linear relationship of Cys concentrations and oxidation currents. Error bars were obtained based on three replicates (n = 3), standard deviations were shown in the range of 0.04–1.8 μA.

LOD, anyway, the proposed platform allowed for simple sample preparation and operation, sensitive detection, low-cost, and fast analysis. These characteristics lead to a very useful and practical technique for applying to real-world analysis.

3.5. Selectivity

We next explored the specificity by detection of 100 μM Cys in the presence of common food additive compounds found in bakery products, including 1 mM thiamine (vitamin B_1), 1 mM nicotinic acid (vitamin B_3), 1 mM folic acid (vitamin B_9), 1 mM ascorbic acid (vitamin C), 10 mM glucose, 10 mM fructose, 10 mM sucrose, 1000 mg/L Na^+, 1000 mg/L Mg^{2+}, 1000 mg/L Fe^{2+}, and 1000 mg/L Ca^{2+}. In Fig. 7, there were no significant change in current (less than 5%) when detecting Cys in the presence of these interferences. Thus, this proposed platform offered an excellent specificity in food samples toward Cys detection.

3.6. Real sample analysis

To demonstrate the proposed platform's sensing applicability, the determination of Cys in bakery products was tested. The standard addition method was used to measure the amount of Cys in real samples.

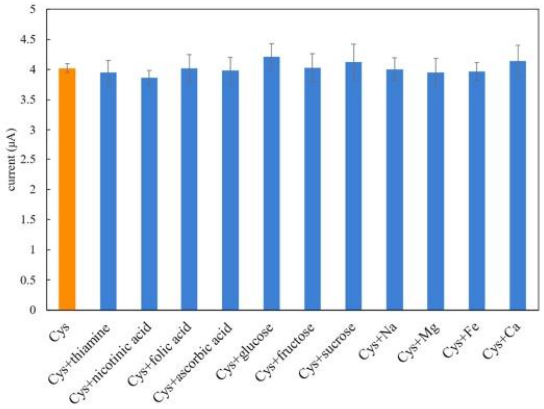

Fig. 7. The interference study of the proposed platform for the detection of Cys in the presence of common food additive compounds. Error bars were obtained based on three replicates (n = 3), the standard deviations were shown in the range of 0.1–0.3 μA.

The recovery test was studied by spiking the standard Cys (100, 200, and 600 μM) in wheat flours, bread, and cake. The recovery and relative standard deviation values (%) are listed in Table 1 to evaluate the accuracy and precision found in the acceptable value ranges of 84.2%–110.8% and 1.5%–4.9%, respectively. In addition, the amount of Cys was 63.0 mg/kg in wheat flour 1, 13.8 mg/kg in wheat flour 2, 44.6 mg/kg in bread, and 81.0 mg/kg in the cake. These results indicated the powerful sensing ability for the detection of Cys in food products.

4. Conclusion

We demonstrated a new all-in-one origami paper-based electrochemical analytical device using self-modification poly(Cys) modified SPGE as a novel sensing platform to detect Cys in food products. The proposed platform was designed to combine modification and detection steps into a single device to facilitate the simplest method for the end-user. Furthermore, in an electrochemical study, we developed a new sensing device for Cys detection for the first time by using the polymerization of itself to increase sensitivity and selectivity. This poly(Cys) exhibited great electrocatalytic activity and performed a wide linear response with lowest possible LOD to determine Cys in focusing applications. The developed device was successfully used to quantify the amount of Cys in food product samples. The innovative platform provides a simple, ready-to-use, inexpensive, portable, and rapid detection of Cys in food products. It offers a high potential for real-time monitoring of food quality control in the food industry and for Halal food investigation applications.

Table 1
The analytical application of the proposed platform for the detection of Cys in bakery products (n = 3).

Sample	Spiked (μM)	Found (μM)	Recovery (%)	RSD (%)
Wheat flour 1	100	110.8 ± 4.6	110.8	4.2
	200	180.7 ± 1.9	90.3	4.2
	600	604.7 ± 21.3	100.8	3.5
Wheat flour 2	100	84.2 ± 3.2	84.2	3.8
	200	207.4 ± 7.3	103.7	3.5
	600	599.9 ± 20.2	100.0	3.4
Bread	100	90.8 ± 3.4	90.8	3.7
	200	215.7 ± 9.6	107.8	4.5
	600	595.9 ± 16.5	99.3	2.8
Cake	100	87.9 ± 3.2	87.9	3.7
	200	216.4 ± 3.2	108.2	1.5
	600	594.0 ± 29.1	99.0	4.9

Credit author statement

Wisarut Khamcharoen: Conceptualization, Methodology, Writing-Original Draft. **Charles S. Henry**: Supervision, Writing- Reviewing and Editing. **Weena Siangproh**: Conceptualization, Resources, Funding acquisition, Project administration, Supervision, Writing- Reviewing and Editing.

Declaration of competing interest

The authors declare that they have no known competing financial interests or personal relationships that could have appeared to influence the work reported in this paper.

Acknowledgement

W.K. would like to thank Science Achievement Scholarship of Thailand (SAST) and W.S. would like to thank the National Research Council of Thailand (NRCT) and Srinakharinwirot University for financial support through Research Grants for Talented Mid-Career Researchers (N41A640098).

Appendix A. Supplementary data

Supplementary data to this article can be found online at https://doi.org/10.1016/j.talanta.2021.122983.

References

[1] K.K. Aswini, A.M. Vinu Mohan, V.M. Biju, Molecularly imprinted polymer based electrochemical detection of L-cysteine at carbon paste electrode, Mater. Sci. Eng. C Mater. Biol. Appl. 37 (2014) 321–326.
[2] H.S. Hashemi, A. Nezamzadeh-Ejhieh, M. Karimi-Shamsabadi, A novel cysteine sensor based on modification of carbon paste electrode by Fe(II)-exchanged zeolite X nanoparticles, Mater. Sci. Eng. C Mater. Biol. Appl. 58 (2016) 286–293.
[3] G. Salemi, M.C. Gueli, M. D'Amelio, V. Saia, P. Mangiapane, P. Aridon, P. Ragonese, I. Lupo, Blood levels of homocysteine, cysteine, glutathione, folic acid, and vitamin B12 in the acute phase of atherothrombotic stroke, Neurol. Sci. 30 (2009) 361–364.
[4] S. Wu, X. Lan, F. Huang, Z. Luo, H. Ju, C. Meng, C. Duan, Selective electrochemical detection of cysteine in complex serum by graphene nanoribbon, Biosens. Bioelectron. 32 (2012) 293–296.
[5] M. Iorizzo, B.M. Piraccini, A. Tosti, Nail cosmetics in nail disorders, J. Cosmet. Dermatol. 6 (2007) 53–58.
[6] K.R. Atkuri, J.J. Mantovani, L.A. Herzenberg, L.A. Herzenberg, N-Acetylcysteine–a safe antidote for cysteine/glutathione deficiency, Curr. Opin. Pharmacol. 7 (2007) 355–359.
[7] H. Takagi, I. Ohtsu, l-Cysteine metabolism and fermentation in microorganisms, in: A. Yokota, M. Ikeda (Eds.), Amino Acid Fermentation, Springer Japan, Tokyo, 2017, pp. 129–151.
[8] N.I. Ismail, Y.Z.H. Hashim, P. Jamal, R. Othman, H.M. Salleh, Production of Cysteine : approaches , challenges and potential solution, Int. J. Biotechnol. Wellness Ind. 3 (2014) 95–101.
[9] N. Cebi, C.E. Dogan, A. Develioglu, M.E. Yayla, O. Sagdic, Detection of l-Cysteine in wheat flour by Raman microspectroscopy combined chemometrics of HCA and PCA, Food Chem. 228 (2017) 116–124.
[10] C.E. Dogan, N. Cebi, A. Develioglu, E.O. Olgun, O. Sagdic, Detection of cystine and cysteine in wheat flour using a robust LC-MS/MS method, J. Cereal. Sci. 84 (2018) 49–54.
[11] G. Chai, Q. Liu, Q. Fei, J. Zhang, X. Sun, H. Shan, G. Feng, Y. Huan, A selective and sensitive fluorescent sensor for cysteine detection based on bi-8-carboxamidoquinoline derivative and Cu(2+) complex, Luminescence 33 (2018) 153–160.
[12] F. Wang, Y. Zhu, J. Xu, Z. Xu, G. Cheng, W. Zhang, Highly selective and ratiometric fluorescent nanoprobe for the detection of cysteine and its application in test strips, Anal. Bioanal. Chem. 410 (2018) 4875–4884.
[13] A. Kaminska, P. Olejarz, K. Borowczyk, R. Glowacki, G. Chwatko, Simultaneous determination of total homocysteine, cysteine, glutathione, and N-acetylcysteine in brain homogenates by HPLC, J. Separ. Sci. 41 (2018) 3241–3249.
[14] L. Zhang, B. Lu, C. Lu, J.M. Lin, Determination of cysteine, homocysteine, cystine, and homocystine in biological fluids by HPLC using fluorosurfactant-capped gold nanoparticles as postcolumn colorimetric reagents, J. Separ. Sci. 37 (2014) 30–36.
[15] M. Heidari, A. Ghaffarinejad, Electrochemical sensor for L-cysteine by using a cobalt(II)/aluminum(III) layered double hydroxide as a nanocatalyst, Microchim. Acta. 186 (2019) 365.

[16] P.T. Lee, J.E. Thomson, A. Karina, C. Salter, C. Johnston, S.G. Davies, R. G. Compton, Selective electrochemical determination of cysteine with a cyclotricatechylene modified carbon electrode, Analyst 140 (2015) 236–242.
[17] A. Safavi, R. Ahmadi, F.A. Mahyari, Simultaneous electrochemical determination of L-cysteine and L-cysteine disulfide at carbon ionic liquid electrode, Amino Acids 46 (2014) 1079–1085.
[18] M. Scampicchio, N.S. Lawrence, A. Arecchi, S. Cosio, S. Mannino, Voltammetric detection of free sulfhydryl compounds in food flours, Electroanalysis 19 (2007) 85–90.
[19] K.v. Harisha, B.E. Kumara Swamy, P.S. Ganesh, H. Jayadevappa, Electrochemical oxidation of haematoxylin at poly(alanine) modified carbon paste electrode: a cyclic voltammetric study, J. Electroanal. Chem. 832 (2019) 486–492.
[20] J. Zhou, Y. Chen, L. Lan, C. Zhang, M. Pan, Y. Wang, B. Han, Z. Wang, J. Jiao, Q. Chen, A novel catalase mimicking nanocomposite of Mn(II)-poly-L-histidine-carboxylated multi walled carbon nanotubes and the application to hydrogen peroxide sensing, Anal. Biochem. 567 (2019) 51–62.
[21] E.S. Gomes, F.R.F. Leite, B.R.L. Ferraz, H.A.J.L. Mourão, A.R. Malagutti, Voltammetric sensor based on cobalt-poly(methionine)-modified glassy carbon electrode for determination of estriol hormone in pharmaceuticals and urine, J. Pharm. Anal. 9 (2019) 347–357.
[22] S. He, P. He, X. Zhang, X. Zhang, K. Liu, L. Jia, F. Dong, Poly(glycine)/graphene oxide modified glassy carbon electrode: preparation, characterization and simultaneous electrochemical determination of dopamine, uric acid, guanine and adenine, Anal. Chim. Acta 1031 (2018) 75–82.
[23] K. Zhang, P. Luo, J. Wu, W. Wang, B. Ye, Highly sensitive determination of Sunset Yellow in drink using a poly (l-cysteine) modified glassy carbon electrode, Anal. Methods. 5 (2013) 5044–5050.
[24] P. Yáñez-Sedeño, S. Campuzano, J.M. Pingarrón, Electrochemical sensors based on magnetic molecularly imprinted polymers: a review, Anal. Chim. Acta 960 (2017) 1–17.
[25] F. Arduini, S. Cinti, V. Caratelli, L. Amendola, G. Palleschi, D. Moscone, Origami multiple paper-based electrochemical biosensors for pesticide detection, Biosens. Bioelectron. 126 (2019) 346–354.
[26] Y. Liu, K. Cui, Q. Kong, L. Zhang, S. Ge, J. Yu, A self-powered origami paper analytical device with a pop-up structure for dual-mode electrochemical sensing of ATP assisted by glucose oxidase-triggered reaction, Biosens. Bioelectron. 148 (2020) 111839.
[27] N. Colozza, K. Kehe, G. Dionisi, T. Popp, A. Tsoutsoulopoulos, D. Steinritz, D. Moscone, F. Arduini, A wearable origami-like paper-based electrochemical biosensor for sulfur mustard detection, Biosens. Bioelectron. 129 (2019) 15–23.
[28] S. Boonkaew, S. Chaiyo, S. Jampasa, S. Rengpipat, W. Siangproh, O. Chailapakul, An origami paper-based electrochemical immunoassay for the C-reactive protein using a screen-printed carbon electrode modified with graphene and gold nanoparticles, Microchim. Acta. 186 (2019) 153.
[29] K. Pungjunun, S. Chaiyo, N. Praphairaksit, W. Siangproh, A. Ortner, K. Kalcher, O. Chailapakul, E. Mehmeti, Electrochemical detection of NOx gas based on disposable paper-based analytical device using a copper nanoparticles-modified screen-printed graphene electrode, Biosens. Bioelectron. 143 (2019) 111606.
[30] Y. Panraksa, W. Siangproh, T. Khampieng, O. Chailapakul, A. Apilux, Paper-based amperometric sensor for determination of acetylcholinesterase using screen-printed graphene electrode, Talanta 178 (2018) 1017–1023.
[31] K. Charoenkitamorn, S. Chaiyo, O. Chailapakul, W. Siangproh, Low-cost and disposable sensors for the simultaneous determination of coenzyme Q10 and alpha-lipoic acid using manganese (IV) oxide-modified screen-printed graphene electrodes, Anal. Chim. Acta 1004 (2018) 22–31.
[32] M. Punjiya, C.H. Moon, Z. Matharu, H. Rezaei Nejad, S. Sonkusale, A three-dimensional electrochemical paper-based analytical device for low-cost diagnostics, Analyst 143 (2018) 1059–1064.
[33] C. Renault, X. Li, S.E. Fosdick, R.M. Crooks, Hollow-channel paper analytical devices, Anal. Chem. 85 (2013) 7976–7979.
[34] B.R. Ferraz, F.R. Leite, A.R. Malagutti, Simultaneous determination of ethionamide and pyrazinamide using poly(l-cysteine) film-modified glassy carbon electrode, Talanta 154 (2016) 197–207.
[35] C.A. Martínez-Huitle, M. Cerro-Lopez, M.A. Quiroz, Electrochemical behaviour of dopamine at covalent modified glassy carbon electrode with L-Cysteine: preliminary results, Mater. Res. 12 (2009) 375–384.
[36] Y. Wang, G. Liu, X. Hou, Y. Huang, C. Li, K. Wu, Assembling gold nanorods on a poly-cysteine modified glassy carbon electrode strongly enhance the electrochemical reponse to tetrabromobisphenol A, Microchim. Acta. 183 (2016) 689–696.
[37] D.R. Kumar, S. Kesavan, T.T. Nguyen, J. Hwang, C. Lamiel, J.J. Shim, Polydopamine@electrochemically reduced graphene oxide-modified electrode for electrochemical detection of free-chlorine, Sensor. Actuator. B Chem. 240 (2017) 818–828.
[38] X. Zhang, Y. Yu, J. Shen, W. Qi, H. Wang, Design of organic/inorganic nanocomposites for ultrasensitive electrochemical detection of a cancer biomarker protein, Talanta 212 (2020) 120794.
[39] R.G. Krishnan, B. Saraswathyamma, Electro-generated poly (cysteine) film as a sensor platform towards the simultaneous electroanalysis of hydrazine and hydroxylamine, Mater. Chem. Phys. 271 (2021) 124880.
[40] E. Sohouli, M. Ghalkhani, M. Rostami, M. Rahimi-Nasrabadi, F. Ahmadi, A noble electrochemical sensor based on TiO2@CuO-N-rGO and poly (L-cysteine) nanocomposite applicable for trace analysis of flunitrazepam, Mater. Sci. Eng. C 117 (2020) 111300.
[41] A.C. Boni, A. Wong, R.A.F. Dutra, M.D.P.T. Sotomayor, Cobalt phthalocyanine as a biomimetic catalyst in the amperometric quantification of dipyrone using FIA, Talanta 85 (2011) 2067–2073.
[42] D. Geng, M. Li, X. Bo, L. Guo, Molybdenum nitride/nitrogen-doped multi-walled carbon nanotubes hybrid nanocomposites as novel electrochemical sensor for detection L-cysteine, Sensor. Actuator. B Chem. 237 (2016) 581–590.
[43] P. Nakthong, T. Kondo, O. Chailapakul, W. Siangproh, Development of an unmodified screen-printed graphene electrode for nonenzymatic histamine detection, Anal. Methods. 12 (2020) 5407–5414.
[44] T. Thomas, R.J. Mascarenhas, D.S. Oj, S. Detriche, Z. Mekhalif, P. Martis, Pristine multi-walled carbon nanotubes/SDS modified carbon paste electrode as an amperometric sensor for epinephrine, Talanta 125 (2014) 352–360.
[45] P.A. Rasheed, R.P. Pandey, K.A. Jabbar, J. Ponraj, K.A. Mahmoud, Sensitive electrochemical detection of l-cysteine based on a highly stable Pd@Ti3C2T:X (MXene) nanocomposite modified glassy carbon electrode, Anal. Methods. 11 (2019) 3851–3856.
[46] M. Singh, N. Jaiswal, I. Tiwari, C.W. Foster, C.E. Banks, A reduced graphene oxide-cyclodextrin-platinum nanocomposite modified screen printed electrode for the detection of cysteine, J. Electroanal. Chem. 829 (2018) 230–240.
[47] R. Thota, V. Ganesh, Simple and facile preparation of silver-polydopamine (Ag-PDA) core-shell nanoparticles for selective electrochemical detection of cysteine, RSC Adv. 6 (2016) 49578–49587.

Appendix 3

ACS SENSORS

pubs.acs.org/acssensors

Article

Electrochemical Capillary-Flow Immunoassay for Detecting Anti-SARS-CoV-2 Nucleocapsid Protein Antibodies at the Point of Care

Isabelle C. Samper,♦ Ana Sánchez-Cano,♦ Wisarut Khamcharoen,♦ Ilhoon Jang, Weena Siangproh, Eva Baldrich, Brian J. Geiss, David S. Dandy, and Charles S. Henry*

Cite This: ACS Sens. 2021, 6, 4067−4075

Read Online

ACCESS | Metrics & More | Article Recommendations | Supporting Information

ABSTRACT: Rapid and inexpensive serological tests for SARS-CoV-2 antibodies are needed to conduct population-level seroprevalence surveillance studies and can improve diagnostic reliability when used in combination with viral tests. Here, we report a novel low-cost electrochemical capillary-flow device to quantify IgG antibodies targeting SARS-CoV-2 nucleocapsid proteins (anti-N antibody) down to 5 ng/mL in low-volume (10 μL) human whole blood samples in under 20 min. No sample preparation is needed as the device integrates a blood-filtration membrane for on-board plasma extraction. The device is made of stacked layers of a hydrophilic polyester and double-sided adhesive films, which create a passive microfluidic circuit that automates the steps of an enzyme-linked immunosorbent assay (ELISA). The sample and reagents are sequentially delivered to a nitrocellulose membrane that is modified with a recombinant SARS-CoV-2 nucleocapsid protein. When present in the sample, anti-N antibodies are captured on the nitrocellulose membrane and detected via chronoamperometry performed on a screen-printed carbon electrode. As a result of this quantitative electrochemical readout, no result interpretation is required, making the device ideal for point-of-care (POC) use by non-trained users. Moreover, we show that the device can be coupled to a near-field communication potentiostat operated from a smartphone, confirming its true POC potential. The novelty of this work resides in the integration of sensitive electrochemical detection with capillary-flow immunoassay, providing accuracy at the point of care. This novel electrochemical capillary-flow device has the potential to aid the diagnosis of infectious diseases at the point of care.

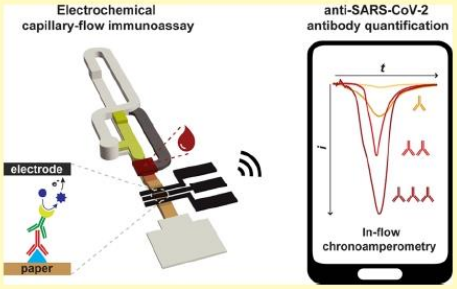

KEYWORDS: *point-of-care (POC) diagnostics, capillary-flow device, electrochemistry, SARS-CoV-2, serology*

■ INTRODUCTION

Coronavirus disease (COVID-19) caused by the severe acute respiratory syndrome coronavirus 2 (SARS-CoV-2) was classified as a pandemic by the World Health Organization and has caused over 4 M deaths worldwide as of July 2021.[1] In order to contain the pandemic, different strategies have been developed within the last year to detect SARS-CoV-2 infections and monitor the virus spread. Both antigen and antibody detection play important roles in pandemic management as well as assessment of patient prognosis.

Reverse transcription polymerase chain reaction (RT-qPCR) is considered to be the gold standard method for detecting the presence of virus, while rapid antigen tests are used for screening at point-of-care (POC) facilities.[2] Meanwhile, serological testing has become key for population-level surveillance because it can be used to detect previous exposure to SARS-CoV-2, even in asymptomatic patients, and enables identification of individuals that remain susceptible to the virus.[3] Thus, seroprevalence analysis can guide decision making around social restrictions and lockdown measures that are in place in most countries.[4] Moreover, serological assays can be used in combination with RT-qPCR to improve COVID-19 diagnostic reliability,[5,6] as well as to establish contact tracing, to identify convalescence plasma donors and to study antibody titers following vaccination.[7]

Current serological assays for COVID-19 include neutralization assays, enzyme-linked immunosorbent assays (ELISAs), and chemiluminescent immunoassays.[8] Whilst being highly sensitive, these assays take hours to days to provide results and require laboratory instrumentation that is not widely available in low-income settings or at the point of care.[9] In response to the need for rapid tests imposed by the worldwide pandemic, multiple COVID-19 serology assays,[6,8,10,11] including POC assays[12] are rapidly emerging. Of the rapid COVID-19 serology tests that are commercially available, most use

Received: July 19, 2021
Accepted: October 12, 2021
Published: October 25, 2021

https://doi.org/10.1021/acssensors.1c01527
ACS Sens. 2021, 6, 4067−4075

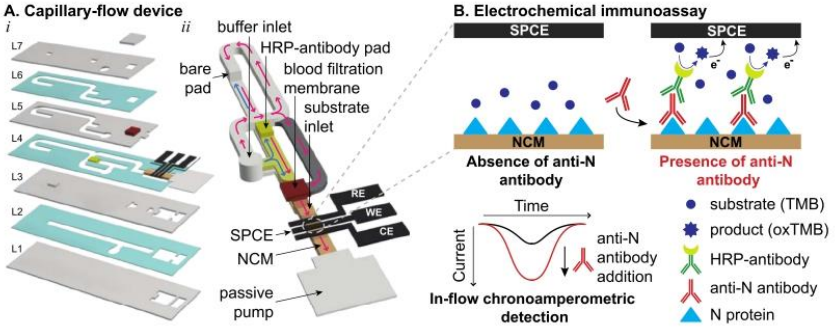

Figure 1. Schematic overview of the electrochemical capillary-flow immunoassay. (A) Exploded view (i) and 3-dimensional view (ii) of the capillary-flow device incorporating a stencil printed carbon electrode (SPCE) facing a NCM. Exploded view (i) shows the four layers of polyester film (gray, L1, L3, L5, L7) and the three layers of double-sided adhesive (turquoise, L2, L4, L6) assembled to create the 3-dimensional microfluidic network represented in (ii). Pink arrows indicate flow direction during delivery regime. In channels where flow direction is different between filling and delivery regimes, blue arrows indicate flow direction during filling regime. Where channels are superimposed, arrows indicate flow direction in both top and bottom channels. (B) Electrochemical immunoassay and detection mechanism. If present in the sample, anti-N antibodies are captured by N proteins striped on the NCM. Secondary HRP-labeled antibodies subsequently bind to anti-N antibodies and catalyze the oxidation of the substrate TMB, creating an electroactive compound (oxTMB) that is detected via chronoamperometry.

holes) were designed using CorelDRAW and cut with a CO_2 laser cutter, to create the 3D microfluidic network shown in Figure 1A. An HRP-antibody reagent pad was placed in the device channel before adding the top layer of polyester film. Then, a blood-filtration membrane (Vivid GX Membrane, Pall Corporation) was placed over the sample inlet, to retain blood cells and deliver plasma to the microfluidic channel. Subsequently, a NCM striped with an N protein was inserted at the outlet of the microfluidic channel, and a waste pad (Grade 1 CHR, Whatman PLC) was placed over the end of the NCM to create a passive pump for the fluidic system. Finally, a SPCE was placed on top of the NCM, upside-down, so that the working electrode (WE) was in contact with the N protein strip. The SPCE was held in position on the NCM by the layer four adhesive (L4, Figure 1Ai).

Device Operation and Electrochemical Recording. The assay was initiated by adding a 10 μL blood sample onto the blood-filtration membrane. Then, 85 μL of washing buffer were added to the buffer inlet, as shown in Video S1. Once the buffer had started to flow through the NCM, a 0.0 V potential was applied to the WE (vs the AglAgCl RE) using a portable potentiostat (PalmSens4) and chronoamperometry recording started. Following the sequential and automated delivery of sample, washing buffer, HRP-antibody and washing buffer to the NCM, 1 μL of TMB was added to the substrate inlet on the NCM, as indicated in Figure 1Aii. In the presence of HRP in the detection zone, TMB gets oxidized into an electrochemically active product (oxTMB), which is then reduced at the electrode surface, generating an increase in the cathodic current. The electrochemical immunoassay detection mechanism is illustrated in Figure 1B.

■ RESULTS AND DISCUSSION

Electrochemical Capillary-Flow Device Design. The electrochemical capillary-flow device was developed with the aim of detecting anti-SARS-CoV-2 N protein specific antibodies with high sensitivity at the point of care. The design of the capillary-flow device was based on previous POC devices developed by our group[32,33,37] and incorporated a SPCE to allow for high-sensitivity detection. Assembled layers of laser-cut polyester and double-sided adhesive films created the microfluidic circuit shown in Figure 1A. This microfluidic circuit provided sequential delivery of the reagents used in the electrochemical immunoassay to a detection zone. The detection zone consisted of a NCM that was modified with a capturing agent, recombinant SARS-CoV-2 N protein, and a SPCE in contact with it. The SPCE had been plasma-treated for improved electrochemical performance, as previously characterized.[41] The flow was maintained by an absorbent waste pad placed downstream from the detection zone.

The capillary flow-driven assay was initiated by adding a 10 μL sample of whole blood on the blood-filtration membrane. This allowed blood cells to be retained in the membrane, while plasma passed through it and entered the channel. The buffer was then added to the device, simultaneously filling all the device channels by capillary action, as illustrated by the arrows in Figure 1Aii) and shown in Video S1. This was possible, thanks to a bare glass fiber pad (L3, Figure 1Ai) and a vent hole (L7, Figure 1Ai) that were added to the buffer channel to prevent air from being trapped. The buffer flow under the blood-filtration membrane carried blood plasma to the NCM. If present in the sample, anti-N antibodies bound to the N proteins immobilized on the NCM (Figure 1B). While buffer kept flowing in the channels and through the NCM, washing away unbound sample components, HRP-antibodies were released from the reagent pad placed on L4 (Figure 1A) and subsequently delivered to the NCM. At this point, HRP antibodies bound to anti-N antibodies if present on the NCM. To prevent non-specific absorption of HRP-antibody the blood-filtration membrane, which could act as a passive pump due to evaporation, the center channel was split into two superimposed channels and a hydration channel was incorporated into the device (shown in dark gray in Figure 1Aii). This enabled the plasma to flow through the top channel while the washing buffer and the HRP-antibody flow through the bottom one (so called HRP-antibody delivery channel, shown in yellow in Figure 1Aii). Both channels converged at the end of the device, after the blood-filtration membrane but before the NCM. Evaporation of solution through the filtration membrane was also minimized by covering it with a lid made of a polyester film (Figure 1Ai). Following HRP-antibody delivery, the excess of HRP-antibody that had bound to the NCM was washed off automatically by the washing buffer running through the device. Lastly, 1 μL of the TMB substrate

https://doi.org/10.1021/acssensors.1c01527
ACS Sens. 2021, 6, 4067−4075

was added to the substrate inlet on the NCM, as indicated in Figure 1Aii. From there, it flowed to the detection zone where it was oxidized by HRP when present. The resulting electroactive compound (oxTMB) was finally detected via chronoamperometry using the SPCE held on the NCM. The complete sandwich immunoassay and electrochemical detection mechanism are illustrated in Figure 1B.

Sequential Delivery of Reagents. The ability of the capillary-flow device to sequentially deliver reagents to the detection zone was demonstrated with a whole blood sample and color dyes to mimic reagents, as shown in Figure 2.

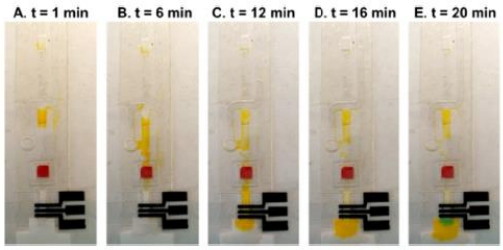

Figure 2. Sequential delivery of blood sample (A), washing buffer (B), HRP-antibodies (C) washing buffer (D), and TMB (E) to the detection area. HRP-antibody and TMB solutions are represented by yellow and blue dyes, respectively.

Once the sample and the buffer were introduced in the device, the flow started and pulled the plasma through the NCM in 1 min (Figure 2A). Efficient blood cell filtration through the filtration membrane was confirmed by visually assessing the color of the solution flowing through the NCM and the absorbent waste pad. While dark red residue remained on the membrane, the fluid emerging through the membrane was clear (Figure 2A). This observation is consistent with results published by our group and others.[37,42,43] Following plasma delivery to the NCM and a subsequent buffer wash (Figure 2B), the yellow dye that had dried on the reagent pad to mimic the HRP-antibody was released through the HRP-antibody delivery channel and flowed to the detection zone (Figure 2C, 12 min). Simultaneously, buffer flowed through the hydration channel to keep the blood-filtration membrane hydrated, driving the flow to the NCM. After approximately 1 min, the HRP-antibody-mimicking yellow solution stopped flowing through the NCM and washing buffer from the buffer channel was delivered instead, to wash out excess HRP-antibody (Figure 2D). Lastly, 1 μL of substrate-mimicking blue solution was added to the device at time 16 min and flowed past the detection zone in 4 min (Figure 2E, 20 min). Overall, these results confirm that the reagents are sequentially delivered to the detection zone in less than 20 min. Estimated incubation periods in the devices are 3 min for blood, 6 min for rehydrated HRP-antibody, and 4 min for TMB on the detection zone, with automatic buffer washes between them.

Static Electrochemical Detection of Anti-N Antibodies. Initial anti-N antibody assays were performed on PBS-based samples using a capillary-flow device identical to the one shown in Figure 1A, but without a blood-filtration membrane and a hydration channel (Figure S1). The first anti-N antibody measurements were carried out under static conditions. In this set up, the NCM was removed from the capillary-flow device upon completion of the fluidic assay and before addition of 1 μL of the TMB substrate. Chronoamperometry measurements started 2 min after the addition of TMB to the NCM. Three SPCEs were successively connected to several NCMs exposed to different anti-N antibody concentrations. Figure 3A displays

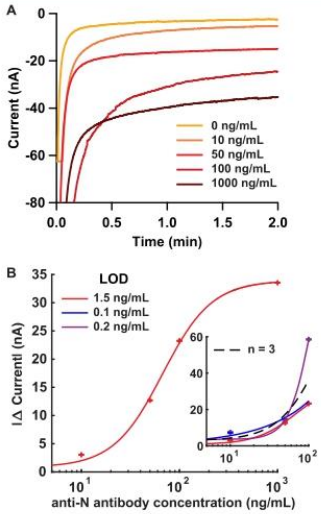

Figure 3. Static electrochemical detection of anti-N antibodies in PBS samples. (A) Chronoamperograms obtained from one SPCE consecutively connected to the NCM taken from five capillary-flow devices, each exposed to a 5 μL PBS-based sample of distinct anti-N antibody concentration. (B) Corresponding calibration curve showing blank-subtracted current at t = 100 s (red). (Insert), amplification of B showing the measurements recorded with three independent SPCEs (red, blue, and purple) and overall signal fit (black dashed line). Markers and error bars represent average and standard deviation (sd) over a 10 s interval centered in 100 s. Data fitted with a 4-parameter logistic (4PL) regression. Limits of detection (LODs) are calculated as the anti-N concentration corresponding to 3 sd of the blank signal.

the chronoamperograms recorded from a single SPCE exposed to five anti-N antibody concentrations ranging from 0 to 1 μg/mL and the calibration curve generated by this dataset is shown in Figure 3B, together with calibration curves of the other two SPCEs (insert).

The current-to-concentration response of each SPCE followed a 4PL model, which is typical for immunoassays.[44] Inherent variability of electrodes that are stencil printed by hand resulted in different LOD across the 3 SPCEs. Nevertheless, all three LODs were below 2 ng/mL, demonstrating the ability of this assay to consistently detect anti-N antibody concentrations in 5 μL PBS samples down to the low ng/mL range, which outperforms commercially available[45,46] as well as recently-developed POC anti-N antibody assays.[47−49] These results prove that the capillary-flow device successfully delivers sample and detection antibody to the NCM and performs effective washing steps. It also demonstrates successful electrochemical detection of TMB as the immunoassay substrate, using a SPCE placed directly on the NCM.

In-Flow Electrochemical Detection of Anti-N Antibodies. Following preliminary results in the static measure-

https://doi.org/10.1021/acssensors.1c01527
ACS Sens. 2021, 6, 4067−4075

ment setup, flow-based anti-N antibody tests were performed on PBS-based samples by running chronoamperometry under flow conditions. Chronoamperometry measurements were started upon delivery of buffer to the detection zone and ended upon flow completion. Three SPCEs were successively connected to four capillary-flow devices that were supplied with PBS-based samples of four different anti-N antibody concentrations ranging from 0 to 100 ng/mL.

Under flow conditions, delivery of TMB to the detection zone produced a transient increase in the cathodic current (Figure 4A) that correlated to the concentration of anti-N

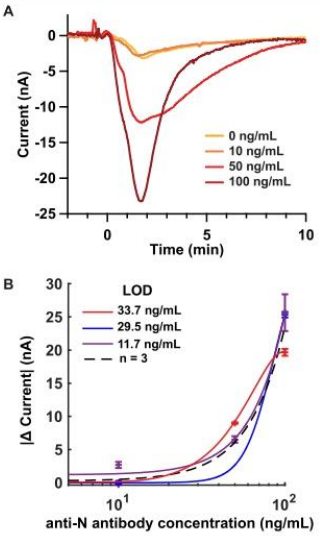

Figure 4. In-flow electrochemical detection of anti-N antibodies in PBS samples. (A) Excerpt of chronoamperograms recorded from one SPCE consecutively connected to four different capillary flow-devices, each supplied with a 5 μL PBS-based sample of distinct anti-N antibody concentration. Data were time-aligned with TMB delivery to the detection zone (t = 0). (B) Calibration curves obtained for three independent SPCEs (red from data shown in A, blue and purple) and overall fit for all three SPCEs (black dashed line). Markers and error bars represent average and sd over a 30 s interval centered in the current local minimum. For each SPCE, the blank signal is subtracted from the data. Data fitted with a 4PL regression. LODs are calculated as the anti-N concentration corresponding to 3 sd of the blank signal.

antibody in the sample (Figure 4B). As in the static measurement setup, the current-to-concentration response of each SPCE followed a 4PL model and variability between electrodes stencil printed by hand was observed. LODs obtained were slightly higher than those achieved in the static setup, which can be due to dispersive blurring of TMB in the microfluidic flow. However, in-flow detection of anti-N antibodies in the low ng/mL range was still possible.

Detection of Anti-N Antibodies in Whole Human Blood. Finally, whole human blood was spiked with different anti-N antibody concentrations ranging from 0 to 100 ng/mL. These samples were run on the complete fluidic device integrating the blood-filtration membrane, as shown in Figure 1, and chronoamperometry measurements were carried out under flow conditions, as described previously. Three SPCEs were successively connected to four capillary-flow devices running these whole blood samples spiked with anti-N antibodies. In-flow chronoamperograms from one SPCE (Figure 5A) show the increase in the cathodic current

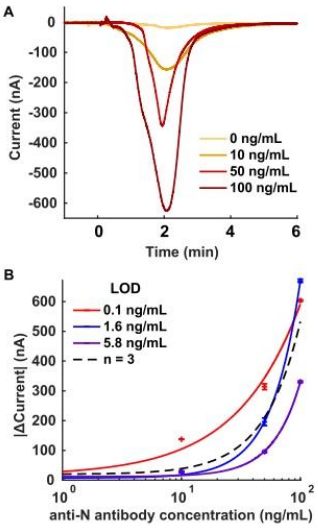

Figure 5. In-flow detection of anti-N antibodies in human whole blood samples. (A) Representative chronoamperograms recorded from one SPCE consecutively connected to four different capillary flow-devices supplied with 10 μL human whole blood samples spiked with different anti-N antibody concentrations. Data were time-aligned with TMB delivery to the detection zone (t = 0). (B) Calibration curves recorded with three independent SPCEs (red from data shown in A, blue and purple) and overall fit for all three SPCEs (black dashed line). Markers and error bars represent average and sd over a 30 s interval centered in the current local minimum. For each SPCE, the blank signal is subtracted from the data. Data fitted with a 4PL regression. LODs are calculated as the anti-N concentration corresponding to 3 sd of the blank signal.

recorded upon delivery of TMB to the detection zone. The correlation between the magnitude of this current and the concentration of anti-N antibody in the whole blood samples is shown in Figure 5B for all three SPCEs.

As for PBS-based samples, the current-to-concentration response of each SPCE followed a 4PL model and variability between electrodes was observed. This is shown by the difference in the magnitude of current response observed between the three SPCEs and highlights the variability of our current electrochemical device. The magnitude of the currents recorded here was 20 times higher than for PBS-based samples. This signal increase was attributed to three main causes: (i) blood sample volume was 10 μL instead of 5 μL for the PBS-based samples, to cover the entire surface of the blood-filtration membrane and to maximize analyte extraction; (ii) delivery of blood sample to the NCM was slowed down by the blood-filtration membrane, allowing for longer sample incubation time on the detection zone, hence enhancing analyte capture; and (iii) the higher viscosity of plasma compared to PBS could further decrease the sample flowrate through the NCM. The increased signal magnitude for whole

https://doi.org/10.1021/acssensors.1c01527
ACS Sens. 2021, 6, 4067−4075

blood samples lead to improved analytical performance, with higher sensitivity and lower LODs down to the 5 ng/mL range (Figure 5), which matches that of commercially available tests.[45,46] Table S2 provides a side-by-side comparison of the performance of our electrochemical capillary-flow device in relation to other tests for SARS-CoV-2 anti N antibodies reported in the literature or commercially available. Note that our device is the only one providing a quantitative detection in whole blood samples at the point of care.

Proof-of-Concept Detection on a Smartphone. As a proof-of-concept experiment, the electrochemical capillary-flow device was coupled to an NFC potentiostat operated by a smartphone and this truly portable system was used to detect anti-N antibodies in whole blood samples. Commonly available in smartphones, NFC is a low-cost technology that enables wireless communication using a simple setup, making it ideal for use in POC applications. The NFC potentiostat (SIC4341, ISO14443A, Silicon Craft Technology PLC) was operated by an Android smartphone (Motorola One, XT1941) running a mobile application made available by Silicon Craft (SIC4341 Allstar Android app). The electrochemical capillary-flow device was connected to the NFC potentiostat via a socket mounted on the NFC potentiostat printed circuit board, in which the SPCE was inserted, as shown in Figure 6A.

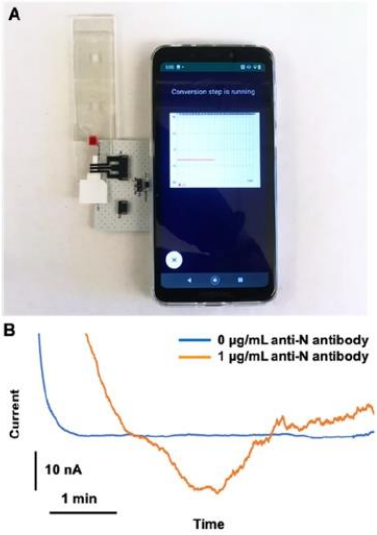

Figure 6. (A) Picture of the whole smartphone-based detection system, showing the electrochemical capillary-flow device connected to the NFC potentiostat, which is wirelessly operated from a smartphone. (B) In-flow chronoamperograms wirelessly recorded using the NFC potentiostat operated by a smartphone. Data are from two different capillary flow-devices supplied with 5 μL PBS-based samples of 0 and 1 μg/mL anti-N antibody concentrations.

The connection between the NFC potentiostat and the smartphone was established by simply placing the smartphone over the NFC potentiostat, and this wireless connection automatically powered it. First, basic electrochemistry was performed to demonstrate the well-functioning of the NFC potentiostat. A cyclic voltammogram recorded from a SPCE in ferri/ferrocyanide is shown in Figure S2, and the complete measurement set up and recording is shown in Video S2. Then, to demonstrate the capability of this system to detect anti-N antibody, two electrochemical capillary-flow devices supplied with PBS-based samples of 0 (blank sample) and 1 μg/mL anti-N antibody were run and chronoamperometry was performed using the NFC potentiostat. The current responses from these two measurements are displayed in Figure 6B. A clear increase in the cathodic current recorded from the 1 μg/mL anti-N antibody sample was observed while the current from the blank sample remained constant throughout the 5 min measurement. While the concentration of anti-N antibody tested here was higher than the targeted clinical range, this proof-of-concept experiment demonstrates the capacity of the NFC potentiostat to be used for this assay. Further optimization of the NFC potentiostat current range is needed to allow the detection of current responses generated by samples of low anti-N antibody concentrations. This fully portable wireless smartphone-based system would greatly facilitate detection at the point of care.

■ CONCLUSIONS

We have presented the development of a new electrochemical capillary flow device and demonstrated its ability to detect IgG antibodies against SARS-CoV-2 N proteins with performance matching commercially available tests.[45,46] The device is easy to use, can be fabricated at low cost (<$0.5, see Table S1), and is single-use/disposable, making it ideal for POC applications. Thanks to an integrated blood-filtration membrane, a droplet of whole blood is added directly to the device and cells are continuously filtered, while plasma is delivered to a microfluidic circuit, which then performs the multistep assay. This eliminates the need for sample preparation, provides sequential delivery of multiple reagents to the detection zone, reduces the number of pipetting steps, and minimizes user intervention, enhancing the potential of such devices for use in a POC setting. Like in a sandwich LFIA assay, the target analyte anti-N antibody is captured on a NCM modified with N protein and detected using labelled secondary antibodies. However, the device developed here uses electrochemical detection via a SPCE that is placed on the NCM and connected to a portable potentiostat. While maintaining the ease of use and the rapidity of a LFIA, this novel system provides a highly sensitive detection, with detection limits lower than 10 ng/mL anti-N antibody in human whole blood samples as small as 10 μL. Critically, the electrochemical detection provides a quantitative output, eliminating any possible user interpretation error, which is a major advantage of the system to be used at the point of care. In a proof-of-concept experiment, the device was successfully used with a low-cost NFC potentiostat operated from a smartphone. This potentiostat could be integrated with the device in the future, so that the whole system is disposable. This would eliminate the need for any dedicated instrumentation as the test could be run from a smartphone only, making it useable at the point of need. Future work shall focus on tuning the NFC potentiostat to match its recording range to output signals from samples of clinically low analyte concentration. Whilst there is preliminary evidence showing stability over storage of every active component of the device (the electrode,[41] the N protein modified NCM[37] and the detection antibody reagent pad[40]), a stability study of the complete device was not conducted yet and would be necessary for the device to access the POC market. Lastly, further developments

https://doi.org/10.1021/acssensors.1c01527
ACS Sens. 2021, 6, 4067−4075

are needed to increase the reproducibility of our measurements. We believe that variability between electrodes, which are currently stencil-printed by hand, could be eliminated by screen-printing electrodes in batches, as it is performed in manufacturing settings. Additionally, manufacturing capillary-flow devices in batches would allow for uniform assembly of the device layers and provide a consistent pressure between the electrodes and the NCM. This is difficult to accomplish by hand assembly but is necessary to enhance the reproducibility of our quantitative detection to translate it to real-world POC use. Applied to the detection of other pathogens, this novel electrochemical capillary-flow technology has the potential to aid the diagnosis of multiple infectious diseases at the point of care.

■ ASSOCIATED CONTENT

Supporting Information

The Supporting Information is available free of charge at https://pubs.acs.org/doi/10.1021/acssensors.1c01527.

Schematics of capillary-flow device without blood-filtration membrane, cyclic voltammogram recorded with NFC potentiostat, and cost of capillary-flow device (PDF)

32x-accelerated video of capillary-flow device operation (MP4)

Video of NFC potentiostat operation (MP4)

■ AUTHOR INFORMATION

Corresponding Author

Charles S. Henry − *Department of Chemistry, Department of Chemical and Biological Engineering, and School of Biomedical Engineering, Colorado State University, Fort Collins, Colorado 80523, United States;* orcid.org/0000-0002-8671-7728; Email: chuck.henry@colostate.edu

Authors

Isabelle C. Samper − *Department of Chemistry and Department of Chemical and Biological Engineering, Colorado State University, Fort Collins, Colorado 80523, United States*

Ana Sánchez-Cano − *Department of Chemistry, Colorado State University, Fort Collins, Colorado 80523, United States; Diagnostic Nanotools Group, Institut de Recerca, Barcelona 08035, Spain; Universitat Autónoma de Barcelona, Barcelona 08193, Spain*

Wisarut Khamcharoen − *Department of Chemistry, Colorado State University, Fort Collins, Colorado 80523, United States; Department of Chemistry, Faculty of Science, Srinakharinwirot University, Bangkok 10110, Thailand*

Ilhoon Jang − *Department of Chemistry, Colorado State University, Fort Collins, Colorado 80523, United States; Institute of Nano Science and Technology, Hanyang University, Seoul 04763, South Korea*

Weena Siangproh − *Department of Chemistry, Faculty of Science, Srinakharinwirot University, Bangkok 10110, Thailand*

Eva Baldrich − *Diagnostic Nanotools Group, Institut de Recerca, Barcelona 08035, Spain;* orcid.org/0000-0003-1393-215X

Brian J. Geiss − *Department of Microbiology, Immunology, and Pathology and School of Biomedical Engineering, Colorado State University, Fort Collins, Colorado 80523, United States*

David S. Dandy − *Department of Chemical and Biological Engineering and School of Biomedical Engineering, Colorado State University, Fort Collins, Colorado 80523, United States;* orcid.org/0000-0003-3254-0717

Complete contact information is available at: https://pubs.acs.org/10.1021/acssensors.1c01527

Author Contributions

♦I.C.S., A.S.-C. and W.K. contributed equally.

Notes

The authors declare no competing financial interest.

■ ACKNOWLEDGMENTS

We would like to thank James Terry and Loran Anderson for providing recombinant SARS-CoV-2 N protein. This work has been supported by the NIH (R01 AI132668), the Insituto de Salud Carlos III and the European regional Development Fund (IFI18/00020, MV19/00036, CPII18/00025), the Science Achievement Scholarship of Thailand (SAST), the Colorado Office of Economic Development and International Trade (OEDIT), and Balanced Biotech Inc.

■ REFERENCES

(1) WHO. WHO Coronavirus (COVID-19) Dashboard|WHO Coronavirus Disease (COVID-19) Dashboard. https://covid19.who.int/ (accessed Jul 10, 2021).

(2) IHE. Testing, Screening, and Outbreak Response for Institutions of Higher Education (IHEs)|CDC. https://www.cdc.gov/coronavirus/2019-ncov/community/colleges-universities/ihe-testing.html (accessed Mar 12, 2021).

(3) Pollán, M.; Pérez-Gómez, B.; Pastor-Barriuso, R.; Oteo, J.; Hernán, M. A.; Pérez-Olmeda, M.; Sanmartín, J. L.; Fernández-García, A.; Cruz, I.; de Larrea, N. F.; et al. Prevalence of SARS-CoV-2 in Spain (ENE-COVID): A Nationwide, Population-Based Seroepidemiological Study. *Lancet* **2020**, *396*, 535−544.

(4) Nuccetelli, M.; Pieri, M.; Grelli, S.; Ciotti, M.; Miano, R.; Andreoni, M.; Bernardini, S. SARS-CoV-2 Infection Serology: A Useful Tool to Overcome Lockdown? *Cell Death Discovery* **2020**, *6*, 1−9.

(5) Böger, B.; Fachi, M. M.; Vilhena, R. O.; Cobre, A. F.; Tonin, F. S.; Pontarolo, R. Systematic Review with Meta-Analysis of the Accuracy of Diagnostic Tests for COVID-19. *Am. J. Infect. Control* **2021**, *49*, 21−29.

(6) Kevadiya, B. D.; Machhi, J.; Herskovitz, J.; Oleynikov, M. D.; Blomberg, W. R.; Bajwa, N.; Soni, D.; Das, S.; Hasan, M.; Patel, M.; et al. Diagnostics for SARS-CoV-2 Infections. *Nat. Mater.* **2021**, *20*, 593−605.

(7) Salazar, E.; Kuchipudi, S. V.; Christensen, P. A.; Eagar, T.; Yi, X.; Zhao, P.; Jin, Z.; Long, S. W.; Olsen, R. J.; Chen, J.; et al. Convalescent Plasma Anti−SARS-CoV-2 Spike Protein Ectodomain and Receptor-Binding Domain IgG Correlate with Virus Neutralization. *J. Clin. Invest.* **2020**, *130*, 6728−6738.

(8) Kopel, J.; Goyal, H.; Perisetti, A. Antibody Tests for COVID-19. *Proc.—Bayl. Univ. Med. Cent.* **2021**, *34*, 63−72.

(9) Emanuel, E. J.; Persad, G.; Upshur, R.; Thome, B.; Parker, M.; Glickman, A.; Zhang, C.; Boyle, C.; Smith, M.; Phillips, J. P. Fair Allocation of Scarce Medical Resources in the Time of Covid-19. *N. Engl. J. Med.* **2020**, *382*, 2049−2055.

(10) Sheridan, C. Fast, Portable Tests Come Online to Curb Coronavirus Pandemic. *Nat. Biotechnol.* **2020**, *38*, 515−518.

(11) Patel, E. U.; Bloch, E. M.; Clarke, W.; Hsieh, Y. H.; Boon, D.; Eby, Y.; Fernandez, R. E.; Baker, O. R.; Keruly, M.; Kirby, C. S.; et al. Comparative Performance of Five Commercially Available Serologic

https://doi.org/10.1021/acssensors.1c01527
ACS Sens. 2021, 6, 4067−4075

Assays to Detect Antibodies to SARS-CoV-2 and Identify Individuals with High Neutralizing Titers. *J. Clin. Microbiol.* **2021**, *59*, 1−10.
(12) Charlton, C. L.; Kanji, J. N.; Johal, K.; Bailey, A.; Plitt, S. S.; MacDonald, C.; Kunst, A.; Buss, E.; Burnes, L. E.; Fonseca, K.; et al. Evaluation of Six Commercial Mid- To High-Volume Antibody and Six Point-of-Care Lateral Flow Assays for Detection of SARS-CoV-2 Antibodies. *J. Clin. Microbiol.* **2020**, *58*, 1−12.
(13) Andryukov, B. G. Six Decades of Lateral Flow Immunoassay: From Determining Metabolic Markers to Diagnosing Covid-19. *AIMS Microbiol.* **2020**, *6*, 280−304.
(14) Liu, Y.; Zhan, L.; Qin, Z.; Sackrison, J.; Bischof, J. C. Ultrasensitive and Highly Specific Lateral Flow Assays for Point-of-Care Diagnosis. *ACS Nano* **2021**, *15*, 3593−3611.
(15) Cesewski, E.; Johnson, B. N. Electrochemical Biosensors for Pathogen Detection. *Biosens. Bioelectron.* **2020**, *159*, 112214.
(16) Monzó, J.; Insua, I.; Fernandez-Trillo, F.; Rodriguez, P. Fundamentals, Achievements and Challenges in the Electrochemical Sensing of Pathogens. *Analyst* **2015**, *140*, 7116−7128.
(17) Xu, X.; Zhang, S.; Chen, H.; Kong, J. Integration of Electrochemistry in Micro-Total Analysis Systems for Biochemical Assays: Recent Developments. *Talanta* **2009**, *80*, 8−18.
(18) de Eguilaz, M. R.; Cumba, L. R.; Forster, R. J. Electrochemical Detection of Viruses and Antibodies: A Mini Review. *Electrochem. Commun.* **2020**, *116*, 106762.
(19) Li, X.-M.; Yang, X.-Y.; Zhang, S.-S. Electrochemical Enzyme Immunoassay Using Model Labels. *Trac. Trends Anal. Chem.* **2008**, *27*, 543−553.
(20) Layqah, L. A.; Eissa, S. An Electrochemical Immunosensor for the Corona Virus Associated with the Middle East Respiratory Syndrome Using an Array of Gold Nanoparticle-Modified Carbon Electrodes. *Microchim. Acta* **2019**, *186*, 1−10.
(21) Ozer, T.; Geiss, B. J.; Henry, C. S. Chemical and Biological Sensors for Viral Detection. *J. Electrochem. Soc.* **2020**, *167*, 037523.
(22) Zhao, C.; Liu, X. A Portable Paper-Based Microfluidic Platform for Multiplexed Electrochemical Detection of Human Immunodeficiency Virus and Hepatitis C Virus Antibodies in Serum. *Biomicrofluidics* **2016**, *10*, 024119.
(23) Wang, L.; Filer, J. E.; Lorenz, M. M.; Henry, C. S.; Dandy, D. S.; Geiss, B. J. An Ultra-Sensitive Capacitive Microwire Sensor for Pathogen-Specific Serum Antibody Responses. *Biosens. Bioelectron.* **2019**, *131*, 46−52.
(24) da Silva, E. T. S. G.; Souto, D. E. P.; Barragan, J. T. C.; de Giarola, J. F.; de Moraes, A. C. M.; Kubota, L. T. Electrochemical Biosensors in Point-of-Care Devices: Recent Advances and Future Trends. *ChemElectroChem* **2017**, *4*, 778−794.
(25) Ruiz-Vega, G.; Arias-Alpízar, K.; de la Serna, E.; Borgheti-Cardoso, L. N.; Sulleiro, E.; Molina, I.; Fernàndez-Busquets, X.; Sánchez-Montalvá, A.; del Campo, F. J.; Baldrich, E. Electrochemical POC Device for Fast Malaria Quantitative Diagnosis in Whole Blood by Using Magnetic Beads, Poly-HRP and Microfluidic Paper Electrodes. *Biosens. Bioelectron.* **2020**, *150*, 111925.
(26) Sun, A. C.; Hall, D. A. Point-of-Care Smartphone-Based Electrochemical Biosensing. *Electroanalysis* **2019**, *31*, 2−16.
(27) Wan, Y.; Su, Y.; Zhu, X.; Liu, G.; Fan, C. Development of Electrochemical Immunosensors towards Point of Care Diagnostics. *Biosens. Bioelectron.* **2013**, *47*, 1−11.
(28) Samper, I. C.; Gowers, S. A. N.; Booth, M. A.; Wang, C.; Watts, T.; Phairatana, T.; Vallant, N.; Sandhu, B.; Papalois, V.; Boutelle, M. G. Portable Microfluidic Biosensing System for Real-Time Analysis of Microdialysate in Transplant Kidneys. *Anal. Chem.* **2019**, *91*, 14631−14638.
(29) Mettakoonpitak, J.; Boehle, K.; Nantaphol, S.; Teengam, P.; Adkins, J. A.; Srisa-Art, M.; Henry, C. S. Electrochemistry on Paper-Based Analytical Devices: A Review. *Electroanalysis* **2016**, *28*, 1420−1436.
(30) Noviana, E.; McCord, C. P.; Clark, K. M.; Jang, I.; Henry, C. S. Electrochemical Paper-Based Devices: Sensing Approaches and Progress toward Practical Applications. *Lab Chip* **2020**, *20*, 9−34.
(31) Ataide, V. N.; Mendes, L. F.; Gama, L. I. L. M.; de Araujo, W. R.; Paixão, T. R. L. C. Electrochemical Paper-Based Analytical Devices: Ten Years of Development. *Anal. Methods* **2020**, *12*, 1030−1054.
(32) Jang, I.; Carrão, D. B.; Menger, R. F.; Moraes De Oliveira, A. R.; Henry, C. S. Pump-Free Microfluidic Rapid Mixer Combined with a Paper-Based Channel. *ACS Sens.* **2020**, *5*, 2230−2238.
(33) Jang, I.; Kang, H.; Song, S.; Dandy, D. S.; Geiss, B. J.; Henry, C. S. Flow Control in a Laminate Capillary-Driven Microfluidic Device. *Analyst* **2021**, *146*, 1932−1939.
(34) Burbelo, P. D.; Riedo, F. X.; Morishima, C.; Rawlings, S.; Smith, D.; Das, S.; Strich, J. R.; Chertow, D. S.; Davey, R. T.; Cohen, J. I. Sensitivity in Detection of Antibodies to Nucleocapsid and Spike Proteins of Severe Acute Respiratory Syndrome Coronavirus 2 in Patients With Coronavirus Disease 2019. *J. Infect. Dis.* **2020**, *222*, 206−213.
(35) Azkur, A. K.; Akdis, M.; Azkur, D.; Sokolowska, M.; Veen, W.; Brüggen, M. C.; O'Mahony, L.; Gao, Y.; Nadeau, K.; Akdis, C. A. Immune Response to SARS-CoV-2 and Mechanisms of Immunopathological Changes in COVID-19. *Allergy* **2020**, *75*, 1564−1581.
(36) Batra, M.; Tian, R.; Zhang, C.; Clarence, E.; Sacher, C. S.; Miranda, J. N.; De La Fuente, J. R. O.; Mathew, M.; Green, D.; Patel, S.; et al. Role of IgG against N-Protein of SARS-CoV2 in COVID19 Clinical Outcomes. *Sci. Rep.* **2021**, *11*, 3455.
(37) Carrell, C.; Link, J.; Jang, I.; Terry, J.; Scherman, M.; Call, Z.; Panraksa, Y.; Dandy, D. S.; Geiss, B. J.; Henry, C. Point-of-Need Disposable ELISA System for COVID-19 Serology Testing. *ChemRxiv* **2020**, DOI: 10.26434/chemrxiv.13050539.v2.
(38) Fagre, A.; Lewis, J.; Eckley, M.; Zhan, S.; Rocha, S. M.; Sexton, N. R.; Burke, B.; Geiss, B.; Peersen, O.; Bass, T.; et al. SARS-CoV-2 Infection, Neuropathogenesis and Transmission among Deer Mice: Implications for Spillback to New World Rodents. *PLoS Pathog.* **2021**, *17*, No. e1009585.
(39) Terry, J. S.; Anderson, L. B.; Scherman, M. S.; McAlister, C. E.; Perera, R.; Schountz, T.; Geiss, B. J. Development of a SARS-CoV-2 Nucleocapsid Specific Monoclonal Antibody. *Virology* **2021**, *558*, 28−37.
(40) Ramachandran, S.; Fu, E.; Lutz, B.; Yager, P. Long-Term Dry Storage of an Enzyme-Based Reagent System for ELISA in Point-of-Care Devices. *Analyst* **2014**, *139*, 1456−1462.
(41) Kava, A. A.; Henry, C. S. Exploring Carbon Particle Type and Plasma Treatment to Improve Electrochemical Properties of Stencil-Printed Carbon Electrodes. *Talanta* **2021**, *221*, 121553.
(42) Liu, C.; Liao, S.-C.; Song, J.; Mauk, M. G.; Li, X.; Wu, G.; Ge, D.; Greenberg, R. M.; Yang, S.; Bau, H. H. A High-Efficiency Superhydrophobic Plasma Separator. *Lab Chip* **2016**, *16*, 553−560.
(43) Su, X.; Zhang, J.; Zhang, D.; Wang, Y.; Chen, M.; Weng, Z.; Wang, J.; Zeng, J.; Zhang, Y.; Zhang, S.; et al. High-Efficiency Plasma Separator Based on Immunocapture and Filtration. *Micromachines* **2020**, *11*, 352.
(44) O'Connell, M. A.; Belanger, B. A.; Haaland, P. D. Calibration and Assay Development Using the Four-Parameter Logistic Model. *Chemom. Intell. Lab. Syst.* **1993**, *20*, 97−114.
(45) GmbH. ABIN6952772 SARS-CoV-2 N-Protein IgG Antibody (SARS-CoV-2 N IgG) ELISA Kit. https://www.antibodies-online.com/productsheets/ABIN6952772.pdf (accessed May 11, 2021).
(46) Protein Tech. Anti-SARS-CoV-2 N protein Human IgG ELISA Kit Elisa Kit KE30001 Proteintech. https://www.ptglab.com/Products/Pictures/pdf/Virus-IgG-for-2019-nCoV-N-protein-ELISA-Kit-KE30001-datasheet.pdf (accessed Mar 18, 2021).
(47) Kim, S.; Hao, Y.; Miller, E. A.; Tay, D. M. Y.; Yee, E.; Kongsuphol, P.; Jia, H.; McBee, M.; Preiser, P. R.; Sikes, H. D. Vertical Flow Cellulose-Based Assays for SARS-CoV-2 Antibody Detection in Human Serum. *ACS Sens.* **2021**, *6*, 1891−1898.
(48) Kasetsirikul, S.; Umer, M.; Soda, N.; Sreejith, K. R.; Shiddiky, M. J. A.; Nguyen, N.-T. Detection of the SARS-CoV-2 Humanized Antibody with Paper-Based ELISA. *Analyst* **2020**, *145*, 7680−7686.
(49) Wang, Z.; Zheng, Z.; Hu, H.; Zhou, Q.; Liu, W.; Li, X.; Liu, Z.; Wang, Y.; Ma, Y. A Point-of-Care Selenium Nanoparticle-Based Test

https://doi.org/10.1021/acssensors.1c01527
ACS Sens. 2021, 6, 4067−4075

for the Combined Detection of Anti-SARS-CoV-2 IgM and IgG in Human Serum and Blood. *Lab Chip* **2020**, *20*, 4255−4261.

https://doi.org/10.1021/acssensors.1c01527
ACS Sens. 2021, 6, 4067−4075

VITA

NAME	WISARUT KHAMCHAROEN
DATE OF BIRTH	5 DEC 1993
PLACE OF BIRTH	BANGKOK
INSTITUTIONS ATTENDED	2554 High scool from Santichon Islamic School 2558 Bechelor Degree in Science, majoring in Chemistry with 2nd honor from Srinakharinwirot University
HOME ADDRESS	25/1, Moo 3, Tambon Phra Achan, Ongkhalak, Nakhon Nayok, 26120
PUBLICATION	1. Khamcharoen, W., & Siangproh, W. (2021). A multilayer microfluidic paper coupled with an electrochemical platform developed for sample separation and detection of dopamine. New Journal of Chemistry, 45(29), 12886-12894. 2. Khamcharoen, W., Henry, C. S., & Siangproh, W. (2022). A novel l-cysteine sensor using in-situ electropolymerization of l-cysteine: Potential to simple and selective detection. Talanta, 237, 122983. 3. Samper, I. C., Sánchez-Cano, A., Khamcharoen, W., Jang, I., Siangproh, W., Baldrich, E., Henry, C. S. (2021). Electrochemical Capillary-Flow Immunoassay for Detecting Anti-SARS-CoV-2 Nucleocapsid Protein Antibodies at the Point of Care. ACS Sensors.